

POLITECNICO DI MILANO

School of Industrial and Information Engineering

Master Degree in Engineering Physics



**ASSESSMENT OF NUMERICAL METHODS FOR PARTICLE TRACKING
IN FIELD MAPS**

Supervisor:

Prof. Luca BONAVENTURA

External Supervisor:

Dr. Andrea LATINA

Candidate:

Costanza AGAZZI 876500

ACADEMIC YEAR 2018 - 2019

Costanza Agazzi,
Assessment of Numerical Methods for Particle Tracking in Field Maps |
Master Thesis in Engineering Physics,
Politecnico di Milano.

Politecnico di Milano:
www.polimi.it

School of Industrial and Information Engineering:
www.ingindinf.polimi.it

Contents

Introduction	1
1 Magnetic Field and Coils System	5
1.1 The Maxwell's Equations	5
1.2 Transfer Matrix for a Solenoid	7
1.3 Coils System	12
1.4 Coils Equations	14
2 Hamiltonian Systems	21
2.1 Canonical Transformations	23
2.2 Extended Phase Space	24
2.3 Choice of the Independent Variable	25
2.4 Symplectic Condition	27
2.5 Symplecticity and Liouville's Theorem	29
2.6 Hamiltonian for a Charged Particle	30
2.7 Alternative Form of the Equations of Motion	35
2.8 The Helmholtz Theorem	35
3 Numerical Methods	39
3.1 Vector Potential Post-Processing Methods	39
3.2 Quadrature Formulae	45
3.3 Interpolation Methods	46
3.4 ODE Integrators	54
3.5 Error Evaluation	59
4 Numerical Experiments	61
4.1 Modeling the System of Coils	61
4.2 Definition of the Discrete Mesh	63
4.3 Comparison of Different Integration Methods	67
4.4 Particle Tracking Results	73
4.5 First Test: Trajectory Study	73
4.6 Second Test: Emittance	76
4.7 Third Test: Measurement Errors Correction	80
5 Conclusions and Perspectives	85
A Measure Units	87

A.1 Units	87
A.2 Physical Constants	88
B Liouville's Theorem Demonstration	89
Bibliography	93

List of Figures

1	CERN accelerators complex.	1
2	Standard tracking procedure.	2
3	New tracking procedure.	4
1.1	Circulation structure in the solenoid.	7
1.2	Subdivision of the solenoid magnetic field along the z axis.	8
1.3	Transverse section of the solenoid.	9
1.4	Magnetic field generated by two coils leading the same currents.	12
1.5	System of coils leading opposite currents.	13
1.6	Magnetic field generated by two coils leading opposite currents.	13
1.7	Coil reference system	14
2.1	Path of the integral in phase space	26
3.1	Interpolation comparison.	50
3.2	First derivative of the interpolated function.	50
3.3	Second derivative of the interpolated function.	51
3.4	Axis of time.	54
4.1	Scheme of the system of coils.	61
4.2	Magnetic field variation with number of coils: one coil versus three coils	62
4.3	Magnetic field variation with number of coils:16 coils versus 32.	62
4.4	Periodic construction of the magnetic field. In red, the elementary unit formed by two coils, then repeated along the z axis four times.	62
4.5	Grid for interpolation.	63
4.6	Interpolation error changing the grid size	64
4.7	Overall interpolated field.	65
4.8	Absolute error for the FIRST post-processing method.	66
4.9	Absolute error for the SECOND post-processing method.	66
4.10	Analytic field: Relative L^2 -norm error for x	67
4.11	Analytic field: Relative L^2 -norm error for p_y	68
4.12	Gauss6, different interpolations: relative L^2 -norm error for x	68
4.13	Gauss6, different interpolations: relative L^2 -norm error for p_y	69
4.14	Mid-point, different interpolations: relative L^2 -norm error for x	70
4.15	Mid-point, different interpolations: relative L^2 -norm error for p_y	70
4.16	Runge Kutta 4, different interpolations: relative L^2 -norm error for x and p_y	71

4.17	Gauss 4, different interpolations: relative L^2 -norm error for x and p_y .	71
4.18	CPU time for the analytic field: relative L^2 -norm error for x .	72
4.19	CPU time for the analytic field: relative L^2 -norm error for p_y .	72
4.20	First test: arrangement of the particles (example in the 3D space).	74
4.21	Trajectory on the xy plane for the analytic field directly interpolated with the LINT method.	74
4.22	Trajectory on the xy plane for the analytic field reconstructed with the FIRST method.	75
4.23	Trajectory on the xy plane for the analytic field reconstructed with the SECOND method.	75
4.24	Particle distribution in a realistic case (in trace space (x, x')).	76
4.25	Emittance behavior for the three different methods vs. the number of turns.	79
4.26	Emittance behavior for the divergence free preserving methods.	80
4.27	\mathbf{B}_z field considered in the third test.	81
4.28	Transverse emittance over the number of integration steps.	82
4.29	FIRST and SECOND methods: transverse emittance over the number of integration steps.	83
4.30	$ \det(\mathbf{M}) $ over the number of integration steps for all the methods.	84
4.31	Zoom on FIRST and SECOND methods: $ \det(\mathbf{M}) $ over the number of integration steps.	84

Sommario

Il tracciamento di particelle attraverso gli elementi di un acceleratore necessita di metodi numerici che siano accurati ed efficienti. L'obiettivo di questa tesi è studiare e testare metodi che garantiscano la conservazione delle proprietà del moto delle particelle, anche nel caso di passaggio attraverso elementi non lineari.

In questo lavoro sono stati implementati due metodi di ricostruzione e post-processamento del potenziale vettore in casi realistici, con lo scopo di conservare le proprietà di divergenza nulla del campo magnetico. Questi sono stati poi confrontati con i più classici metodi di interpolazione.

Diverse tecniche di integrazione numerica, utilizzate per il calcolo delle equazioni del moto, sono state poi messe a confronto. Infine, sono stati studiati gli effetti di diversi metodi di interpolazione sull'efficacia del processo di integrazione.

Parte di questo lavoro è stata sviluppata durante uno stage di quattordici mesi presso il CERN (*European Organization for Nuclear Research*) di Ginevra, sotto la supervisione del Dr. Andrea Latina. Al termine di questa esperienza, il lavoro è stato completato presso il Politecnico di Milano.

Parole chiave: Tracciamento di particelle, Metodi numerici, Post-processamento, Integratori numerici, Ricostruzione a divergenza nulla.

Abstract

Particle tracking in accelerators elements requires accurate and efficient numerical methods. The aim of this thesis is to study and test methods which guarantee the conservation of particle motion properties when crossing non-linear elements. Two techniques for the reconstruction and post-processing of realistic vector potentials, aiming to preserve the divergence free property of the magnetic field, have been implemented and compared with more classical interpolation methods. Various integration techniques for the determination of particle motion have been compared. Moreover, the impact of different interpolation methods on the numerical integration process was observed.

The idea for this thesis work started during an internship at CERN (*European Organization for Nuclear Research*, Geneva, Switzerland), from September 2017 to November 2018. There, my work was coordinated by Dr. Andrea Latina, in the “Beam Department” (BE), “Accelerators and Beam Physics” (ABP) group. At the end of the time spent at CERN, this work was continued and completed at Politecnico di Milano. This thesis presents the results achieved independently in both the experiences, analysing the process of particle tracking from two complementary view points.

Keywords: Particle tracking, Numerical methods, Post-processing, Numerical integrators, Divergence-free reconstruction.

Introduction

CERN is the most important research centre in the world for particle physics. CERN's mission is to provide a unique range of particle accelerator facilities to uncover what the universe is made of and how it works. Particle accelerators are used to obtain extremely high-energy particle beams that collide in dedicated detection areas, called experiments. The products of such collisions are detected, recorded and analysed, the final goals being on one hand to confirm theoretical predictions and, on the other hand, to search for new theoretical explanations of previously unseen phenomena, to understand the most fundamental laws of nature and ultimately advance the boundaries of human knowledge.

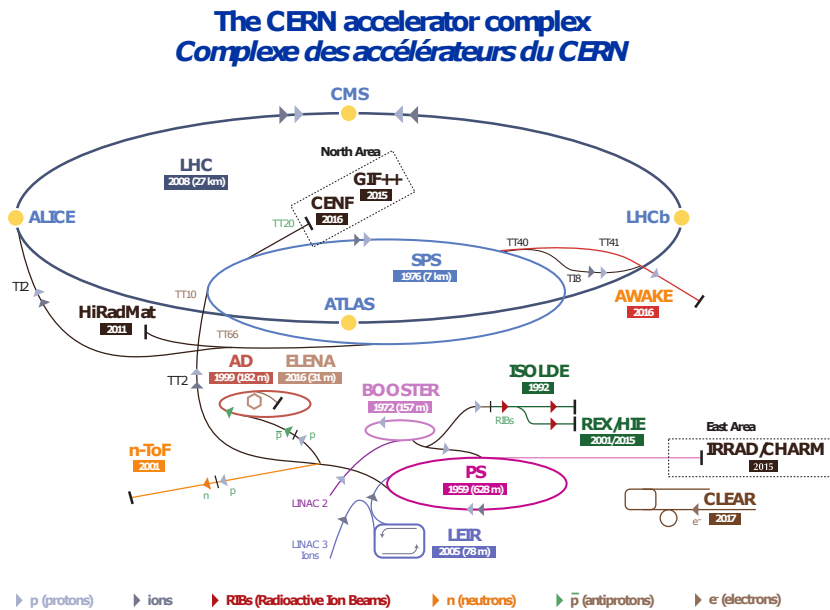


Figure 1: CERN accelerators complex.

A particle accelerator consists of a large number of magnets and other electromagnetic devices that determine the particle trajectory through the accelerator. Each device is described by its own equations of motion, which are derived from the exact Hamiltonian of the system. However, these equations cannot be solved exactly in general. For this purpose, a number of approximations are introduced in order to simplify the solution process and to speed up the computation. These approximations are only valid under certain conditions and ignore many non-linear effects.

Nonetheless, they are often considered to be appropriate and find widespread use in beam physics.

In order to evaluate the long term stability of particle beams and to simulate particle losses, particle tracking algorithms are applied, which simulate the motion of the particle through each magnet in the accelerator. The effect of the magnet on the motion of the particle is modelled in what will be referred to as a *map*. Indeed, each magnet can be represented by a mapping which maps the initial coordinates at the entrance of the magnet to the final coordinates at the exit of the magnet. If \mathbf{w}_i denotes the initial coordinates, \mathbf{w}_f the final coordinates and M the map of a magnet, this mapping can be denoted as:

$$\mathbf{w}_f = M(\mathbf{w})\mathbf{w}_i.$$

The mathematical form of these maps varies depending on the approximations used in their derivations. In a linear case they can be expressed in matrix form. Generally, the maps representing specific magnets are non-linear. The motion of any Hamiltonian system is represented by a symplectic map, which implies that the volume in phase space is conserved by the time evolution of these systems, as guaranteed by the Liouville theorem.

The typical procedure followed in a particle tracking operation, in the case of accelerator elements that cannot be represented by a linear map, is sketched in fig. 2. The field data of such accelerator elements are generally expressed in terms of magnetic field at discrete grid points in space, computed either numerically, using dedicated electromagnetic solvers, or measured. Then, in order to retrieve the complete behavior of the field, these data are interpolated. The information retrieved is used in the equations of motion of the system to compute the particle's trajectory, defining in this way the particle dynamics. Finally, tracking algorithms, simulating the particles passing repeatedly inside the element, can be applied. In



Figure 2: Standard tracking procedure.

order to track the motion of the particles effectively, numerical approximations are usually necessary.

On one hand, electric and magnetic fields are too complex to be expressed in terms of analytic functions, so that, as we already mentioned, the field is numerically evaluated at a discrete set of points. An estimation of its value at a generic point can then be provided using either reconstruction or interpolation methods. Performing particle tracking with interpolated magnetic field may cause some problems. For example, the interpolated fields may not satisfy the divergence-free condition,

because of measurement errors or an improper interpolation itself. In this case, results of the tracking will not correspond to the real dynamics of the system. In particular, if the divergence free condition over the magnetic field is not satisfied by the reconstructed magnetic field, Liouville theorem does not hold anymore. If the volume occupied by the particles in phase space is not conserved, the consequence is an artificial growth or damping of the size of a cell in phase space, due to this bad approximation of the field values.

The importance of preserving $\nabla \cdot \mathbf{B} = 0$ was pointed out in many fields: for example, Brackbill and Barnes [BB80] showed that in the context of magnetohydrodynamics, the failure of this condition may lead to unphysical sources orthogonal to the field in the model. As stated in [McN11], the key fact is that the discrete point values of the magnetic field do not have a defined derivative, so, if $\nabla \cdot \mathbf{B} = 0$ is respected, depends entirely on the method used to produce the continuous representation of the magnetic field from which derivatives are taken. We know that Liouville theorem holds under specific conditions: any forces encountered by the particles must be conservative and differentiable (i.e. “smooth”), they must not change the total energies of the particles and they cannot be abrupt forces such as those arising from collisions. According to [BB80], if the condition $\nabla \cdot \mathbf{B} = 0$ is not respected, it can be proved that the energy integral is not in conservation form. As a consequence, the energy of an isolated system is not a constant of the motion and Liouville theorem does not hold.

On the other hand, an accurate description of the particle dynamics is achieved using numerical methods which solve the Hamilton Ordinary Differential Equations (ODE), called integration methods. Hamiltonian integrators can be symplectic or non-symplectic. The numerical approximation to a Hamiltonian system obtained from an ordinary numerical method (non-symplectic) may introduce a non-Hamiltonian perturbation in the long term. This means that a Hamiltonian system integrated using an ordinary numerical method may become a dissipative system, with completely different long-term behaviour. This problem has led to the introduction of methods of symplectic integration for Hamiltonian systems, which do preserve the features of the Hamiltonian structure, imposing each step of the integration to be a canonical transformation.

Interpolation and integration methods influence each other and the overall accuracy of the particles tracking. An appropriate choice of both these aspects is necessary in order to obtain accurate results. In this thesis, the impact of field reconstruction and interpolation techniques was studied during the internship at CERN, while a comparison of the accuracy of several integration methods was carried out in the final part of the thesis work at Politecnico.

The main goal of the work done at CERN was to provide reconstruction and post-processing algorithms for the vector potential of the field on a discrete grid, preserving the divergence-free characteristics, and prove that these techniques, together with proper interpolation methods and accurate integration algorithms, are able to improve volume preservation in phase space, also for non-linear field maps. The procedure described in fig. 2, was completed with extra steps, in which the magnetic field data are reconstructed in such a way that the final magnetic

field preserves its divergence free properties (see fig. 3).

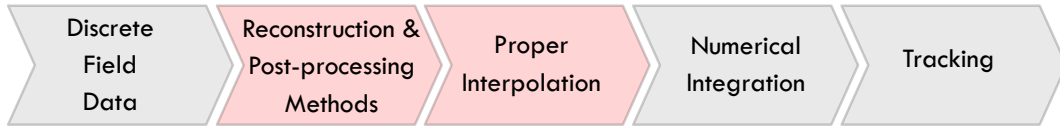


Figure 3: New tracking procedure.

This part of the work was performed improving and completing the simulation code “RF-Track” [Lat16], developed at CERN by Dr. Andrea Latina, which implements particle tracking through accelerators, using field maps of various kind. Two alternative techniques to achieve divergence free reconstructions were considered and their impact was assessed by numerical simulations.

On the other hand, the main goal of the work done at Politecnico was to study the accuracy and efficiency of different integration methods and their interactions with the interpolation techniques. Indeed, as pointed out in [Sim+19], if the errors induced by field reconstruction and interpolation are significant, non symplectic integration methods appear to be competitive with symplectic ones (even on relatively long integrations). For this reason, implicit high-order symplectic integrators and explicit Runge Kutta methods were compared, in order to assess their efficiency and their computational costs. In this case, a magnetic field, whose analytic expression is known, was considered. It has been shown that the accuracy of the field reconstruction and interpolation techniques are both limiting factors for the accuracy of the particle tracking procedures.

This thesis is organized as follows. In chapter 1, the system we considered in our tracking analysis is presented. In chapter 2, some general results concerning the particle dynamics in Hamiltonian systems are recalled. Also, the particular Hamiltonian used in this thesis is presented. In chapter 3, an overview of the numerical methods considered is given. The two reconstruction and post-processing methods developed at CERN are explained in detail. Afterwards, the quadrature formulae and the ODE techniques applied are introduced. In chapter 4, the results of the tests over the post-processing methods and the different integrators are shown.

Chapter 1

Magnetic Field and Coils System

This chapter provides the reader with an overview of the classical theory of electromagnetism (section 1.1) and a presentation of the main characteristics of the system for which we tested our algorithms, which is a system of coils leading opposite currents (section 1.3).

1.1 The Maxwell's Equations

In the following section we are going to introduce the basic concepts and formalism used in the treatment of the magnetic field. The reader is referred to [Jac99] for a more detailed description. Unless specified otherwise, the system of measurement adopted is the International System of Units (SI), reported in Appendix (A).

The Maxwell equations describe the electric and magnetic fields arising from distributions of electric charges and currents, and how those fields change in time. They can be written in a differential form as:

$$\begin{aligned}\nabla \cdot \mathbf{E} &= \frac{\rho}{\varepsilon} \\ \nabla \cdot \mathbf{B} &= 0 \\ \nabla \times \mathbf{E} &= - \frac{\partial \mathbf{B}}{\partial t} \\ \nabla \times \mathbf{B} &= \mu \mathbf{j} + \mu \varepsilon \frac{\partial \mathbf{E}}{\partial t}\end{aligned}\tag{1.1}$$

where \mathbf{E} is the electric field, \mathbf{B} is the magnetic field, ρ is the charge density, ε is the vacuum permittivity, μ is the vacuum permeability and \mathbf{j} is the current density. In this thesis, we consider stationary magnetic fields in a region free of sources or currents. In these conditions, the equations (1.1) become:

$$\begin{aligned}
\nabla \cdot \mathbf{E} &= 0 \\
\nabla \cdot \mathbf{B} &= 0 \\
\nabla \times \mathbf{E} &= 0 \\
\nabla \times \mathbf{B} &= 0
\end{aligned} \tag{1.2}$$

We assume to be working in a *simply connected* domain. A domain Ω in \mathbb{R}^3 is said to be simply connected if it is both contour-wise and surface-wise simply connected [BN82].

Definition 1.1.1. A domain Ω is said to be *contour-wise simply connected* (c.s.c.) if every closed regular curve Γ contained in Ω is the boundary of an open surface S entirely contained in Ω . In a c.s.c. domain every irrotational vector field can be written as the gradient of a global one-valued \mathcal{C}^2 magnetic scalar potential:

$$\nabla \times \mathbf{v} = \mathbf{0} \text{ in } \Omega \text{ c.s.c.} \Rightarrow \mathbf{v} = -\nabla u, \quad u \text{ one-valued in } \Omega.$$

Definition 1.1.2. A domain Ω is said to be *surface-wise simply connected* (s.s.c.) if every closed regular surface S contained in Ω is the boundary of a domain D entirely contained in Ω . In a s.s.c. domain a \mathcal{C}^1 solenoidal (divergence-free) vector field can be written as the curl of a \mathcal{C}^2 global one-valued vector potential:

$$\nabla \cdot \mathbf{v} = \mathbf{0} \text{ in } \Omega \text{ s.s.c.} \Rightarrow \mathbf{v} = \nabla \times \mathbf{V}, \quad \mathbf{V} \text{ one-valued in } \Omega.$$

Thanks to the regularity of the domain, the magnetic field \mathbf{B} , which is divergence-free ($\nabla \cdot \mathbf{B} = 0$), can be expressed as the curl of some other vector field \mathbf{A} , called the *magnetic vector potential*:

$$\mathbf{B} = \nabla \times \mathbf{A}.$$

Since the magnetic field is also irrotational ($\nabla \times \mathbf{B} = 0$), it can also be written as the gradient of a scalar potential φ , called the *magnetic scalar potential*:

$$\mathbf{B} = -\nabla \varphi.$$

It can be proved that the vector potential is defined up to a constant and up to a gradient of a scalar function. Indeed, if we define a scalar function ψ and $\mathbf{A}' = \mathbf{A} + \nabla \psi$, we can write:

$$\nabla \times \mathbf{A}' = \nabla \times (\mathbf{A} + \nabla \psi) = \nabla \times \mathbf{A} = \mathbf{B},$$

because the curl of a gradient is zero. Similarly, the magnetic scalar potential is defined up to a constant. Indeed, defining g a constant function and $\varphi' = \varphi + g$, we get:

$$\nabla \varphi' = \nabla(\varphi + g) = \nabla \varphi = -\mathbf{B},$$

because the gradient of a constant function is null. A particular choice of the scalar and vector potentials is called a choice of *gauge*.

1.2 Transfer Matrix for a Solenoid

Let us consider a solenoid as shown in fig. 1.1, with length L and N coils leading a current I . The magnetic field, considering the cylindrical coordinates (r, z, ϑ) , is composed by a radial and an axial component, called B_r and B_z , while $B_\vartheta = 0$ because of the axial symmetry of the system. Inside the body of the solenoid, the axial component is constant and equal to:

$$\oint_C \mathbf{B} \cdot d\mathbf{l} = \mu_0 I \quad \Rightarrow \quad B_{z0} = \mu_0 \frac{N}{L} I \quad (1.3)$$

where C is the rectangular circulation path in fig. 1.1. However, real solenoids present also an entry and an exit region. In these regions one has:

$$\oint_S \mathbf{B} \cdot d\mathbf{s} = 0 \quad \Rightarrow \quad B_z \pi r^2 + 2\pi r \int B_r dz = 0 \quad \Rightarrow \quad B_r = -\frac{r}{2} \frac{dB_z}{dz}, \quad (1.4)$$

where S is the integration volume shown in fig. 1.1. Indeed, a variation of the magnetic field along the axis of the solenoid gives rise to a radial component of the magnetic field. This term is responsible for the end effects seen by particles entering or leaving a solenoid, since, at the end of a solenoid, the field falls from a given value B_{z0} to zero. As an approximation, one can look at the solenoid as split

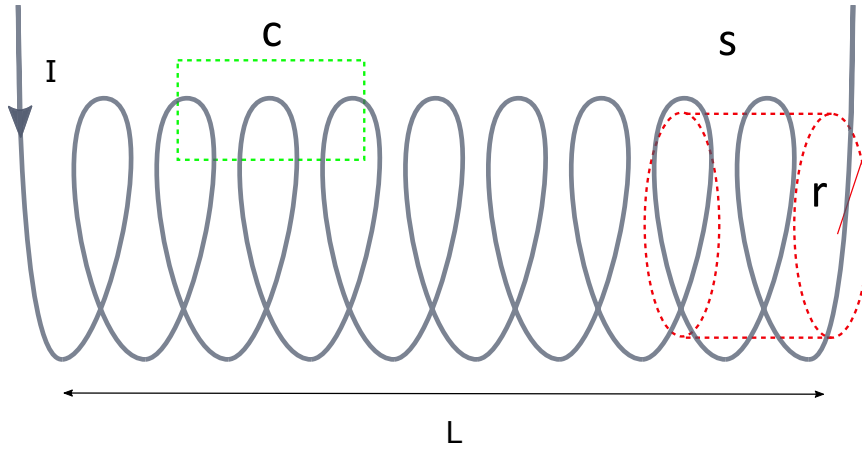


Figure 1.1: Circulation structure in the solenoid.

in three parts: an entry region, a body region and an exit region (see fig. 1.2). We first consider the behavior of a particle entering the solenoid. We assume that its velocity is aligned with the direction z of the axis of the solenoid. In this region, we have to look at the action of the radial field which imparts an angular momentum on the beam, resulting in a change of the azimuthal momentum. Indeed, in the absence of electrical fields, the Lorentz force is given by:

$$\frac{d\mathbf{p}}{dt} = q\mathbf{v} \times \mathbf{B}. \quad (1.5)$$

As we previously said, the particle is moving along the z axis with velocity v_z ($v_r = v_\vartheta = 0$). Equation (1.5) becomes:

$$\frac{dp_\vartheta}{dt} = qv_z B_r, \quad (1.6)$$

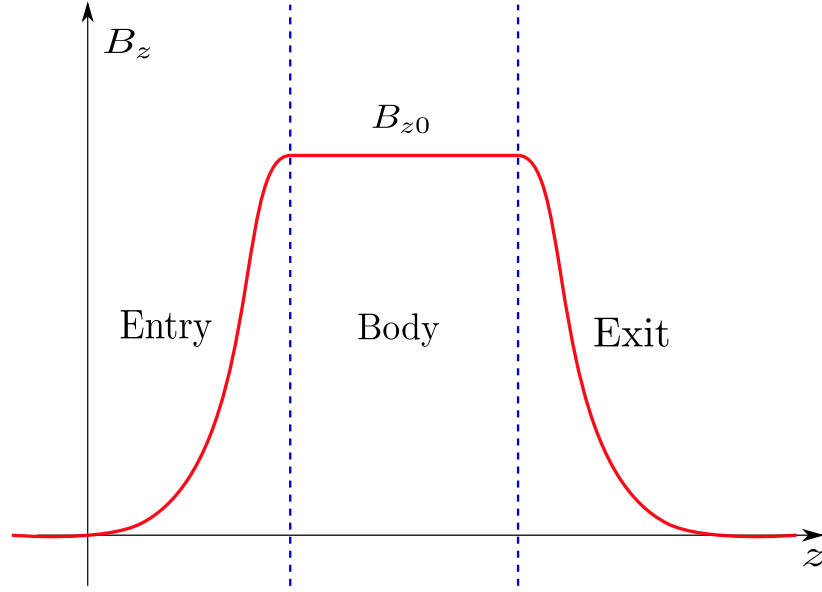


Figure 1.2: Subdivision of the solenoid magnetic field along the z axis.

where ϑ indicates azimuthal direction and $p_r = p_z = 0$. After substituting the expression of B_r given in (1.4), we can rewrite (1.6) as:

$$\frac{dp_\vartheta}{dz} \frac{dz}{dt} = qv_z \left(-\frac{r}{2} \frac{dB_z}{dz} \right),$$

ending up with:

$$\frac{dp_\vartheta}{dz} = -\frac{qr}{2} \frac{dB_z}{dz}.$$

Afterwards, integrating in z over the entrance region, one obtains a variation of the azimuthal momentum equal to:

$$\Delta p_\vartheta = -\frac{qr}{2} B_z. \quad (1.7)$$

As a consequence, the variation of the magnetic field, which varies for instance from zero to a given value at the entrance of a solenoid, induces a transverse kick in the azimuthal momentum. In other words, the particles crossing the fringe fields experience a transverse force. This phenomenon is responsible for the particles entering with a velocity parallel to the axis of the solenoid to start spiralling inside the solenoid. Finally, we can retrieve the vertical and horizontal components of the momentum as:

$$\begin{aligned} \Delta p_x &= -\Delta p_\vartheta \sin(\vartheta) = \frac{qr}{2} B_z \sin(\vartheta) = \frac{qB_z}{2} y, \\ \Delta p_y &= \Delta p_\vartheta \cos(\vartheta) = -\frac{qr}{2} B_z \cos(\vartheta) = -\frac{qB_z}{2} x. \end{aligned}$$

To simplify notation, we define:

$$K = \frac{qB_z}{2P_0}, \quad (1.8)$$

where P_0 is called the *reference momentum*. Although the reference momentum can be chosen arbitrarily, a smart choice is to set P_0 as the momentum that particles are intended to have by design. Then, we define $P_0 = p_z$. Finally, we get:

$$\begin{aligned} x' &= \frac{dx}{dz} = \frac{\Delta p_x}{P_0} = \frac{qB_z}{2P_0}y = Ky; \\ y' &= \frac{dy}{dz} = -Kx; \end{aligned} \quad (1.9)$$

The transfer matrices for the transverse variables (x, x', y, y') in the entry and the exit regions are then:

$$M_{\text{entry}} = \begin{pmatrix} 1 & 0 & 0 & 0 \\ 0 & 1 & K & 0 \\ 0 & 0 & 1 & 0 \\ -K & 0 & 0 & 1 \end{pmatrix}, \quad M_{\text{exit}} = \begin{pmatrix} 1 & 0 & 0 & 0 \\ 0 & 1 & -K & 0 \\ 0 & 0 & 1 & 0 \\ K & 0 & 0 & 1 \end{pmatrix}.$$

In the body of the solenoid the field is constant and directed along the z axis. The motion of a particle is circular in the xy plane. The geometry we are considering is the one shown in fig. 1.3. v_ϑ is the transverse velocity, v_x and v_y are its transverse plane components, ρ_ϑ is the radius of the coil and φ is the transverse angle. Over

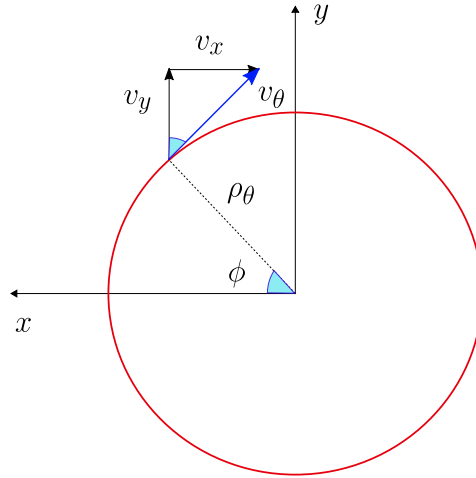


Figure 1.3: Transverse section of the solenoid.

the length L of the solenoid, the total rotation angle is:

$$\vartheta = \omega t_L = \frac{-qB_z}{m} \frac{L}{v_z} = -\frac{qB_z}{P_0} L = 2KL, \quad (1.10)$$

where ω is the angular velocity and t_L the time needed to go through the solenoid. Let us define the quantities x' and y' , which are the derivatives of x and y with respect to z . The index i and f indicate the initial and final position:

$$\begin{aligned} x'_f &= x'_i \cos(\vartheta) - y'_i \sin(\vartheta), \\ y'_f &= x'_i \sin(\vartheta) + y'_i \cos(\vartheta). \end{aligned} \quad (1.11)$$

Setting:

$$\begin{aligned}\cos \varphi &= \frac{v_{y_i}}{v_\vartheta} = \frac{v_{y_i} v_z}{v_z v_\vartheta} = \frac{dy}{dz} \frac{L}{\rho_\vartheta t_L \omega} = y'_i \frac{1}{\rho_\vartheta} \frac{L}{\vartheta}, \\ \sin \varphi &= -\frac{v_{x_i}}{v_\vartheta} = -\frac{v_{x_i} v_z}{v_z v_\vartheta} = -x'_i \frac{1}{\rho_\vartheta} \frac{L}{\vartheta},\end{aligned}$$

the position transformation is given by:

$$\begin{aligned}\Delta x &= x_f - x_i \\ &= \rho_\vartheta [\cos(\varphi + \vartheta) - \cos(\varphi)] \\ &= \rho_\vartheta [\cos \varphi (\cos \vartheta - 1) - \sin \varphi \sin \vartheta] \\ &= \rho_\vartheta [y'_i \frac{1}{\rho_\vartheta} \frac{L}{\vartheta} (\cos \vartheta - 1) + x'_i \frac{1}{\rho_\vartheta} \frac{L}{\vartheta} \sin \vartheta] \\ &= x_i \frac{L}{\vartheta} \sin \vartheta - y'_i \frac{L}{\vartheta} (1 - \cos \vartheta).\end{aligned}\tag{1.12}$$

The same procedure can be followed also for the y variable. Finally, the transfer matrix for the body of the solenoid is:

$$\begin{aligned}M_{\text{body}} &= \begin{pmatrix} 1 & \frac{L}{\vartheta} \sin \vartheta & 0 & -\frac{L}{\vartheta} (1 - \cos \vartheta) \\ 0 & \cos \vartheta & 0 & -\sin \vartheta \\ 0 & \frac{L}{\vartheta} (1 - \cos \vartheta) & 1 & \frac{L}{\vartheta} \sin \vartheta \\ 0 & \sin \vartheta & 0 & \cos \vartheta \end{pmatrix} \\ &= \begin{pmatrix} 1 & \frac{\sin 2KL}{2K} & 0 & \frac{(1 - \cos 2KL)}{2K} \\ 0 & \cos 2KL & 0 & -\sin 2KL \\ 0 & -\frac{(1 - \cos 2KL)}{2K} & 1 & \frac{\sin 2KL}{2K} \\ 0 & -\sin 2KL & 0 & \cos 2KL \end{pmatrix}.\end{aligned}$$

In this way, setting:

$$C = \cos(KL), \quad S = \sin(KL),$$

we can obtain the transfer matrix for a solenoid as:

$$M_{\text{sol}} = M_{\text{exit}} \cdot M_{\text{body}} \cdot M_{\text{entry}} = \begin{pmatrix} C^2 & \frac{SC}{K} & SC & \frac{S^2}{K} \\ -KSC & C^2 & -KS^2 & SC \\ -SC & -\frac{S^2}{K} & C^2 & \frac{SC}{K} \\ KS^2 & -SC & -KSC & C^2 \end{pmatrix}.\tag{1.13}$$

The transfer matrix of a solenoid shows full coupling of the components in the transversal direction. Physically, particles moving through a solenoid follow helical trajectories, performing cyclotron oscillations around the field lines.

From (1.13) it is possible to prove that solenoids are able to focus both transverse planes, simultaneously. Indeed, following the thin lens approximation, we can consider the length L , hence ϑ , small, and keep the first term of the Taylor series for the cosine and sine. The matrix takes then the form [Wie07]:

$$M_{\text{sol}}^{\text{thin}} = \begin{pmatrix} 1 & 0 & 0 & 0 \\ -1/f & 1 & 0 & 0 \\ 0 & 0 & 1 & 0 \\ 0 & 0 & -1/f & 1 \end{pmatrix},\tag{1.14}$$

with $\frac{1}{f} = K^2 L = \left(\frac{qB_z}{2P_0}\right)^2 L$. This property is extremely useful in particle accelerators, in which this double focusing is generally achieved with a sequence of two rotated quadrupoles. However, the price that has to be paid for this ability is the coupling of the motion over the transverse plane. This fact is complicating the dynamics of particles, allowing the passage of errors from the x -axis to the y -axis and vice versa.

In order to remove the coupling, one can consider two consecutive solenoids with opposite magnetic fields B_z and $-B_z$. Indeed, calling M_{sol}^- the matrix obtained from (1.13) evaluated setting:

$$\begin{aligned} K^- &= -\frac{qB_z}{2P_0} = -K, \\ C^- &= \cos(K^-L) = \cos(KL) = C, \\ S^- &= \sin(K^-L) = -\sin(KL) = -S, \end{aligned}$$

we have:

$$M_{sol}^- = \begin{pmatrix} C^2 & \frac{CS}{K} & -CS & -\frac{S^2}{K} \\ -CSK & C^2 & S^2K & -CS \\ CS & \frac{S^2}{K} & C^2 & \frac{CS}{K} \\ -S^2K & CS & -CSK & C^2 \end{pmatrix}.$$

The product between the two matrices $M_{sol} \cdot M_{sol}^-$ is given by:

$$\begin{pmatrix} C^4 - S^4 & \frac{2CS^3}{K} + \frac{2C^3S}{K} & 0 & 0 \\ -2CS^3K - 2C^3SK & C^4 - S^4 & 0 & 0 \\ 0 & 0 & C^4 - S^4 & \frac{2CS^3}{K} + \frac{2C^3S}{K} \\ 0 & 0 & -2CS^3K - 2C^3SK & C^4 - S^4 \end{pmatrix}.$$

Simplifying the trigonometric expressions, the transfer matrix of a cell composed by two opposite solenoids can be written as:

$$\begin{pmatrix} 2\cos(KL)^2 - 1 & \frac{4P \cos(KL) \sin(KL)}{Bq} & 0 & 0 \\ -\frac{Bq \cos(KL) \sin(KL)}{P} & 2\cos(KL)^2 - 1 & 0 & 0 \\ 0 & 0 & 2\cos(KL)^2 - 1 & \frac{4P \cos(KL) \sin(KL)}{Bq} \\ 0 & 0 & -\frac{Bq \cos(KL) \sin(KL)}{P} & 2\cos(KL)^2 - 1 \end{pmatrix},$$

which can be finally written as:

$$M = \begin{pmatrix} 2C^2 - 1 & \frac{2SC}{K} & 0 & 0 \\ -2KSC & 2C^2 - 1 & 0 & 0 \\ 0 & 0 & 2C^2 - 1 & \frac{2SC}{K} \\ 0 & 0 & -2KSC & 2C^2 - 1 \end{pmatrix}. \quad (1.15)$$

1.3 Coils System

Solenoids are interesting elements but it is not easy to work directly with them: the coupling of the motion over the transverse plane allows the passage of errors from the x -axis to the y -axis and vice versa, resulting in a complicated dynamics of the particle motion. For this reason we focused on a particular system of coils leading opposite currents. A single coil can be formally considered as the approximation of a solenoid with a single turn of wire, and, as a consequence, the considerations about coupling and decoupling made in section 1.2 apply also to this system. Considering a system composed by a sequence of coils provides us multiple advantages, like periodicity, exact knowledge of the transport matrix and of the complete analytic field equations, including the so called fringe fields. This last characteristic is of crucial importance. The Maxwell equations require the presence of a transition region between a null field and a solenoidal or multipole magnetic field. These transition regions are usually known as fringe fields. Accurate models of an accelerator must include them, since they may have significant and complicated effects: they can introduce non-linearities in the equations of motion, or they can make a substantial contribution to the desired effects of the magnetic field [Wol14]. However, the mathematical description of a fringe field can be rather complicated. The study of a system of coils represents a way to overcome fringe field definition, since the magnetic field is known analytically everywhere in space.

In order to understand the behavior of such a system, let us consider the magnetic field generated by a pair of coils in two different situations. When the coils are leading the same current, their magnetic fields sum together as in figure 1.4. When

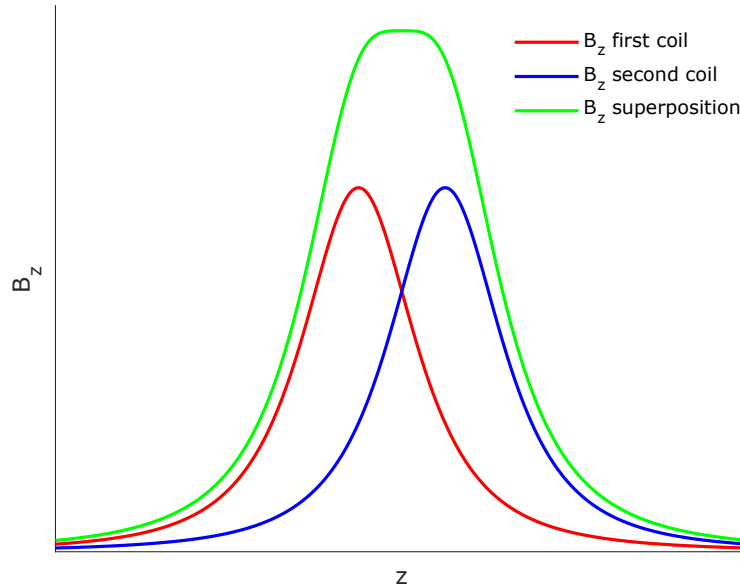


Figure 1.4: Magnetic field generated by two coils leading the same currents.

the system is composed by a large number of these coils (placed at an appropriate

distance from each other), we can approximate the system with a solenoid. Such a system is generating a uniform magnetic field, perpendicular to the coil's surface. As we saw in section 1.2, the particle dynamics can be approximated by linear equations and the motion in the horizontal and vertical direction (in the transverse plane) is strongly coupled.

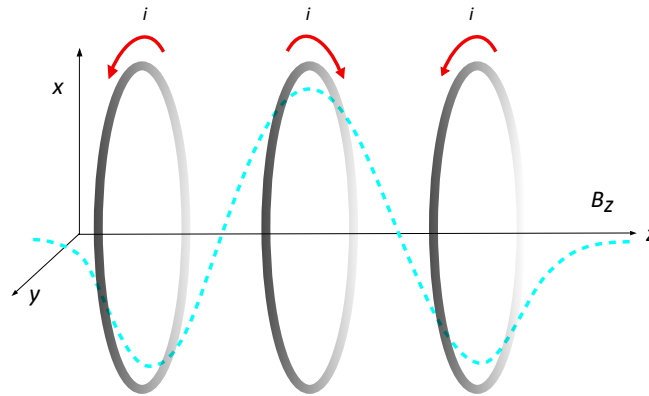


Figure 1.5: System of coils leading opposite currents.

Since each coil can be considered as the approximation of a solenoid with a single turn of wire, we decided to focus on a system of coils leading opposite currents (see fig. 1.5), so that the coupling effect could be cancelled (keeping anyways the knowledge about the fringe fields behavior). When two coils leading opposite currents are placed one next to the other, their magnetic fields sum together as in fig. 1.6. In this case, as it was proved in (1.15), the vertical and the horizontal

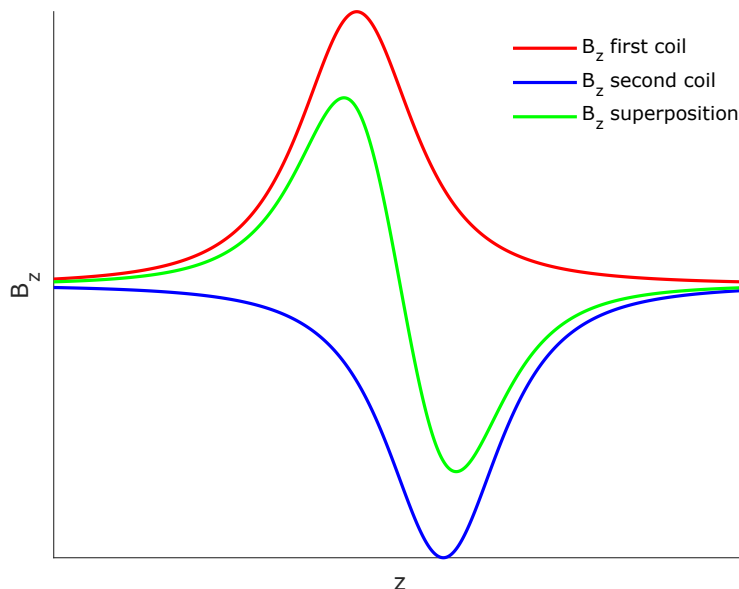


Figure 1.6: Magnetic field generated by two coils leading opposite currents.

motion of the particles passing through this system are decoupled.

1.4 Coils Equations

Following [Kun07], we will now derive the equations describing the magnetic field generated by a coil leading a certain current.

The magnetic field generated by a steady current loop can be expressed using the Biot–Savart law as:

$$\mathbf{B} = \frac{\mu_0}{4\pi} \int \frac{I d\mathbf{l} \times \mathbf{R}}{|\mathbf{R}|^3}. \quad (1.16)$$

where $d\mathbf{l}$ is the coil element, I is the steady current and \mathbf{R} is the distance from a given point on the loop to the observation point P . In order to find the analytic

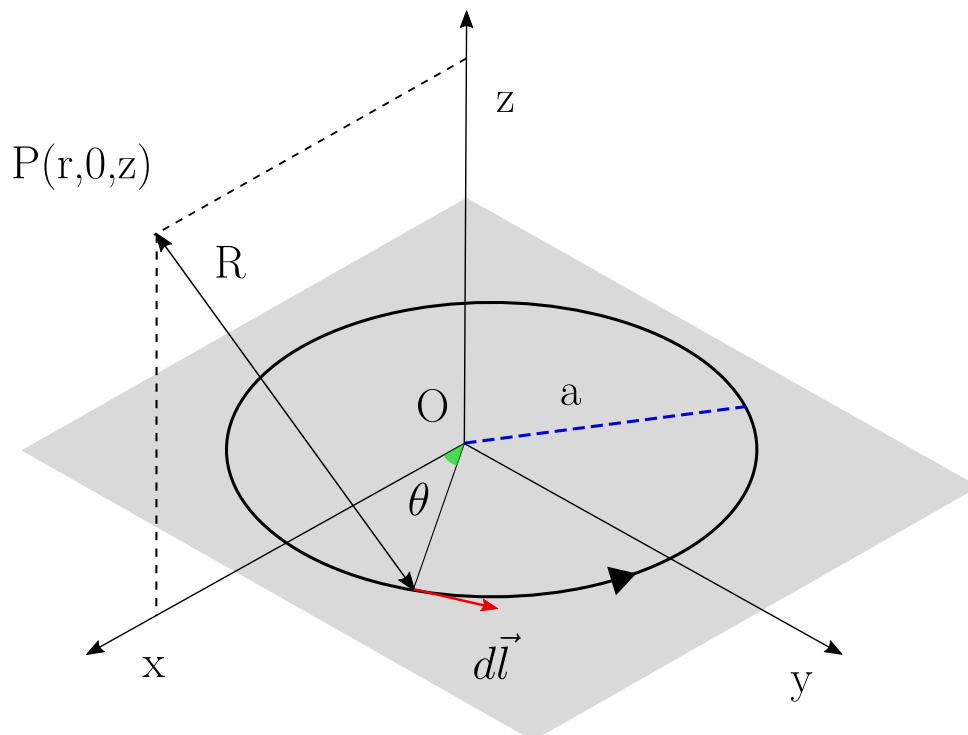


Figure 1.7: Coil reference system

expression of the field, the integral in (1.16) has to be computed. This can be done in terms of *complete elliptic integrals* of the first and second kind.

1.4.1 Elliptic integrals

Elliptic integrals originally arose in connection with the problem of giving the arc length of an ellipse [AWH13]. These special functions can be computed numerically (see [AS65]) and, in general, they are expressed as a function of the parameter k , called elliptic modulus or eccentricity. We can distinguish different kinds of elliptic integrals. In our study we will focus only on the complete elliptic functions of the

first and second kind. Assuming a k such that $0 < k^2 < 1$, the complete elliptic integral of the first kind is defined as:

$$K(k) = \int_0^{\frac{\pi}{2}} \frac{d\alpha}{\sqrt{1 - k^2 \sin^2 \alpha}}. \quad (1.17)$$

The complete elliptic integral of the second kind is:

$$E(k) = \int_0^{\frac{\pi}{2}} \sqrt{1 - k^2 \sin^2 \alpha} d\alpha. \quad (1.18)$$

We are now going to define the expressions for the derivative of $K(k)$ and $E(k)$, since they will be useful in the calculation of \mathbf{B} . The derivative of K is given by:

$$\frac{dK(k)}{dk} = \int_0^{\frac{\pi}{2}} \frac{k \sin^2 \alpha}{(1 - k^2 \sin^2 \alpha)^{\frac{3}{2}}} d\alpha. \quad (1.19)$$

Since

$$\frac{k \sin^2 \alpha}{(1 - k^2 \sin^2 \alpha)^{\frac{3}{2}}} = \frac{1}{k(1 - k^2 \sin^2 \alpha)^{\frac{3}{2}}} - \frac{1}{k\sqrt{1 - k^2 \sin^2 \alpha}},$$

we can rewrite (1.19) as:

$$\frac{dK(k)}{dk} = \int_0^{\frac{\pi}{2}} \frac{1}{k(1 - k^2 \sin^2 \alpha)^{\frac{3}{2}}} d\alpha - \int_0^{\frac{\pi}{2}} \frac{1}{k\sqrt{1 - k^2 \sin^2 \alpha}} d\alpha.$$

By definition of K , the second integral is $\frac{K}{k}$. It can be shown that [AWH13]:

$$E(k) = (1 - k^2) \int_0^{\frac{\pi}{2}} \frac{d\alpha}{(1 - k^2 \sin^2 \alpha)^{\frac{3}{2}}},$$

so that as a consequence:

$$\frac{dK(k)}{dk} = \frac{E(k)}{k(1 - k^2)} - \frac{K(k)}{k}. \quad (1.20)$$

The derivative of $E(k)$ is given by:

$$\frac{dE(k)}{dk} = - \int_0^{\frac{\pi}{2}} \frac{k \sin^2 \alpha}{\sqrt{1 - k^2 \sin^2 \alpha}} d\alpha.$$

Since

$$-\frac{k \sin^2 \alpha}{\sqrt{1 - k^2 \sin^2 \alpha}} = \frac{\sqrt{1 - k^2 \sin^2 \alpha}}{k} - \frac{1}{k\sqrt{1 - k^2 \sin^2 \alpha}},$$

we can rewrite and simplify the derivative as:

$$\begin{aligned} \frac{dE(k)}{dk} &= \int_0^{\frac{\pi}{2}} \frac{\sqrt{1 - k^2 \sin^2 \alpha}}{k} d\alpha - \int_0^{\frac{\pi}{2}} \frac{d\alpha}{k\sqrt{1 - k^2 \sin^2 \alpha}} \\ &= \frac{E(k)}{k} - \frac{K(k)}{k}. \end{aligned} \quad (1.21)$$

1.4.2 The Vector Potential

The computation of the magnetic field generated by a current loop in any point of the space will be obtained starting from the expression of its vector potential [Sha12], and then using the formula $\mathbf{B} = \nabla \times \mathbf{A}$. The expression for the vector potential is:

$$\mathbf{A} = \frac{\mu_0 I}{4\pi} \int \frac{d\mathbf{l}}{R}, \quad (1.22)$$

where $d\mathbf{l}$ is the coil element and R is the distance from any point on the loop to the point of observation P . Consider that a loop of radius a centered on the z axis and lying on a plane parallel to xy , as represented in figure 1.7. For simplicity, we will determine \mathbf{A} at a point P with coordinates $(r, 0, z)$. Choosing $y = 0$ or $x = 0$ does not change the final configuration, thanks to the cylindrical symmetry of the system. Moreover, in the most general case in which the vector potential is computed in a point $P = (x, y, z)$, the following demonstration will still be valid, as long as r will be imposed equal to $\sqrt{x^2 + y^2}$.

Denoting by ϑ the angle from the x axis to a generic point of the loop, the coordinates of the same point on the loop will be $(a \cos \vartheta, a \sin \vartheta, 0)$.

The distance from P to any point on the loop is given by:

$$\begin{aligned} R &= \sqrt{(r - a \cos \vartheta)^2 + a^2 \sin^2 \vartheta + z^2} = \\ &= \sqrt{r^2 - 2ar \cos \vartheta + a^2(\cos^2 \vartheta + \sin^2 \vartheta) + z^2} \\ &= \sqrt{r^2 + a^2 + z^2 - 2ar \cos \vartheta}. \end{aligned} \quad (1.23)$$

The length element along the coil is:

$$d\mathbf{l} = -a \sin \vartheta d\vartheta \hat{\mathbf{x}} + a \cos \vartheta d\vartheta \hat{\mathbf{y}}. \quad (1.24)$$

Substituting (1.23) and (1.24) in (1.22), we get:

$$\begin{aligned} \mathbf{A} &= \frac{\mu_0 I}{4\pi} \left[\int_0^{2\pi} \frac{-a \sin \vartheta d\vartheta}{\sqrt{r^2 + a^2 + z^2 - 2ar \cos \vartheta}} \hat{\mathbf{x}} \right. \\ &\quad \left. + \int_0^{2\pi} \frac{a \cos \vartheta d\vartheta}{\sqrt{r^2 + a^2 + z^2 - 2ar \cos \vartheta}} \hat{\mathbf{y}} \right]. \end{aligned} \quad (1.25)$$

One can prove by symmetry arguments that the overall contribution in the x direction is zero, canceling the first term in (1.25). Moreover, the component in the y direction integrated from 0 to 2π can be rewritten as twice the same function integrated from 0 to π . Finally, we can also switch to cylindrical coordinates, rewriting (1.25) as:

$$\mathbf{A} = \frac{\mu_0 I a}{2\pi} \int_0^\pi \frac{\cos \vartheta d\vartheta}{\sqrt{r^2 + a^2 + z^2 - 2ar \cos \vartheta}} \hat{\boldsymbol{\vartheta}}.$$

This integral will now be expressed in terms of elliptic functions. First of all, we can rewrite the denominator inside the integral as:

$$\sqrt{r^2 + a^2 + z^2 - 2ar \cos \vartheta} = \sqrt{(r+a)^2 + z^2 - 4ar \left(\frac{1 + \cos \vartheta}{2} \right)}.$$

Then, assuming $\vartheta = \pi - 2\alpha$, we have:

$$\cos \vartheta = -\cos(2\alpha) = -(1 - 2\sin^2 \alpha). \quad (1.26)$$

So, we can write:

$$(1 + \cos \vartheta) / 2 = \sin^2 \alpha.$$

Afterwards, factoring out $(r + a)^2 + z^2$, we get:

$$\sqrt{(r + a)^2 + z^2} \sqrt{1 - \frac{4ar}{(r + a)^2 + z^2} \sin^2 \alpha}.$$

If we define the parameter k as:

$$k = \sqrt{\frac{4ar}{(r + a)^2 + z^2}},$$

then the denominator becomes:

$$\frac{2\sqrt{ar}}{k} \sqrt{1 - k^2 \sin^2 \alpha}. \quad (1.27)$$

Concerning the numerator inside the integral in (1.25), it will be rewritten as (1.26). Putting together numerator and denominator and remembering $d\vartheta = -2d\alpha$, (1.25), we get:

$$\begin{aligned} \mathbf{A} &= \frac{\mu_0 I a}{2\pi} \int_0^\pi \frac{-2(1 - 2\sin^2 \alpha) d\alpha}{\frac{2\sqrt{ar}}{k} \sqrt{1 - k^2 \sin^2 \alpha}} \hat{\vartheta} \\ &= \frac{\mu_0 I k}{2\pi} \sqrt{\frac{a}{r}} \int_0^\pi \frac{-(1 - 2\sin^2 \alpha) d\alpha}{\sqrt{1 - k^2 \sin^2 \alpha}} \hat{\vartheta} \\ &= \frac{\mu_0 I k}{2\pi} \sqrt{\frac{a}{r}} \left[\int_0^{\frac{\pi}{2}} \frac{-d\alpha}{\sqrt{1 - k^2 \sin^2 \alpha}} + \int_0^{\frac{\pi}{2}} \frac{2\sin^2 \alpha d\alpha}{\sqrt{1 - k^2 \sin^2 \alpha}} \right] \hat{\vartheta}. \end{aligned}$$

The first term of the equation is (1.17), $K(k)$. The second term can be further reformulated as:

$$\frac{2\sin^2 \alpha}{\sqrt{1 - k^2 \sin^2 \alpha}} = \frac{1}{k^2} \left(\frac{1}{\sqrt{1 - k^2 \sin^2 \alpha}} - \sqrt{1 - k^2 \sin^2 \alpha} \right).$$

Therefore, for the second integral we get:

$$\frac{2}{k^2} \left[\int_0^{\frac{\pi}{2}} \frac{d\alpha}{\sqrt{1 - k^2 \sin^2 \alpha}} - \int_0^{\frac{\pi}{2}} \sqrt{1 - k^2 \sin^2 \alpha} d\alpha \right],$$

which is equivalent to:

$$\frac{2}{k^2} (K(k) - E(k)).$$

Finally, we can write:

$$\begin{aligned} \mathbf{A} &= \frac{\mu_0 I k}{2\pi} \sqrt{\frac{a}{r}} \left[-K(k) + \frac{2}{k^2} (K(k) - E(k)) \right] \hat{\vartheta} \\ &= \frac{\mu_0 I}{2\pi} \sqrt{\frac{a}{r}} \left[\left(-k + \frac{2}{k} \right) K(k) - \frac{2}{k} E(k) \right] \hat{\vartheta}. \end{aligned} \quad (1.28)$$

1.4.3 The Magnetic Field

We will now derive an expression for \mathbf{B} from the curl of the vector potential. In cylindrical coordinates, one has:

$$\begin{aligned}\nabla \times \mathbf{A} &= \frac{1}{r} \left(\frac{\partial A_z}{\partial \vartheta} - \frac{\partial A_\vartheta}{\partial z} \right) \hat{\mathbf{r}} + \left(\frac{\partial A_r}{\partial z} - \frac{\partial A_z}{\partial r} \right) \hat{\boldsymbol{\vartheta}} + \frac{1}{r} \left(\frac{\partial}{\partial r} r A_\vartheta - \frac{\partial A_r}{\partial \vartheta} \right) \hat{\mathbf{z}} \\ &= -\frac{\partial A_\vartheta}{\partial z} \hat{\mathbf{r}} + \frac{1}{r} \frac{\partial}{\partial r} (r A_\vartheta) \hat{\mathbf{z}},\end{aligned}$$

since \mathbf{A} has only a ϑ component. In order to compute each component, we first compute the derivative of k with respect to r and z .

$$\begin{aligned}\frac{\partial k}{\partial z} &= \frac{1}{2} \sqrt{\frac{(r+a)^2 + z^2}{4ar}} \cdot \frac{-8arz}{[(r+a)^2 + z^2]^2 k} \\ &= -\frac{k^3 z}{4ar}\end{aligned}\tag{1.29}$$

$$\begin{aligned}\frac{\partial k}{\partial r} &= \frac{1}{2} \sqrt{\frac{(r+a)^2 + z^2}{4ar}} \cdot \frac{4a[(r+a)^2 + z^2] - 8arz}{[(r+a)^2 + z^2]^2} \\ &= \frac{k}{2r} - \frac{k^3(r+a)}{4ar}.\end{aligned}\tag{1.30}$$

Starting from these expressions, we can compute the two components of the magnetic field. The radial component can be retrieved as:

$$\begin{aligned}-\frac{\partial A}{\partial z} &= -\frac{\mu_0 I}{2\pi} \sqrt{\frac{a}{r}} \left[-\left(1 + \frac{2}{k^2}\right) \frac{\partial k}{\partial z} K(k) + \left(\frac{2}{k} - k\right) \frac{\partial k}{\partial z} \frac{dK(k)}{dk} \right. \\ &\quad \left. + \frac{2}{k^2} \frac{\partial k}{\partial z} E(k) - \frac{2}{k} \frac{\partial k}{\partial z} \frac{dE(k)}{dk} \right].\end{aligned}\tag{1.31}$$

Substituting (1.20), (1.21) and (1.29) in (1.31):

$$\begin{aligned}-\frac{\partial A}{\partial z} &= -\frac{\mu_0 I}{2\pi} \sqrt{\frac{a}{r}} \left[\left(1 + \frac{2}{k^2}\right) \frac{k^3 z}{4ar} K(k) - \left(\frac{2}{k} - k\right) \frac{k^3 z}{4ar} \left(\frac{E(k)}{k(1-k^2)} - \frac{K(k)}{k} \right) - \right. \\ &\quad \left. \frac{2}{k^2} \frac{k^3 z}{4ar} E(k) + \frac{2}{k} \frac{k^3 z}{4ar} \left(\frac{E(k)}{k} - \frac{K(k)}{k} \right) \right]\end{aligned}$$

By expanding and simplifying, we get:

$$\begin{aligned}-\frac{\partial A}{\partial z} &= -\frac{\mu_0 I}{2\pi} \sqrt{\frac{a}{r}} \left[\frac{kz}{2ar} K(k) - \frac{2kz - k^3 z}{4ar(1-k^2)} E(k) \right] \\ &= -\frac{\mu_0 I k z}{4\pi \sqrt{ar^3}} \left[K(k) - \frac{2-k^2}{(1-k^2)} E(k) \right].\end{aligned}$$

We can now determine the z component of \mathbf{B} . We have to compute $\frac{\partial}{\partial r}(rA)$, where:

$$rA = \frac{\mu_0 I}{2\pi} \sqrt{ar} \left[\left(-k + \frac{2}{k} \right) K(k) - \frac{2}{k} E(k) \right],$$

so:

$$\begin{aligned} \frac{\partial}{\partial r}(rA) &= \frac{\mu_0 I}{4\pi} \sqrt{\frac{a}{r}} \left[\left(-k + \frac{2}{k} \right) K(k) - \frac{2}{k} E(k) \right] \\ &\quad + \frac{\mu_0 I}{2\pi} \sqrt{ar} \left[\left(-1 - \frac{2}{k^2} \right) \frac{\partial k}{\partial r} K(k) \right. \\ &\quad \left. + \left(-k + \frac{2}{k} \right) \frac{\partial k}{\partial r} \frac{dK(k)}{dk} + \frac{2}{k^2} \frac{\partial k}{\partial r} E(k) - \frac{2}{k} \frac{\partial k}{\partial r} \frac{dE(k)}{dk} \right]. \end{aligned} \quad (1.32)$$

Again, substituting (1.20), (1.21) and (1.29) in (1.32) we have:

$$\begin{aligned} \frac{\partial}{\partial r}(rA) &= \frac{\mu_0 I}{2\pi} \sqrt{\frac{a}{r}} \left[\left(\frac{1}{k} - \frac{k}{2} \right) K(k) - \frac{E(k)}{k} \right. \\ &\quad + \left(-\frac{2r}{k^2} - r \right) \left(\frac{k}{2r} - \frac{k^3(r+a)}{4ar} \right) K(k) \\ &\quad + \left(-kr + \frac{2r}{k} \right) \left(\frac{k}{2r} - \frac{k^3(r+a)}{4ar} \right) \left(\frac{E(k)}{k(1-k^2)} - \frac{K(k)}{k} \right) \\ &\quad \left. + \frac{2r}{k^2} \left(\frac{k}{2r} - \frac{k^3(r+a)}{4ar} \right) E(k) - \frac{2r}{k} \left(\frac{k}{2r} - \frac{k^3(r+a)}{4ar} \right) \left(\frac{E(k)}{k} - \frac{K(k)}{k} \right) \right]. \end{aligned}$$

This expression can be finally expanded and simplified as follows. Moreover, we also divided the expression by r to get the complete expression for \mathbf{B}_z :

$$\begin{aligned} \frac{1}{r} \frac{\partial}{\partial r}(rA) &= \frac{\mu_0 I}{2\pi} \sqrt{\frac{a}{r^3}} \left[\left(\frac{k(r+a) - ak}{2a} \right) K(k) \right. \\ &\quad \left. + \left(\frac{k^2(-2a - 2(r+a) + k^2(r+a) + 4a)}{4ak(1-k^2)} \right) E(k) \right] \\ &= \frac{\mu_0 I k r}{4\pi \sqrt{ar^3}} \left[K(k) + \frac{k^2(r+a) - 2r}{2r(1-k^2)} E(k) \right]. \end{aligned}$$

So, finally, the complete expression for the magnetic field is:

$$\begin{aligned} \mathbf{B}(r, z) &= \frac{\mu_0 I k}{4\pi \sqrt{ar}} \left[\frac{-z}{r} \left(K(k) - \frac{2-k^2}{2(1-k^2)} E(k) \right) \hat{\mathbf{r}} \right. \\ &\quad \left. + \left(K(k) + \frac{k^2(r+a) - 2r}{2r(1-k^2)} E(k) \right) \hat{\mathbf{z}} \right]. \end{aligned}$$

In order to make the expression more readable and to be consistent with the formalism used in the implementation we have used for the numerical experiments, we define:

$$\alpha = \frac{r}{a}, \quad \beta = \frac{z}{a}, \quad \gamma = \frac{z}{r}, \quad Q = (1 + \alpha)^2 + \beta^2, \quad B_0 = \frac{\mu_0 I}{2a}.$$

and

$$k = \sqrt{\frac{4ar}{(r+a)^2 + z^2}}.$$

The radial and longitudinal components of the magnetic field are then:

$$\begin{aligned} \mathbf{B}_r &= \frac{\mu_0 I k}{4\pi\sqrt{ar}} \left[\frac{-z}{r} \left(K(k) - \frac{2-k^2}{2(1-k^2)} E(k) \right) \right] \hat{\mathbf{r}} \\ &= \frac{B_0 \gamma}{\pi\sqrt{Q}} \left(\frac{2-k^2}{2(1-k^2)} E(k) - K(k) \right) \hat{\mathbf{r}} \\ &= \frac{B_0 \gamma}{\pi\sqrt{Q}} \left(\frac{1+\alpha^2+\beta^2}{Q-4\alpha} - K(k) \right) \hat{\mathbf{r}}; \end{aligned}$$

$$\begin{aligned} \mathbf{B}_z &= \frac{\mu_0 I k}{4\pi\sqrt{ar}} \left(K(k) + \frac{k^2(r+a) - 2r}{2r(1-k^2)} E(k) \right) \hat{\mathbf{z}} \\ &= \frac{B_0}{\pi\sqrt{Q}} \left(K(k) + \frac{4ar^2 + 4a^2r - 2r[(r+a)^2 + z^2]}{2r[(r+a)^2 + z^2] - 8ar^2} E(k) \right) \hat{\mathbf{z}} \\ &= \frac{B_0}{\pi\sqrt{Q}} \left(K(k) + \frac{1-\alpha^2-\beta^2}{Q-4\alpha} \right) \hat{\mathbf{z}}. \end{aligned}$$

Chapter 2

Hamiltonian Systems

The particle dynamics inside a beam line is ruled by the Hamilton equations. Therefore, in this chapter, following the presentation in [Lan+82], some definitions and properties of Hamiltonian systems are recalled.

A mechanical system with n degrees of freedom can be described by its generalized coordinates $\mathbf{q} \in \mathbb{R}^n$ and its generalized velocities $\dot{\mathbf{q}} \in \mathbb{R}^n$. The state of a system is characterized by the Lagrangian function $\mathcal{L}(\mathbf{q}, \dot{\mathbf{q}}, t)$. The most general formulation of the law governing the motion of mechanical systems is the *principle of least action*. According to this principle, a mechanical system occupying the positions described by $q^{(1)}$ and $q^{(2)}$ at instants t_1 and t_2 , is moving between these two position in such a way that [Lan+82]:

$$S(\mathbf{q}) = \int_{t_1}^{t_2} \mathcal{L}(\mathbf{q}, \dot{\mathbf{q}}, t) dt \quad (2.1)$$

is minimized. This integral S is called *action*.

Let us call $\mathbf{q} = \mathbf{q}(t)$ the trajectory for which S is minimized. A small variation of $\delta\mathbf{q}(t)$ will increase the value of S . This means that S is increased when $\mathbf{q}(t)$ is replaced by $\mathbf{q}(t) + \delta\mathbf{q}(t)$. Since at t_1 and t_2 all the functions $\mathbf{q}(t) + \delta\mathbf{q}(t)$ have to be equal to $q^{(1)}(t)$ and $q^{(2)}(t)$, it follows that:

$$\delta\mathbf{q}(t_1) = \delta\mathbf{q}(t_2) = 0. \quad (2.2)$$

The correspondent change in S is:

$$\delta S(\mathbf{q}) = \int_{t_1}^{t_2} \mathcal{L}(\mathbf{q} + \delta\mathbf{q}, \dot{\mathbf{q}} + \delta\dot{\mathbf{q}}, t) dt - \int_{t_1}^{t_2} \mathcal{L}(\mathbf{q}, \dot{\mathbf{q}}, t) dt.$$

When this difference is expanded in a power series, the necessary condition for S to have a minimum is that the first order terms are zero. Thus, the principle of least action can be written as:

$$\delta S(\mathbf{q}) = \delta \int_{t_1}^{t_2} \mathcal{L}(\mathbf{q}, \dot{\mathbf{q}}, t) dt = 0,$$

and also:

$$\delta S(\mathbf{q}) = \int_{t_1}^{t_2} \left(\frac{\partial \mathcal{L}}{\partial \mathbf{q}} \delta \mathbf{q} + \frac{\partial \mathcal{L}}{\partial \dot{\mathbf{q}}} \delta \dot{\mathbf{q}} \right) dt = 0.$$

Since $\delta \dot{\mathbf{q}} = \frac{d \delta \mathbf{q}}{dt}$, we obtain, integrating the second term by parts:

$$\delta S(\mathbf{q}) = \int_{t_1}^{t_2} \left(\frac{\partial \mathcal{L}}{\partial \mathbf{q}} - \frac{d}{dt} \frac{\partial \mathcal{L}}{\partial \dot{\mathbf{q}}} \right) \delta \mathbf{q} dt + \left[\frac{\partial \mathcal{L}}{\partial \dot{\mathbf{q}}} \delta \mathbf{q} \right]_{t_1}^{t_2} = 0.$$

Remembering the condition (2.2), we obtain:

$$\frac{d}{dt} \left(\frac{\partial \mathcal{L}}{\partial \dot{\mathbf{q}}} \right) - \frac{\partial \mathcal{L}}{\partial \mathbf{q}} = 0. \quad (2.3)$$

These n different equations are known as *Euler-Lagrange equations*. Once the Lagrangian is known, they allow to define the equations of motion.

In Hamiltonian mechanics, the dynamics of a given system is usually described in terms of generalized coordinates and momenta of the system [GPS02]. To perform this change of independent variables, we have to apply a *Legendre transformation*. The conjugate momenta are defined as:

$$p_i = \frac{\partial \mathcal{L}}{\partial \dot{q}_i}(\mathbf{q}, \dot{\mathbf{q}}, t) \quad i = 1, \dots, n. \quad (2.4)$$

The total differential of the Lagrangian can be written as:

$$\begin{aligned} d\mathcal{L} &= \frac{\partial \mathcal{L}}{\partial \mathbf{q}} d\mathbf{q} + \frac{\partial \mathcal{L}}{\partial \dot{\mathbf{q}}} d\dot{\mathbf{q}} + \frac{\partial \mathcal{L}}{\partial t} dt \\ &= \dot{\mathbf{p}} d\mathbf{q} + \mathbf{p} d\dot{\mathbf{q}} + \frac{\partial \mathcal{L}}{\partial t} dt. \end{aligned} \quad (2.5)$$

Working on the last expression, it is possible to retrieve the equivalent form:

$$d(\mathbf{p} \dot{\mathbf{q}} - \mathcal{L}) = -\dot{\mathbf{p}} d\mathbf{q} + \dot{\mathbf{q}} d\mathbf{p} - \frac{\partial \mathcal{L}}{\partial t} dt. \quad (2.6)$$

The argument of the differential represents the energy of the system in terms of generalized coordinates and momenta, which is also called *Hamiltonian* of the system:

$$H(\mathbf{p}, \mathbf{q}, t) = \mathbf{p} \dot{\mathbf{q}} - \mathcal{L}(\mathbf{q}, \dot{\mathbf{q}}, t). \quad (2.7)$$

Substituting (2.7) in (2.6), we have:

$$dH = -\dot{\mathbf{p}} d\mathbf{q} + \dot{\mathbf{q}} d\mathbf{p} - \frac{\partial \mathcal{L}}{\partial t} dt. \quad (2.8)$$

It is also interesting to compute the differential of (2.7):

$$\begin{aligned} dH &= \dot{q}_i dp_i + p_i d\dot{q}_i - d\mathcal{L} \\ &= \dot{q}_i dp_i + p_i d\dot{q}_i - \frac{\partial \mathcal{L}}{\partial q_i} dq_i - \frac{\partial \mathcal{L}}{\partial p_i} dp_i - \frac{\partial \mathcal{L}}{\partial t} dt \\ &= -\frac{\partial \mathcal{L}}{\partial q_i} dq_i + \dot{q}_i dp_i - \frac{\partial \mathcal{L}}{\partial t} dt \\ &= \frac{\partial H}{\partial q_i} dq_i + \frac{\partial H}{\partial p_i} dp_i + \frac{\partial H}{\partial t} dt. \end{aligned}$$

from which, comparing it with (2.8), we can retrieve the so called *Hamilton equations of motion* or *canonical equations* :

$$\begin{aligned}\frac{\partial H}{\partial p_i} &= \dot{q}_i \\ -\frac{\partial H}{\partial q_i} &= \frac{\partial \mathcal{L}}{\partial q_i} = \dot{q}_i \\ \frac{\partial H}{\partial t} &= -\frac{\partial \mathcal{L}}{\partial t}\end{aligned}\tag{2.9}$$

where q_i are the coordinates of the particle ($i = 1 \dots n$ in an n -dimensional space), p_i are the components of the momentum, and $H(\mathbf{q}, \mathbf{p}, t)$ is the Hamiltonian. The Hamilton equations can also be rewritten in a compact form as:

$$\dot{\mathbf{w}} = S \nabla H(\mathbf{w}) = -S^{-1} \nabla H(\mathbf{w}) = -S^T \nabla H(\mathbf{w}),\tag{2.10}$$

where $\mathbf{w} = (q_1, \dots, q_n, p_1, \dots, p_n) \in \mathbb{R}^{2n}$ and:

$$S = \begin{bmatrix} \mathbf{0} & \mathbf{I}_n \\ -\mathbf{I}_n & \mathbf{0} \end{bmatrix} \in \mathbb{R}^{2n \times 2n}.\tag{2.11}$$

with \mathbf{I}_n the identity matrix of dimension n .

2.1 Canonical Transformations

Canonical transformations are special transformations from $\mathbf{q}(t)$ to new variables $\mathbf{Q}(\mathbf{q}, t)$ that act on the dynamical variables preserving the form of the Euler-Lagrange equations. The Hamiltonian formulation of the equations of motion has important advantages: we can enlarge the class of possible transformations imposing that also the Hamilton equations are preserved. Indeed, in the Hamiltonian treatment the momenta \mathbf{p} are variables independent of and on an equal footing with the coordinates \mathbf{q} . In this case, the transformation will include all the $2n$ independent variables \mathbf{p} and \mathbf{q} :

$$Q_i = Q_i(p, q, t) \quad P_i = P_i(p, q, t).$$

In order to retain the canonical form, the new variables have to satisfy the following conditions:

$$\dot{Q}_i = \frac{\partial H'}{\partial P_i} \quad \dot{P}_i = -\frac{\partial H'}{\partial Q_i},\tag{2.12}$$

with Hamiltonian $H'(\mathbf{P}, \mathbf{Q})$. If transformations respect the previous constraints, they are called *canonical transformations*.

A first way to retrieve canonical transformations is using generating functions. If the new variables \mathbf{P} and \mathbf{Q} satisfy the Hamilton equations, we can write the principle of least action as:

$$\delta \int_{t_1}^{t_2} (\dot{\mathbf{p}} d\mathbf{q} - H dt) = \delta \int_{t_1}^{t_2} (\dot{\mathbf{P}} d\mathbf{Q} - H' dt) = 0.\tag{2.13}$$

The two expressions are equivalent if their intergrands are equal apart from the total differential of a function F of coordinates, momenta and time. Each canonical transformation is characterized by a specific function F , called *generating function* of the transformation.

$$\dot{\mathbf{p}} d\mathbf{q} - H dt = \dot{\mathbf{P}} d\mathbf{Q} - H' dt + dF \quad (2.14)$$

In particular, there are four types of these functions, called mixed generating functions, that mix new and old dynamical variables, ensuring that the obtained transformation is canonical: $F_1(\mathbf{q}, \mathbf{Q}, t)$, $F_2(\mathbf{q}, \mathbf{P}, t)$, $F_3(\mathbf{Q}, \mathbf{p}, t)$ and $F_4(\mathbf{P}, \mathbf{p}, t)$. For example, assuming $F_k = F_2(\mathbf{q}, \mathbf{Q}, t)$, from equation (2.14), we can retrieve the relation between new and old variables:

$$p_i = \frac{\partial F_2}{\partial q_i}, \quad Q_i = -\frac{\partial F_2}{\partial P_i}, \quad H' = H + \frac{\partial F_2}{\partial t} \quad \forall i = 1, \dots, n.$$

2.2 Extended Phase Space

In some cases, it is easier to work with *autonomous* Hamiltonian systems. An autonomous Hamiltonian system is a system whose Hamiltonian does not explicitly depend on the independent variable. It is possible to transform non-autonomous Hamiltonian systems with n degrees of freedom into autonomous Hamiltonian system with $n + 1$ degrees of freedom. Let us consider the original independent variable t : it is possible to treat it as if it were dependent on a new independent variable τ (assuming for sake of simplicity that $t(\tau) = \tau$).

Let us now define the extended phase space of dimension $2n + 2$, where the canonical pair $(t; E)$ is added to the usual dynamical variables. Then, the new system with $n + 1$ degrees of freedom is autonomous and ruled by the following Hamiltonian:

$$\tilde{H}(\tilde{\mathbf{q}}, \tilde{\mathbf{p}}) = E + H, \quad (2.15)$$

where $\tilde{\mathbf{q}} = (\mathbf{q}^T, t)^T$ and $\tilde{\mathbf{p}} = (\mathbf{p}^T, E)^T \in \mathbb{R}^{n+1}$.

In this case, indicating with the prime the total derivative respect to τ , the Hamilton equations become:

$$\begin{aligned} \tilde{q}'_i &= \frac{\partial \tilde{H}}{\partial \tilde{p}_i} = \frac{\partial H}{\partial p_i} & \forall i = 1, \dots, n; \\ \tilde{q}'_{n+1} &= t' = 1; \\ \tilde{p}'_i &= -\frac{\partial \tilde{H}}{\partial \tilde{q}_i} = -\frac{\partial H}{\partial q_i} & \forall i = 1, \dots, n; \\ \tilde{p}'_{n+1} &= E' = -\frac{\partial \tilde{H}}{\partial t} = -\frac{\partial H}{\partial t}; \end{aligned}$$

2.3 Choice of the Independent Variable

In beam dynamics it is a common practice to express the equations of motion using the distance along a path as the independent variable. Indeed, in particle accelerator, the axial speed is almost constant and almost equal to the speed of light c . Under these conditions, it is more useful to express the equations of motion in terms of distance rather than time. Moreover, it is easier to evaluate "how far" the particle went in a beam line, rather than "when" a particle passed in a certain magnet. From this point of view, Hamiltonian mechanics provides a useful technique to perform this conversion [Wol14]. These techniques rely on the re-parametrization of the action. Following [Dra19], we have:

Theorem 2.3.1. *Suppose $H(\mathbf{q}, \mathbf{p}, t)$ is a Hamiltonian for a system having n degrees of freedom. Suppose further that $\dot{q}_K = \frac{\partial H}{\partial p_L} \neq 0$, $K \in [1, \dots, n]$, for some interval of time T in some region R of the phase space described by the $2n$ variables (q_1, \dots, q_n) and (p_1, \dots, p_n) . Then in this region and time interval, q_K can be introduced as an independent variable in place of the time t .*

Consider again the expression for the action (2.1):

$$S(\mathbf{q}, \mathbf{p}) = \int_0^T \mathcal{L}(\mathbf{q}, \dot{\mathbf{q}}, t) dt = \int_0^T \sum_{i=1}^n p_i \dot{q}_i - H(\mathbf{q}, \mathbf{p}, t) dt, \quad (2.16)$$

where n is the number of degrees of freedom (in our case $n = 3$). The dependence of \mathbf{q} and \mathbf{p} on the time t is given for granted. An infinitesimal variation of the action can be expressed as:

$$\delta S(\mathbf{q}, \mathbf{p}) = \int_0^T \sum_{i=1}^n \delta p_i \dot{q}_i + p_i \delta \dot{q}_i - \delta H(\mathbf{q}, \mathbf{p}, t) dt. \quad (2.17)$$

To have a graphical idea of what is happening, we can plot both the particle's momentum and position on a two dimensional graph (see fig. 2.1). This space is the so called *phase space*. Over the period from time 0 to time T the particle is following a particular line on this plot.

The variation at (2.17) can be seen as a change $\delta \mathbf{p}$ and $\delta \mathbf{q}$ to the dynamic variables, inducing a variation δH of the Hamiltonian. Graphically, we are fixing the starting and the ending points in the phase space, and we are considering a different path in the same interval of time.

Recalling the expression (2.8) for the infinitesimal Hamiltonian, the action's variation is:

$$\begin{aligned} \delta S(\mathbf{q}, \mathbf{p}) &= \int_0^T (\mathbf{p} \delta \dot{\mathbf{q}} + \dot{\mathbf{p}} \delta \mathbf{q}) dt = \\ &= \int_0^T \frac{d}{dt} (\mathbf{p} \delta \mathbf{q}) dt = \\ &= [\mathbf{p} \delta \mathbf{q}]_0^T. \end{aligned}$$

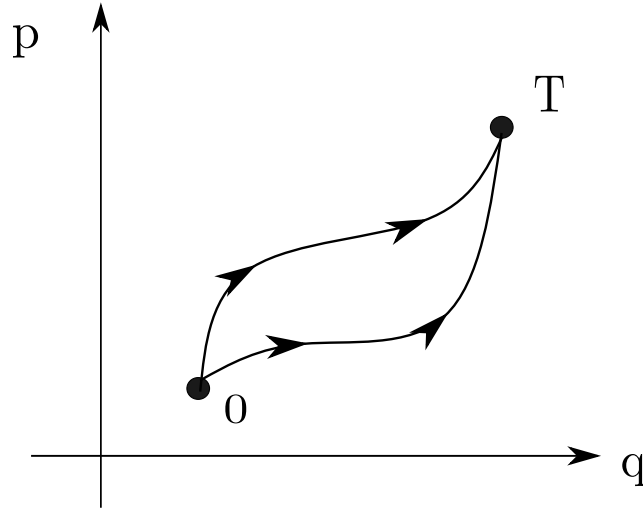


Figure 2.1: Path of the integral in phase space

Since the starting and ending points in the phase space are fixed, $\delta\mathbf{q} = 0$ at $t = 0, T$, we obtain:

$$\delta S(\mathbf{q}, \mathbf{p}) = 0.$$

This result means that, for a system obeying Hamilton equations, the path taken by the particle in the time interval $(0, T)$ is the one that minimizes the action with respect to small changes in the trajectory (the principle of least action).

Let us consider now a beam line with the accelerator components aligned along $q_3(t)$ (z axis of a Cartesian coordinate system). If one of the generalized coordinates \mathbf{q} is invertible with respect to the independent variable t and $\dot{q}_i(t) \neq 0 \forall t \in [0, T]$, then the path can be re-parametrized. Thus, we can rewrite (2.16) as an integral over one of the coordinates, for example q_3 . We have that:

$$\begin{aligned} S(\mathbf{q}, \mathbf{p}) &= \int_{q_{3,0}}^{q_{3,T}} \left(\sum_{i=1}^n p_i(t(q_3)) \frac{dq_i}{dt}(t(q_3)) - H(t(q_3)) \right) \frac{dt}{dq_3}(q_3) dq_3 = \\ &= \int_{q_{3,0}}^{q_{3,T}} \left(p_3(t(q_3)) + \sum_{i=1}^{n-1} p_i(t(q_3)) \frac{dq_i}{dq_3}(t(q_3)) - H(t(q_3)) \frac{dt}{dq_3}(q_3) \right) dq_3, \end{aligned}$$

where the particle is in $q_3 = q_{3,0}$ at time $t = 0$, and in $q_3 = q_{3,T}$ at time $t = T$.

If we replace the Hamiltonian H by $-p_3$ and the coordinate q_3 by t , we obtain a system equivalent to (2.18), where the independent variable is now q_3 , the distance along the beam line. The other coordinate and momentum pairs, (q_1, p_1) and (q_2, p_2) , are left unchanged:

$$S(\mathbf{q}, \mathbf{p}) = \int_{q_{3,0}}^{q_{3,T}} \left(\sum_{i=1}^n p_i(q_3) q'_i(q_3) + p_3(q_3) \right) dq_3. \quad (2.18)$$

This replacement is equivalent to assume $(t, -H)$ as a new canonical pair of variables. The prime now indicates the derivative with respect to the independent variable q_3 .

2.4 Symplectic Condition

The main goal of this work is to study how the numerical approximations of field maps affect the symplectic properties of a Hamiltonian system. In this section we are going to define the concept of symplecticity and all its consequences.

Transfer maps for magnetic components are fundamental to study beam dynamics in accelerators. A transfer map is simply a statement of the relationship between the dynamical variables for a particle at different points. In the case of an accelerator beam line:

$$\mathbf{w}(s_1) = \mathbf{M}_{s_0, s_1}(\mathbf{w}(s_0))$$

where $\mathbf{w} = (x, y, z, p_x, p_y, p_z) \in \mathbb{R}^{2n}$ is a vector in phase space and \mathbf{M} is the transfer map, function of the dynamical variables for a particle at $s = s_0$. The transfer map \mathbf{M} is found by solving Hamilton's equations for a particle moving from s_0 to s_1 . From [HLW06]:

Definition 2.4.1. A generic differentiable map $\mathbf{M} : U \subset \mathbb{R}^{2n} \rightarrow \mathbb{R}^{2n}$ (where U is an open set) is called *symplectic* if

$$J(\mathbf{w})^T S J(\mathbf{w}) = S \quad \forall \mathbf{w} \in U,$$

where $J(\mathbf{w})$ is the Jacobian matrix of the map \mathbf{M} and S is a block-diagonal $2n \times 2n$ antisymmetric matrix, defined as:

$$S = \begin{pmatrix} s & 0 & 0 & 0 \\ 0 & s & 0 & 0 \\ 0 & 0 & \ddots & 0 \\ 0 & 0 & 0 & s \end{pmatrix},$$

where s is the 2×2 matrix given by:

$$s = \begin{pmatrix} 0 & 1 \\ -1 & 0 \end{pmatrix}.$$

Let us consider the components w_i of the vector \mathbf{w} , where for n degrees of freedom, $i = 1, \dots, 2n$. As already said in (2.10), the Hamiltonian equations can be written as:

$$\dot{w}_i = S \frac{\partial H}{\partial w_i},$$

where \dot{w}_i is the derivative with respect to the independent variable. The matrix S has the following properties:

$$S^{-1} = -S, \quad S^2 = -I, \quad \det(S) = 1, \quad (2.19)$$

where I is the $2n \times 2n$ identity matrix.

Following the procedure explained in [Wol14], we consider an infinitesimal transformation in the independent variable from $s = s_0$ to $s = s_0 + \delta s$. In this infinitesimal interval, the dynamic variables change as:

$$w_i(s_0 + \delta s) = w_i(s_0) + \dot{w}_i(s_0)\delta s = w_i(s_0) + S_{ik} \left. \frac{\partial H}{\partial w_k} \right|_{s=s_0} \delta s,$$

where we used the Einstein notation for the repeated indices. The Jacobian matrix element of this infinitesimal transformation from s_0 to $s_0 + \delta s$ is:

$$J_{ij} = \frac{\partial w_i(s_0 + \delta s)}{\partial w_j(s_0)} = \delta_{ij} + S_{ik} \left. \frac{\partial^2 H}{\partial w_j \partial w_k} \right|_{s=s_0} \delta s,$$

where δ_{ij} is the Kronecker delta. Because of the antisymmetrical properties of S , we can write the transpose of J as:

$$J_{ij}^T = \delta_{ij} - \left. \frac{\partial^2 H}{\partial w_j \partial w_k} \right|_{s=s_0} S_{ik} \delta s.$$

Putting all the elements together we can write the expression for the Jacobian as:

$$J(\mathbf{w}) = I + S\tilde{H}\delta s,$$

$$J^T(\mathbf{w}) = I - \tilde{H}S\delta s,$$

where $\tilde{H}_{jk} = \left. \frac{\partial^2 H}{\partial w_j \partial w_k} \right|_{s=s_0}$ is a symmetric $2n \times 2n$ matrix. Keeping in mind the properties of S given in equation (2.19), it can then be proved that $(I - \tilde{H}S\delta s)S(I + S\tilde{H}\delta s) = S$, whence it follows that:

$$J^T(\mathbf{w})SJ(\mathbf{w}) = S \tag{2.20}$$

where J^T is the transpose of the Jacobian matrix J .

Symplecticity provides us with a direct test for canonical transformations. We considered the motion of a system from s_0 to $s_0 + \delta s$. In the infinitesimal interval δs , the coordinates and the momenta changed by increments $\dot{q}\delta s$ and $\dot{p}\delta s$. Thus, considering a set of new variables \mathbf{W} , the motion transformation can be written as:

$$\mathbf{W} = \mathbf{w} + S \frac{\partial H}{\partial \mathbf{w}} \delta s.$$

Repeating the steps of the previous proof, we would find that if a transformation is symplectic, it is canonical, and if a transformation is canonical, then it is symplectic [FM06]:

Definition 2.4.2. A differentiable and invertible coordinate transformation \mathbf{W} is called *canonical* if the Jacobian matrix

$$\mathbf{J}(\mathbf{w}) = \frac{\partial \mathbf{W}}{\partial \mathbf{w}}$$

is symplectic for every choice of \mathbf{w} in the domain of the transformation.

We should point out that the Jacobian matrix will generally be a function of the dynamical variables. However, if we are dealing with a linear transformation, the components of the vector \mathbf{M} are polynomials in the dynamical variables with zeroth-order and first-order terms, then the Jacobian matrix will be a matrix with constant components. The first-order part of a linear transfer map can be represented by a symplectic matrix.

2.5 Symplecticity and Liouville's Theorem

An important consequence of symplecticity is that in symplectic transformations some quantities are conserved. An example is the volume identified by a set of particles in phase space. In this section we are presenting this aspect, ending with the introduction and the proof of Liouville theorem.

Let us consider a symplectic transformation in phase space \mathbf{M} as defining a new set of dynamical variables [Wol14]:

$$\mathbf{W} = \mathbf{M}(\mathbf{w}).$$

As an example, we can imagine to pass from an initial region described by $\mathbf{w} \in \mathbb{R}^{2n}$, to a final region (described by $\mathbf{W} \in \mathbb{R}^{2n}$) by the symplectic map \mathbf{M} . A volume element in phase space in the original variables \mathbf{w} is represented as:

$$dv = \prod_{i=1}^{2n} dw_i. \quad (2.21)$$

In the new variables \mathbf{W} , the volume element is:

$$dV = \prod_{i=1}^{2n} dW_i = |\det(J)| \prod_{i=1}^{2n} dw_i, \quad (2.22)$$

where $|\det(J)|$ is the absolute value of the determinant of the Jacobian matrix of the transformation from the old to the new variables. Using the symplectic condition (2.20) we can also get:

$$\det(J^T S J) = \det(J)^2 \det(S) = \det(S) = 1.$$

It follows immediately that:

$$\det(J) = \pm 1, \quad |\det(J)| = 1. \quad (2.23)$$

Putting (2.21), (2.22) and (2.23) together we get:

$$dV = dv.$$

We can conclude that the volume of any given region in phase space is conserved under a symplectic transformation [Wol14].

In order to introduce Liouville theorem, we need to consider particles densities. We know that the density of particles in phase space is given by the number of particles in a given region divided by the volume of the region. As we have seen, in a Hamiltonian system, both the number of particles and the volume defined by them is conserved [Wol14].

Theorem 2.5.1. *In any system governed by a Hamiltonian, the density of particles in phase space must remain constant as the independent variable evolves:*

$$\frac{d\rho}{dt} = \frac{\partial \rho}{\partial t} + \sum_{i=1}^{2n} \frac{dw_i}{dt} \frac{\partial \rho}{\partial w_i} = 0,$$

where ρ is the density of particles in a given volume.

The theorem may be considered a consequence of the symplectic condition, since its proof relies on the constancy of the Jacobian determinant (which is a consequence of symplecticity). A more formal demonstration of the Liouville's theorem can be found in Appendix B.

2.6 Hamiltonian for a Charged Particle

In order to describe particles dynamics in a beam line, we define the Hamiltonian for a charged particle moving through electromagnetic fields. In the non-relativistic frame, the Hamiltonian of this system would be:

$$H(\mathbf{q}, \mathbf{p}) = \frac{1}{2m} (\mathbf{p} - Q\mathbf{A})^2,$$

where m is the mass of the particle, Q is the charge, \mathbf{p} is the canonical momenta and \mathbf{A} is the magnetic vector potential. The canonical momenta \mathbf{p} are related to the mechanical momenta by:

$$\mathbf{p} = \mathbf{p}^M + Q\mathbf{A}. \quad (2.24)$$

Since particles in high energy accelerators move typically with relativistic velocities, we are writing the total energy E and the momentum \mathbf{p} according to special relativity [Lan+82].

As a result, the Lagrangian of a single particle moving in an electromagnetic field is given by:

$$\mathcal{L} = -mc^2\sqrt{1 - \beta^2} + Q\mathbf{A} \cdot \mathbf{v},$$

where $\boldsymbol{\beta} = \mathbf{v}/c$, β is the norm of $\boldsymbol{\beta}$, v is the speed of the particle under consideration and c is the speed of light in vacuum. According to (2.4), the canonical momenta are:

$$\mathbf{p} = \frac{\partial \mathcal{L}}{\partial \mathbf{v}} = \frac{m\mathbf{v}}{\sqrt{1 - \beta^2}} = \gamma m\mathbf{v} + Q\mathbf{A}. \quad (2.25)$$

As we can see, the relation between mechanical and canonical momenta is the same, but the mechanical one is now $\gamma m\mathbf{v}$. For a particle in free space we can also show that the kinetic energy E is:

$$E = \gamma mc^2, \quad (2.26)$$

and:

$$\gamma = \frac{1}{\sqrt{1 - \beta^2}}, \quad (2.27)$$

is the Lorentz factor. From (2.27) the relationship between the kinetic energy and the canonical momentum can be retrieved:

$$E^2 = (\mathbf{p} - Q\mathbf{A}(\mathbf{q}))^2 c^2 + m^2 c^4, \quad (2.28)$$

where c is the speed of light in vacuum.

Since also in the relativistic case, the Hamiltonian is expressed as the total energy of the particle, we can write the following form:

$$H(\mathbf{q}, \mathbf{p}) = c\sqrt{(\mathbf{p} - Q\mathbf{A}(\mathbf{q}))^2 + m^2c^2} \quad (2.29)$$

As we already mentioned in section 2.3, it is usually more convenient to express the system using the longitudinal coordinate z . Rewriting the Hamiltonian in (2.29) we obtain the new form \mathcal{K} :

$$\mathcal{K} = -p_z = -\sqrt{\frac{E^2}{c^2} - (p_x - QA_x)^2 - (p_y - QA_y)^2 - m^2c^2} - QA_z, \quad (2.30)$$

where the Hamiltonian H was replaced by the total energy of the particle E . At this point, the dynamical variables are $(x, y, t, p_x, p_y, -E)$ and z is the independent variable. It can be noticed that this new Hamiltonian does not describe an autonomous system anymore, due to the fact that the magnetic vector potential depends on the independent variable z .

2.6.1 Dynamical Variables for Beam Dynamics

Once the Hamiltonian (2.30) and the electromagnetic potentials are known, it is possible to derive the equations of motion as function of the position. However, these equations are generally too complex to be solved exactly, and we need to perform some approximations.

A general procedure in beam dynamics is to consider the new position and momentum as relative quantities with respect to those of a reference particle, which is assumed to move along the z axis with a reference momentum P_0 [Wol14].

Since we are dealing with Hamiltonian systems, we also need to ensure that the new variables will be canonical variables and the transformation from the old to the new ones has to be a canonical transformation.

Describing the motion of a general particle in terms of relative position with respect to a reference particle, the new set of variable will take relatively small values, if all the particles in the beam line are assumed to have a momentum similar to P_0 . The trajectory described by the reference particle is called reference orbit and it is characterized by the following values of the dynamical variables:

$$x^0 = y^0 = p_x^0 = p_y^0 = 0, \quad t^0 = \frac{z}{v_z^0} = \frac{z}{c\beta_0}, \quad E^0 = \gamma_0 mc^2. \quad (2.31)$$

We want to perform a change of variables that allows to describe the motion of a generic particle in terms of deviations with respect of the reference orbit:

$$\mathbf{w}^d = \mathbf{w} - \mathbf{w}^0, \quad (2.32)$$

where $\mathbf{w} = (x, y, t, p_x, p_y, -E)$. This change of variables is a canonical transformation that can be obtained using a generating function (see section 2.1):

$$F_2(\mathbf{q}, \mathbf{p}^d; z) = p_i^0 q_i - q_i^0 p_i^d + q_i p_i^d,$$

which, considering (2.31), becomes:

$$F_2(\mathbf{q}, \mathbf{p}^d; z) = -E^0 t + t^0 E^d + q_i p_i^d. \quad (2.33)$$

Then, the new Hamiltonian expressed using the deviation variables is:

$$\begin{aligned}\mathcal{K}^d &= \mathcal{K} + \frac{\partial F_2}{\partial z} = \\ &= -\sqrt{\frac{(E^0 + E^d)^2}{c^2} - (p_x - QA_x)^2 - (p_y - QA_y)^2 - m^2 c^2} \\ &\quad - QA_z + \frac{E^d}{c\beta_0}\end{aligned}\quad (2.34)$$

It is also convenient to deal with non-dimensional quantities. For this reason the deviation variables have been properly scaled. This operation is done using a fixed length L and the module of reference momentum P_0 , that is defined as $P_0 = \sqrt{\left(\frac{E^0}{c}\right)^2 - m^2 c^2}$.

First of all, we apply a scaling factor to the Hamiltonian and to the independent variable:

$$\tilde{H} = \frac{\mathcal{K}^d}{P_0}, \quad \tilde{Z} = \frac{z}{L}.$$

Observing the action (2.16), we can see that:

$$\begin{aligned}S(\mathbf{q}^d, \mathbf{p}^d) &= \int_{z_0}^{z_T} \sum_{i=1}^n p_i^d \frac{q_i^d}{dz} - \mathcal{K}^d(\mathbf{q}^d, \mathbf{p}^d, z) dz \\ &= \int_{\tilde{Z}_0}^{\tilde{Z}_T} \left(\sum_{i=1}^n p_i^d \frac{q_i^d}{d\tilde{Z}} \frac{d\tilde{Z}}{dz} - \mathcal{K}^d(\mathbf{q}^d, \mathbf{p}^d, \tilde{Z}) \right) L d\tilde{Z} \\ &= \int_{\tilde{Z}_0}^{\tilde{Z}_T} \left(\sum_{i=1}^n p_i^d \frac{q_i^d}{d\tilde{Z}} - L\mathcal{K}^d(\mathbf{q}^d, \mathbf{p}^d, \tilde{Z}) \right) d\tilde{Z},\end{aligned}\quad (2.35)$$

and so the scaling of the independent variable introduces a scaling factor L in the Hamiltonian \mathcal{K}^d . The new scaled dynamic variables are then:

$$\begin{aligned}\tilde{p}_x &= \frac{p_x}{P_0}, & \tilde{p}_y &= \frac{p_y}{P_0}, & \tilde{E} &= \frac{E^d}{cP_0}, \\ \tilde{X} &= \frac{x^d}{L}, & \tilde{Y} &= \frac{y^d}{L}, & \tilde{t} &= c\frac{t^d}{L}.\end{aligned}$$

\tilde{E} can be seen as the relative energy deviation from the reference energy. We also introduced the so called mechanical momentum deviation, defined as:

$$\delta = \frac{|\mathbf{p}^d|}{P_0} = \frac{|\mathbf{p}| - P_0}{P_0} = \frac{|\mathbf{p}|}{P_0} - 1. \quad (2.36)$$

Between \tilde{E} and δ the following relations hold:

$$\tilde{E} = -\frac{\sqrt{1 + (2\delta + \delta^2)\beta_0^2} - 1}{\beta_0}, \quad \delta = \sqrt{1 - \frac{2\tilde{E}}{\beta_0} + \tilde{E}^2} - 1 \quad (2.37)$$

For simplicity, we also define the scaled version of the vector potential:

$$\mathbf{a} = \frac{Q}{P_0} \mathbf{A}. \quad (2.38)$$

Performing all the substitutions, we can write the Hamiltonian for a particle moving along z in a linear beam line as:

$$\begin{aligned}\tilde{H} &= \frac{\mathcal{K}^d}{P_0} \\ &= -\sqrt{\frac{(E^0 + E^d)^2}{c^2 P_0^2} - \left(\frac{p_x - QA_x}{P_0}\right)^2 - \left(\frac{p_y - QA_y}{P_0}\right)^2} - \frac{m^2 c^2}{P_0^2} - \frac{QA_z}{P_0} + \frac{E^d}{P_0 c \beta_0} \\ &= -\sqrt{1 - \frac{2\tilde{E}}{\beta_0} + \tilde{E}^2 - (\tilde{p}_x - a_x)^2 - (\tilde{p}_y - a_y)^2} - a_z + \frac{\tilde{E}^d}{\beta_0},\end{aligned}$$

where the canonical variables are $(\tilde{X}, \tilde{Y}, \tilde{t}, \tilde{p}_x, \tilde{p}_y, -\tilde{E})$ and the independent variable is \tilde{Z} . Finally, it is possible to rewrite the Hamiltonian, substituting the canonical pair $(\tilde{t}, -\tilde{E})$ with (l, δ) , applying again the generating function (2.14):

$$\tilde{H}_1 = -\sqrt{(1 + \delta)^2 - (\tilde{p}_x - a_x)^2 - (\tilde{p}_y - a_y)^2} - a_z - \delta, \quad (2.39)$$

where the canonical variables are now $(\tilde{X}, \tilde{Y}, l, \tilde{p}_x, \tilde{p}_y, \delta)$ and the independent variable is still \tilde{Z} .

2.6.2 Paraxial Approximation

Linear approximations to non-linear dynamical systems are usually useful in the study of accelerator components. In order to do that, the Hamiltonian is expanded as a power series to second order in the dynamical variables. The truncation of the power expansion at the lower order of \mathbf{p} is known as *paraxial approximation*. This approximation holds when the momenta in the transversal plane are much smaller than the total momentum module (i.e. $(\delta + 1)^2 \ll (\tilde{p}_x - a_x)^2 + (\tilde{p}_y - a_y)^2$). Given (2.39), we can write the Hamiltonian as the Taylor expansion to second order of \tilde{H}_1 :

$$\begin{aligned}\tilde{H}_1 &= -\sqrt{(1 + \delta)^2 - (\tilde{p}_x - a_x)^2 - (\tilde{p}_y - a_y)^2} - a_z - \delta \\ &= -(1 + \delta) \sqrt{1 - \frac{(\tilde{p}_x - a_x)^2}{(1 + \delta)^2} - \frac{(\tilde{p}_y - a_y)^2}{(1 + \delta)^2}} - a_z - \delta \\ &\approx -(1 + \delta) \left(1 - \frac{(\tilde{p}_x - a_x)^2}{2(1 + \delta)^2} - \frac{(\tilde{p}_y - a_y)^2}{2(1 + \delta)^2} \right) - a_z - \delta \\ &= -1 - 2\delta + \left(1 - \frac{(\tilde{p}_x - a_x)^2}{2(1 + \delta)} - \frac{(\tilde{p}_y - a_y)^2}{2(1 + \delta)} \right) - a_z \\ &\approx -2\delta + \left(1 - \frac{(\tilde{p}_x - a_x)^2}{2(1 + \delta)} - \frac{(\tilde{p}_y - a_y)^2}{2(1 + \delta)} \right) - a_z,\end{aligned}$$

where we neglected the constant terms, because they are not physically relevant. Since the vector potential depends on the independent variable \tilde{Z} , this Hamiltonian describes a 6D non-autonomous system. Applying the procedure explained in

section 2.2, we introduce a new canonical pair (\tilde{Z}, \tilde{p}_z) and a new independent variable σ . The new autonomous Hamiltonian \mathcal{H} is:

$$\mathcal{H} = -2\delta + \left(1 - \frac{(\tilde{p}_x - a_x)^2}{2(1 + \delta)} - \frac{(\tilde{p}_y - a_y)^2}{2(1 + \delta)} \right) - a_z + \tilde{p}_z, \quad (2.40)$$

where $\mathbf{q} = (\tilde{X}, \tilde{Y}, l, \tilde{Z})$ and $\mathbf{p} = (\tilde{p}_x, \tilde{p}_y, \delta, \tilde{p}_z)$. In this case, the equations of motion can be written as:

$$\mathbf{w} = \mathbf{J} \nabla \mathcal{H} = \begin{bmatrix} \frac{\tilde{p}_x - a_x}{\delta + 1} \\ \frac{\tilde{p}_y - a_y}{\delta + 1} \\ -\frac{(\tilde{p}_x - a_x)^2}{2(\delta + 1)^2} - \frac{(\tilde{p}_y - a_y)^2}{2(\delta + 1)^2} - 2 \\ 1 \\ \frac{\partial a_x}{\partial \tilde{X}} \frac{\tilde{p}_x - a_x}{\delta + 1} + \frac{\partial a_y}{\partial \tilde{X}} \frac{\tilde{p}_y - a_y}{\delta + 1} + \frac{\partial a_z}{\partial \tilde{X}} \\ \frac{\partial a_x}{\partial \tilde{Y}} \frac{\tilde{p}_x - a_x}{\delta + 1} + \frac{\partial a_y}{\partial \tilde{Y}} \frac{\tilde{p}_y - a_y}{\delta + 1} + \frac{\partial a_z}{\partial \tilde{Y}} a_z Y \\ 0 \\ \frac{\partial a_x}{\partial \tilde{Z}} \frac{\tilde{p}_x - a_x}{\delta + 1} + \frac{\partial a_y}{\partial \tilde{Z}} \frac{\tilde{p}_y - a_y}{\delta + 1} + \frac{\partial a_z}{\partial \tilde{Z}} \end{bmatrix}. \quad (2.41)$$

Moreover, it can be noticed that the Hamiltonian does not depend on l , so that the partial derivative of \mathcal{H} with respect to l is zero. As a consequence, δ is a constant of motion, equal to the initial value, denoted by δ_0 . If the evolution of the variable l is not needed, the canonical pair (l, δ) can be neglected, considering δ_0 as a parameter and reducing again the size of the phase space. In this case, the Hamiltonian is still given by (2.40) but, since the dynamical variables are now $\mathbf{w} = (\tilde{X}, \tilde{Y}, \tilde{Z}, \tilde{p}_x, \tilde{p}_y, \tilde{p}_z)$, the Hamilton equations become:

$$\mathbf{w} = \mathbf{J} \nabla \mathcal{H} = \begin{bmatrix} \frac{\tilde{p}_x - a_x}{\delta_0 + 1} \\ \frac{\tilde{p}_y - a_y}{\delta_0 + 1} \\ 1 \\ \frac{\partial a_x}{\partial \tilde{X}} \frac{\tilde{p}_x - a_x}{\delta_0 + 1} + \frac{\partial a_y}{\partial \tilde{X}} \frac{\tilde{p}_y - a_y}{\delta_0 + 1} + \frac{\partial a_z}{\partial \tilde{X}} \\ \frac{\partial a_x}{\partial \tilde{Y}} \frac{\tilde{p}_x - a_x}{\delta_0 + 1} + \frac{\partial a_y}{\partial \tilde{Y}} \frac{\tilde{p}_y - a_y}{\delta_0 + 1} + \frac{\partial a_z}{\partial \tilde{Y}} \\ \frac{\partial a_x}{\partial \tilde{Z}} \frac{\tilde{p}_x - a_x}{\delta_0 + 1} + \frac{\partial a_y}{\partial \tilde{Z}} \frac{\tilde{p}_y - a_y}{\delta_0 + 1} + \frac{\partial a_z}{\partial \tilde{Z}} \end{bmatrix}. \quad (2.42)$$

A further simplification can be achieved noticing that \tilde{p}_z is decoupled from the other dynamical variables, so that its computation can be neglected if we are only interested in the dynamics of the transverse variables, reducing the number of equations (2.42) to the four ones associated to \tilde{X} , \tilde{Y} , \tilde{p}_x and \tilde{p}_y .

This form of the Hamilton equations was used in some numerical tests performed at Politecnico di Milano, in the framework of the integrators analysis. For the tests performed at CERN, the equations of motion used are the one presented in section 2.7.

2.7 Alternative Form of the Equations of Motion

In alternative to the Hamiltonian form (2.42), the equations of motion can also be rewritten in a form more similar to that often employed in the non relativistic case.

Indeed, in the tracking tests performed at CERN with the "RF-Track" code, the equations of motion (with z as independent variable) were written as:

$$\frac{d\mathbf{p}^M}{dz} = \frac{Q}{\beta_z c} (\mathbf{v} \times \mathbf{B}), \quad (2.43)$$

$$\begin{aligned} \frac{dx}{dz} &= \frac{p_x^M}{p_z^M}, \\ \frac{dy}{dz} &= \frac{p_y^M}{p_z^M}, \\ \frac{dt}{dz} &= \frac{1}{\beta_z c}, \end{aligned} \quad (2.44)$$

where \mathbf{p}^M is the mechanical momentum and $\beta_z = v_z/c$, with v_z velocity in the z direction. In the first equation it is possible to recognize the expression of the Lorentz force.

This form of the equations was implemented in order integrate directly the magnetic field \mathbf{B} values, instead of those of the vector potential. However, this version was used just for testing non-symplectic integrators.

2.8 The Helmholtz Theorem

We are now introducing an important theorem that will be widely used in the next sections for the reconstruction of the field data. From [Dra19], the Helmholtz decomposition theorem reads:

Theorem 2.8.1. *Suppose V is simply connected volume in 3-dimensional space bounded by a surface S and let $\mathbf{F}(\mathbf{r})$ be a continuous vector field with continuous*

first partial derivatives in V . Then $\mathbf{F}(\mathbf{r})$ can be uniquely expressed in terms of the negative gradient of a scalar potential $I_S(\mathbf{r})$ and the curl of a vector potential $\mathbf{I}_V(\mathbf{r})$:

$$\mathbf{F}(\mathbf{r}) = \nabla \times \mathbf{I}_V(\mathbf{r}) - \nabla I_S(\mathbf{r}) \quad \text{for } \mathbf{r} \in V.$$

The Helmholtz theorem can be demonstrated in the following way. Let us consider the three dimensional representation of the delta function:

$$\nabla^2 \left(\frac{1}{|\mathbf{r} - \mathbf{r}'|} \right) = 4\pi\delta(\mathbf{r} - \mathbf{r}'). \quad (2.45)$$

Next, we write the arbitrary function $\mathbf{F}(\mathbf{r})$ over a given volume V as:

$$\mathbf{F}(\mathbf{r}) = \int_V d^3r' \delta(\mathbf{r} - \mathbf{r}') \mathbf{F}(\mathbf{r}'). \quad (2.46)$$

Substituting (2.45) in (2.46) and factoring the derivatives with respect to the function point \mathbf{r}' yields:

$$\mathbf{F}(\mathbf{r}) = \frac{-\nabla^2}{4\pi} \int_V d^3r' \delta(\mathbf{r} - \mathbf{r}') \frac{\mathbf{F}(\mathbf{r}')}{|\mathbf{r} - \mathbf{r}'|}. \quad (2.47)$$

We now apply the vector identity:

$$\nabla^2 = \nabla(\nabla \cdot) - \nabla \times (\nabla \times).$$

In this way, we can rewrite (2.47) as:

$$\mathbf{F}(\mathbf{r}) = \nabla \times \mathbf{I}_V - \nabla I_S, \quad (2.48)$$

where

$$\begin{aligned} \mathbf{I}_V &= \frac{1}{4\pi} \nabla \times \int_V d^3r' \frac{\mathbf{F}(\mathbf{r}')}{|\mathbf{r} - \mathbf{r}'|}, \\ I_S &= \frac{1}{4\pi} \nabla \cdot \int_V d^3r' \frac{\mathbf{F}(\mathbf{r}')}{|\mathbf{r} - \mathbf{r}'|}. \end{aligned} \quad (2.49)$$

At this point, we have to bring the derivative operator with respect to \mathbf{r} inside the integral. Then, it is possible to switch the derivative from \mathbf{r} to \mathbf{r}' with a cost of a minus sign. Finally, integrating by parts, the resulting equations we end up with are:

$$\begin{aligned} \mathbf{I}_V &= \frac{1}{4\pi} \int_V \frac{\nabla' \times \mathbf{F}(\mathbf{r}')}{|\mathbf{r} - \mathbf{r}'|} dr^3 - \frac{1}{4\pi} \int_S \frac{\mathbf{n}(\mathbf{r}') \times \mathbf{F}(\mathbf{r}')}{|\mathbf{r} - \mathbf{r}'|} dS', \\ I_S &= \frac{1}{4\pi} \int_V \frac{\nabla' \cdot \mathbf{F}(\mathbf{r}')}{|\mathbf{r} - \mathbf{r}'|} dr^3 - \frac{1}{4\pi} \int_S \frac{\mathbf{n}(\mathbf{r}') \cdot \mathbf{F}(\mathbf{r}')}{|\mathbf{r} - \mathbf{r}'|} dS', \end{aligned} \quad (2.50)$$

where $S = \partial V$ is the boundary surface of the volume and \mathbf{n} is the corresponding outwards normal.

Given a magnetic field $\mathbf{B}(\mathbf{r})$ under the conditions in Theorem 2.8.1, we can easily find:

$$\mathbf{B}(\mathbf{r}) = \nabla \times \mathbf{A}(\mathbf{r}) - \nabla\varphi(\mathbf{r}) \quad \text{for } \mathbf{r} \in V, \quad (2.51)$$

where:

$$\mathbf{A}(\mathbf{r}) = \frac{1}{4\pi} \int_V \frac{\nabla' \times \mathbf{B}(\mathbf{r}')}{|\mathbf{r} - \mathbf{r}'|} dV' - \frac{1}{4\pi} \int_S \frac{\mathbf{n}(\mathbf{r}') \times \mathbf{B}(\mathbf{r}')}{|\mathbf{r} - \mathbf{r}'|} dS', \quad (2.52)$$

$$\varphi(\mathbf{r}) = \frac{1}{4\pi} \int_V \frac{\nabla' \cdot \mathbf{B}(\mathbf{r}')}{|\mathbf{r} - \mathbf{r}'|} dV' - \frac{1}{4\pi} \int_S \frac{\mathbf{n}(\mathbf{r}') \cdot \mathbf{B}(\mathbf{r}')}{|\mathbf{r} - \mathbf{r}'|} dS'. \quad (2.53)$$

Since in a magnetostatic case, Maxwell equations describing the system are those of (1.2), we can retrieve the widely known Biot-Savart law:

$$\mathbf{B} = \nabla \times \mathbf{A} = \frac{\mu_0}{4\pi} \int_V \frac{\mathbf{J}(\mathbf{r}') \times (\mathbf{r} - \mathbf{r}')}{|\mathbf{r} - \mathbf{r}'|^3} dr'^3. \quad (2.54)$$

This is the case of solenoidal fields, in which the magnetic scalar potential contribution is equal to zero. This is also the case for our system of coils.

It has to be pointed out that, given a magnetic field in the form (2.54), sampled on a discrete grid, it is not always true that a field reconstructed by interpolation from this sampled data will preserve all the properties of the original field. In particular, the reconstructed field may not be divergence free. In other words, in the interpolated reconstruction a small contribution given by a spurious scalar potential field φ can arise.

Chapter 3

Numerical Methods

In this chapter, we present several numerical techniques which are employed to achieve an accurate approximation of the solutions of the equations for our system. In the first part, the vector potential reconstruction and post-processing methods developed at CERN are introduced. A brief description of the numerical methods for integration is then presented. Afterwards, an overview on the interpolation methods applied in both the parts of this work is presented. Along some classical interpolation algorithms, an original method is also introduced. The Ordinary Differential Equation (ODE) methods tested and implemented, together with the error norms used in the validation chapters are explained in the last sections.

3.1 Vector Potential Post-Processing Methods

The methods presented in this section have been developed and implemented during the work done at CERN. As we already mentioned, in accelerator particle physics it is usual to deal with measured field maps, so that a magnetic field \mathbf{B} is only available at the points of a specific grid. Usually, given these data, the field itself is directly interpolated and its vector potential is used in the integration. In particular, the Hamiltonian (2.29) (function of the vector potential) is integrated to retrieve the equations of motion. However, this measured field is usually not divergence free, due to measurements errors, and consequently its vector potential is not enough to describe the field completely.

In order to solve this problem, our procedure includes also a reconstruction and post-processing step: after retrieving the vector potential from the measured field map, this is then re-elaborated, in order to make it consistent with a divergence free magnetic field, preserving the original behavior of the data as much as possible. For this purpose, we have tested two different techniques. The first one is based on the paper [MMK06]. The second method is based instead on some results presented in [Dra19]. This post-processing method allows to eliminate the spurious scalar potential contribution completely, leading to a perfectly divergence free magnetic field.

In the following pages, we are going to describe in the detail the two reconstruction and post-processing methods. The re-elaborated vector potential obtained with the two methods was then interpolated with the cubic interpolation presented in section 3.3.2.

3.1.1 First Post-Processing Method

The first method we implemented is based on the procedure presented in [MMK06]. In order to ensure $\nabla \cdot \mathbf{B} = 0$, a common strategy is to work with the vector potential \mathbf{A} and employ an interpolation procedure that guarantees a \mathcal{C}^2 regularity. Assuming the Coulomb Gauge to hold ($\nabla \cdot \mathbf{A} = 0$), the relationship between \mathbf{A} and \mathbf{B} is:

$$\mathbf{B} = \nabla \times \mathbf{A}.$$

Starting from the knowledge of the magnetic field at the discrete points of a grid, the Fourier transform of the vector potential can be written as:

$$\tilde{\mathbf{A}}(\mathbf{k}) = \frac{i\mathbf{k} \times \tilde{\mathbf{B}}(\mathbf{k})}{|k|^2}, \quad (3.1)$$

where $\tilde{\mathbf{B}}(\mathbf{k})$ is the Fourier transform of the field and \mathbf{k} is the wave vector number. In order to take advantage of the numerical efficiency of fast Fourier transforms, in the implementation the fields and their transforms are considered on a uniform Cartesian grid, and the number of grid points in each the x , y and z directions is an integer power of two. Once $\tilde{\mathbf{A}}$ is computed, it is straightforward to find \mathbf{A} as inverse Fourier transform. It has to be noticed that the expression for $\tilde{\mathbf{A}}$ has a singularity in correspondence of $\mathbf{k} = \mathbf{0}$. This value represents the contribution to the vector potential due to the average value of the magnetic field. It is computed and analytically added to the total vector potential as:

$$\mathbf{A}_0 = -\frac{\mathbf{r} \times \mathbf{B}_0}{2}.$$

The same technique can also be applied to identify the presence of a magnetic scalar potential contribution in the original data:

$$\tilde{\varphi} = \frac{i\mathbf{k} \cdot \tilde{\mathbf{B}}(\mathbf{k})}{|k|^2}. \quad (3.2)$$

It has to be noticed that, even if the method is aiming to the reconstruction of a divergence-free field, a substantial contribution given by the magnetic scalar potential was detected in different cases. In realistic situations, in which the field map is measured, this may be due to measurement errors and non-linearities. As a consequence, the magnetic field cannot be completely described by the vector potential contribution, and we will have to keep in mind that the resulting post-processed field will not be perfectly divergence-free.

Finally, the field is computed interpolating the values of \mathbf{A} and φ defined in each grid point and computing $\mathbf{B} = \nabla \cdot \mathbf{A} - \nabla \varphi$. According to [MMK06], \mathbf{A} and φ have to be \mathcal{C}^2 continuous, so that the equality (vector potential case):

$$\frac{\partial^2 A_i}{\partial x_j \partial x_k} = \frac{\partial^2 A_i}{\partial x_k \partial x_j},$$

holds. For this reason, the interpolation defined in section 3.3.2 was employed in this post-processing method. In the following chapters, we are going to refer to this method with the name FIRST.

It is important to know that the presence of the scalar magnetic field contribution represents an error in the desired reconstructed divergence-free magnetic field. For this reason, we implemented a second post-processing method, focusing on the direct elimination of this contribution.

3.1.2 Second Post-Processing Method

An alternative post-processing approach is now introduced, which is based on the *Helmholtz decomposition* theorem. This presentation follows the steps explained in [Dra19]. Recalling the equation in Theorem 2.8.1, we can rewrite it introducing the superscripts n and t to denote the normal and tangential components:

$$\mathbf{B}(\mathbf{r}) = \nabla \times \mathbf{A}_t(\mathbf{r}) - \nabla \varphi_n(\mathbf{r}) \quad \text{for } \mathbf{r} \in V.$$

\mathbf{A}_t and φ_n are defined by the integrals already introduced in (2.52) and (2.53):

$$\mathbf{A}_t(\mathbf{r}) = \frac{1}{4\pi} \int_V \frac{\nabla' \times \mathbf{B}(\mathbf{r}')}{|\mathbf{r} - \mathbf{r}'|} dV' - \frac{1}{4\pi} \int_S \frac{\mathbf{n}(\mathbf{r}') \times \mathbf{B}(\mathbf{r}')}{|\mathbf{r} - \mathbf{r}'|} dS', \quad (3.3)$$

$$\varphi_n(\mathbf{r}) = \frac{1}{4\pi} \int_V \frac{\nabla' \cdot \mathbf{B}(\mathbf{r}')}{|\mathbf{r} - \mathbf{r}'|} dV' - \frac{1}{4\pi} \int_S \frac{\mathbf{n}(\mathbf{r}') \cdot \mathbf{B}(\mathbf{r}')}{|\mathbf{r} - \mathbf{r}'|} dS'. \quad (3.4)$$

As we can see, the vector potential depends only on the tangential component of the field, whereas the scalar one depends only on the normal component. Here, $\mathbf{n}(\mathbf{r}')$ is the outward normal to S at the point \mathbf{r}' , position of the source. The *Green's functions* for the Laplace's equations (in three dimensions) are defined as [Dra19]:

$$G(\mathbf{r}, \mathbf{r}') = -\frac{1}{4\pi} \frac{1}{|\mathbf{r} - \mathbf{r}'|}. \quad (3.5)$$

We can now write the expressions as:

$$\mathbf{A}_t(\mathbf{r}) = - \int_V \nabla' \times \mathbf{B}(\mathbf{r}') G(\mathbf{r}, \mathbf{r}') dV' + \int_S \mathbf{n}(\mathbf{r}') \times \mathbf{B}(\mathbf{r}') G(\mathbf{r}, \mathbf{r}') dS' \quad (3.6)$$

$$\varphi_n(\mathbf{r}) = - \int_V \nabla' \cdot \mathbf{B}(\mathbf{r}') G(\mathbf{r}, \mathbf{r}') dV' + \int_S \mathbf{n}(\mathbf{r}') \cdot \mathbf{B}(\mathbf{r}') G(\mathbf{r}, \mathbf{r}') dS' \quad (3.7)$$

Let us consider the case of main interest for our purposes. If $\mathbf{B}(\mathbf{r})$ is divergence and curl free in V , only the surface terms appear in (3.3) and (3.4) and we obtain:

$$\mathbf{A}_t(\mathbf{r}) = -\frac{1}{4\pi} \int_S \frac{\mathbf{n}(\mathbf{r}') \times \mathbf{B}(\mathbf{r}')}{|\mathbf{r} - \mathbf{r}'|} dS' = \int_S \mathbf{n}(\mathbf{r}') \times \mathbf{B}(\mathbf{r}') G(\mathbf{r}, \mathbf{r}') dS', \quad (3.8)$$

$$\varphi_n(\mathbf{r}) = -\frac{1}{4\pi} \int_S \frac{\mathbf{n}(\mathbf{r}') \cdot \mathbf{B}(\mathbf{r}')}{|\mathbf{r} - \mathbf{r}'|} dS' = \int_S \mathbf{n}(\mathbf{r}') \cdot \mathbf{B}(\mathbf{r}') G(\mathbf{r}, \mathbf{r}') dS'. \quad (3.9)$$

However, this formalism presents an issue: in order to employ a Hamiltonian formulation to reap the benefits of symplectic symmetry, we need the field to be expressed as curl of the vector potential only (rather than in terms of both a scalar and vector potential):

$$\mathbf{B}(\mathbf{r}) = \nabla \times \mathbf{A}(\mathbf{r}).$$

In order to get rid of the magnetic scalar potential contribution, we need a vector potential such that:

$$\nabla \times \mathbf{A}_n(\mathbf{r}) = -\nabla \varphi_n(\mathbf{r}).$$

Then, the overall vector potential will be:

$$\mathbf{A}(\mathbf{r}) = \mathbf{A}_t(\mathbf{r}) + \mathbf{A}_n(\mathbf{r}).$$

A suitable expression for $\mathbf{A}_n(\mathbf{r})$ can be found using the so called *Dirac monopole vector potential*. Indeed, the expression of $\varphi_n(\mathbf{r})$ as given by (3.9) appears to arise from a distribution of magnetic monopoles described by a magnetic charge surface density spread over the surface S . Therefore, it should be possible to find an equivalent vector potential based on the vector potential for a magnetic monopole. Recalling the Green's function given in equation (3.5), we note that $G(\mathbf{r}, \mathbf{r}')$ has the following properties:

$$\nabla G(\mathbf{r}, \mathbf{r}') = -\nabla' G(\mathbf{r}, \mathbf{r}') = -\frac{1}{4\pi} \frac{\mathbf{r} - \mathbf{r}'}{|\mathbf{r} - \mathbf{r}'|^3},$$

$$\nabla^2 G(\mathbf{r}, \mathbf{r}') = (\nabla')^2 G(\mathbf{r}, \mathbf{r}') = \delta(\mathbf{r} - \mathbf{r}'),$$

where \mathbf{r} is the position of the system and \mathbf{r}' is the source position. We then define the kernel $\mathbf{G}_n(\mathbf{r}; \mathbf{r}', \mathbf{n})$ as:

$$\mathbf{G}_n(\mathbf{r}; \mathbf{r}', \mathbf{n}) = \frac{1}{4\pi} \frac{\mathbf{n} \times (\mathbf{r} - \mathbf{r}')}{|\mathbf{r} - \mathbf{r}'| - \mathbf{n} \cdot (\mathbf{r} - \mathbf{r}')} \frac{1}{|\mathbf{r} - \mathbf{r}'|^3}, \quad (3.10)$$

where \mathbf{n} is a unit vector normal and outgoing from the surface S . It can be shown that for the vector field \mathbf{G}_n , the following property holds:

$$\frac{1}{4\pi} \nabla' \frac{1}{|\mathbf{r} - \mathbf{r}'|} = \nabla' G(\mathbf{r}, \mathbf{r}') = \nabla' \times \mathbf{G}_n(\mathbf{r}; \mathbf{r}', \mathbf{n}).$$

If we define:

$$\mathbf{B}_n(\mathbf{r}) = -\nabla \varphi_n(\mathbf{r}) = \nabla \times \mathbf{A}_n(\mathbf{r}),$$

we can combine it with (3.9) in:

$$\begin{aligned}
\mathbf{B}_n(\mathbf{r}) &= \int_S \mathbf{n}(\mathbf{r}') \cdot \mathbf{B}(\mathbf{r}') \nabla' G(\mathbf{r}, \mathbf{r}') dS' \\
&= \int_S \mathbf{n}(\mathbf{r}') \cdot \mathbf{B}(\mathbf{r}') \nabla' \times \mathbf{G}_n(\mathbf{r}; \mathbf{r}', \mathbf{n}(\mathbf{r}')) dS' \\
&= \nabla' \times \int_S \mathbf{n}(\mathbf{r}') \cdot \mathbf{B}(\mathbf{r}') \mathbf{G}_n(\mathbf{r}; \mathbf{r}', \mathbf{n}(\mathbf{r}')) dS'. \tag{3.11}
\end{aligned}$$

Finally, we get the complete expression for \mathbf{A}_n :

$$\mathbf{A}_n(\mathbf{r}) = \int_S \mathbf{n}(\mathbf{r}') \cdot \mathbf{B}(\mathbf{r}') \mathbf{G}_n(\mathbf{r}; \mathbf{r}', \mathbf{n}(\mathbf{r}')) dS'. \tag{3.12}$$

Let us make at this point some observations. If $\mathbf{r} \in V$, $\mathbf{G}_n(\mathbf{r}, \mathbf{r}')$ has to respect the following properties:

$$\begin{aligned}
\nabla \cdot \mathbf{G}_n(\mathbf{r}, \mathbf{r}') &= 0, \\
\nabla \times [\nabla \times \mathbf{G}_n(\mathbf{r}, \mathbf{r}')] &= 0.
\end{aligned}$$

It is then straightforward that:

$$\begin{aligned}
\nabla \cdot \mathbf{A}_n(\mathbf{r}) &= 0, \\
\nabla \times [\nabla \times \mathbf{A}_n(\mathbf{r})] &= 0. \tag{3.13}
\end{aligned}$$

This fact has an important consequence. As long as $\mathbf{n}(\mathbf{r}')$ is the unit vector pointing outward from S , the functions $\mathbf{G}_n(\mathbf{r}, \mathbf{r}')$, for every $\mathbf{r}' \in S$, are *analytic* in \mathbf{r} for all $\mathbf{r} \in V$. It follows from (3.12), under mild conditions on $\mathbf{B}_n(\mathbf{r}')$ for $\mathbf{r}' \in S$, that $\mathbf{A}_n(\mathbf{r})$ is analytic in V . For this reason, even if $\mathbf{B}_n(\mathbf{r})$ will be known only approximately, with an accuracy depending on the method used to approximate the integral (3.11), the resulting $\mathbf{A}_n(\mathbf{r})$ will be analytic in V and will satisfy the relations (3.13) exactly, independently of any error on $\mathbf{B}_n(\mathbf{r})$, as long as the kernel is computed very accurately.

We now retrieve the expression for $\mathbf{A}_t(\mathbf{r})$. Looking at the expression (3.3), it can be proved that:

$$\begin{aligned}
\nabla \cdot \mathbf{A}_t(\mathbf{r}) &\neq 0, \\
\nabla \times [\nabla \times \mathbf{A}_t(\mathbf{r})] &\neq 0.
\end{aligned}$$

However, it is possible to recast the expression for $\mathbf{A}_t(\mathbf{r})$ in such a way to respect these properties and be symmetric with $\mathbf{A}_n(\mathbf{r})$.

Since, by assumption, $\mathbf{B}(\mathbf{r}')$ is curl free for $\mathbf{r}' \in V$, there exists a magnetic scalar potential $\psi(\mathbf{r}')$ such that

$$\mathbf{B}(\mathbf{r}') = \nabla' \psi(\mathbf{r}').$$

We can then write (3.3) as:

$$\mathbf{A}_t(\mathbf{r}) = \int_S [\mathbf{n}(\mathbf{r}') \times \nabla' \psi(\mathbf{r}')] G(\mathbf{r}, \mathbf{r}') dS'.$$

Given the identity:

$$[\nabla' \psi(\mathbf{r}')] G(\mathbf{r}, \mathbf{r}') = \nabla' [\psi(\mathbf{r}') G(\mathbf{r}, \mathbf{r}')] - \psi(\mathbf{r}') \nabla' G(\mathbf{r}, \mathbf{r}'),$$

we have that:

$$\begin{aligned} \mathbf{A}_t(\mathbf{r}) &= \int_S \mathbf{n}(\mathbf{r}') \times \nabla' [\psi(\mathbf{r}') G(\mathbf{r}, \mathbf{r}')] dS' - \int_S \mathbf{n}(\mathbf{r}') \times \psi(\mathbf{r}') \nabla' G(\mathbf{r}, \mathbf{r}') dS' \\ &= - \int_S \mathbf{n}(\mathbf{r}') \times \psi(\mathbf{r}') \nabla' G(\mathbf{r}, \mathbf{r}') dS' \\ &= - \int_S \psi(\mathbf{r}') [\mathbf{n}(\mathbf{r}') \times \nabla' G(\mathbf{r}, \mathbf{r}')] dS', \end{aligned}$$

where it can be shown that the first integral vanishes, and in the last expression we moved $\psi(\mathbf{r}')$ outside the cross product. We then define the new kernel $\mathbf{G}_t(\mathbf{r}; \mathbf{r}', \mathbf{n})$ as:

$$\mathbf{G}_t(\mathbf{r}; \mathbf{r}', \mathbf{n}) = \mathbf{n} \times \nabla' G(\mathbf{r}, \mathbf{r}') = \mathbf{n} \times (\nabla' \times \mathbf{G}_n(\mathbf{r}; \mathbf{r}', \mathbf{n})).$$

At this point, $\mathbf{A}_t(\mathbf{r})$ takes the final form:

$$\mathbf{A}_t(\mathbf{r}) = - \int_S \psi_n(\mathbf{r}') \mathbf{G}_t(\mathbf{r}; \mathbf{r}', \mathbf{n}(\mathbf{r}')) dS'. \quad (3.14)$$

Since, according to our hypothesis, the magnetic field $\mathbf{B}(\mathbf{r})$ is curl free, we can write the previous equation in function of the magnetic scalar potential φ_n . In this way:

$$\mathbf{A}_t(\mathbf{r}) = \int_S \varphi_n(\mathbf{r}') \mathbf{G}_t(\mathbf{r}; \mathbf{r}', \mathbf{n}(\mathbf{r}')) dS'. \quad (3.15)$$

Analogously to the previous case, it can be proved that also $\mathbf{G}_t(\mathbf{r})$ is respecting the properties:

$$\begin{aligned} \nabla \cdot \mathbf{G}_t(\mathbf{r}, \mathbf{r}') &= 0, \\ \nabla \times [\nabla \times \mathbf{G}_t(\mathbf{r}, \mathbf{r}')] &= 0. \end{aligned} \quad (3.16)$$

and so does $\mathbf{A}_t(\mathbf{r})$. Moreover, following the same reasoning done for $\mathbf{G}_n(\mathbf{r}, \mathbf{r}')$, $\mathbf{A}_t(\mathbf{r})$ is again analytic in V and equations (3.16) hold exactly even in the presence of errors in the surface values $\varphi_n(\mathbf{r}')$, no matter how poorly the integrals (3.14) are evaluated.

Finally, the three equations implemented are given by (3.17).

$$\begin{aligned} \mathbf{A}_n(\mathbf{r}) &= \int_{S'} \mathbf{n}(\mathbf{r}') \cdot \mathbf{B}(\mathbf{r}') \mathbf{G}_n(\mathbf{r}; \mathbf{r}', \mathbf{n}(\mathbf{r}')) dS', \\ \varphi_n(\mathbf{r}) &= \int_{S'} \mathbf{n}(\mathbf{r}') \cdot \mathbf{B}(\mathbf{r}') G(\mathbf{r}, \mathbf{r}') dS', \\ \mathbf{A}_t(\mathbf{r}) &= \int_{S'} \varphi_n(\mathbf{r}') \mathbf{G}_t(\mathbf{r}; \mathbf{r}', \mathbf{n}(\mathbf{r}')) dS'. \end{aligned} \quad (3.17)$$

The evaluation of the surface integrals was performed over the six faces of the rectangular volume presented in section 4.2 (the same for all the points). The

integrals were evaluated using the *midpoint rule* explained in section 3.2. To perform all these summations is computationally really slow. For this reason, it has to be remembered that this method, even though it is divergence-free-wise the best one, it is also very time consuming. Once obtained the value of $\mathbf{A} = \mathbf{A}_n + \mathbf{A}_t$, this value was interpolated with the cubic interpolation method introduced in section 3.3.2. In the following chapters, we are going to refer to this method with the name SECOND.

3.2 Quadrature Formulae

In this section we are going to briefly introduce the quadrature formula that was used for the approximation of the integrals applied in the work performed at CERN. More details on this topic can be found in [QSS10]. The quadrature formulae are used to approximate the value of a generic integral:

$$I(f) = \int f(x)dx. \quad (3.18)$$

With the *Newton-Cotes Formulae*, the finite integral (3.18) is approximated using a Lagrange polynomial of order n to $I_n(f)$, interpolating $f(x)$ through n *equispaced* points x_k , $k \in [0, n]$. The midpoint, trapezoidal and Simpson formulae are special instances of the Newton-Cotes formulae, taking $n = 0$, $n = 1$ and $n = 2$ respectively. More formally:

Definition 3.2.1. Assume that the value of the function f defined on $[a, b]$ is known at equally spaced points x_k , for $k = 0, \dots, n$, where $x_0 = a$ and $x_n = b$. A Newton-Cotes formula is said to be of the *closed* type if it uses the function value at all points, otherwise it is called *open*, when it does not use the function values at the endpoints. The closed Newton-Cotes formula of degree n is stated as:

$$I_n(f) = \int_a^b f(x) dx \approx \sum_{k=0}^n w_k f(x_k)$$

where $x_k = kh + x_0$, with h (called the step size) equal to $(x_n - x_0)/n = (b - a)/n$. The w_k are called weights.

The quadrature weights are derived from the Lagrange basis polynomials and they depend only on n . Indeed, let $L(x)$ be the interpolation polynomial in the Lagrange form for the given data points $(x_0, f(x_0)), \dots, (x_n, f(x_n))$, then:

$$\begin{aligned} \int_a^b f(x) dx &\approx \int_a^b L(x) dx = \int_a^b \left(\sum_{k=0}^n f(x_k) l_k(x) \right) dx \\ &= \sum_{k=0}^n f(x_k) \underbrace{\int_a^b l_k(x) dx}_{w_k}. \end{aligned}$$

where $l_k(x)$ is the k^{th} Lagrange base polynomial of degree n .

The simplest method of this type is using an interpolating function that is a constant

(a polynomial of degree zero). This method is called *midpoint rule* or *rectangle rule*. This formula is obtained by replacing f over $[a, b]$ with the constant function equal to the value attained by f at the midpoint of $[a, b]$. This yields:

$$I_0 = (b - a)f\left(\frac{a + b}{2}\right),$$

with weight $w = b - a$ and node $x_0 = (a + b)/2$. In this case, it is possible to estimate the *quadrature error* $E_0 = I(f) - I_n(f)$. By expanding f in a Taylor series around $c = (a + b)/2$ and truncating at the second order, we get:

$$f(x) = f(c) + f'(c)(x - c) + \frac{f''(\eta(x))(x - c)^2}{2},$$

from which, integrating on (a, b) and using the mean-value theorem, we get:

$$E_0(f) = \frac{h^3}{3}f''(\xi), \quad h = \frac{b - a}{2},$$

where $\xi \in (a, b)$.

It should be pointed out that, if the width of the integration interval $[a, b]$ is not sufficiently small, the quadrature error can be quite large. This drawback is common to all the numerical integration formulae, which lead to the introduction of their *composite* counterparts. These methods are called composite since they repeatedly apply the simple formulae derived previously to cover longer intervals. Suppose now that we approximate the integral $I(f)$ by replacing f over $[a, b]$ with its composite interpolating polynomial of degree zero, constructed on m sub-intervals of width $H = (b - a)/m$, for $m \geq 1$. Introducing the quadrature nodes $x_k = a + (2k + 1)H/2$, we get the composite midpoint formula:

$$I_{0,m} = H \sum_{k=0}^{m-1} f(x_k) = \frac{(b - a)}{m} \sum_{k=0}^{m-1} f(x_k), \quad m \geq 1.$$

In this case, the quadrature error $E_{0,m}(f) = I(f) - I_{0,m}(f)$ is given by:

$$E_{0,m}(f) = \frac{b - a}{24} H^2 f''(\xi), \quad H = \frac{b - a}{m},$$

provided that $f \in \mathcal{C}^2$ and where $\xi \in (a, b)$.

The integrals computed with the code implemented at CERN use this simple technique. In future implementations, some effort might be spent in improving this aspect, opting for a more efficient and fast strategy.

3.3 Interpolation Methods

In this section, we are going to present the interpolation methods we used in this thesis. In the work done and CERN and at Politecnico di Milano, different methods were considered.

In the first case, a linear and a cubic spline were implemented. The linear interpolation, despite its simplicity, is generally used in particle tracking. Indeed, given a grid with a dense concentration of interpolating points, the error can be considered tolerable, and this method is usually chosen because of its speed and simple implementation. For this reason, we used this technique to interpolate the analytic magnetic field \mathbf{B} sampled on a three dimensional grid (see chapter 4.2). On the other hand, an original cubic spline was developed. This technique, ensuring a \mathcal{C}^2 regularity, was applied to interpolate the re-elaborated vector potential \mathbf{A} obtained with both the post-processing methods presented in section 3.1.

During the tests performed in Politecnico di Milano, the effects of interpolation on the integration procedure were analysed. In this framework, three classical MATLAB interpolators were used: linear interpolation, cubic interpolation and the cubic spline interpolation. In this case, these methods were all applied to the analytic vector potential. The results of this comparison are reported in section 4.3.

3.3.1 Linear Interpolation

Linear interpolation is one of the simplest polynomial interpolation procedures. It is a fast and easy to implement algorithm but it does not produce very smooth results.

In the one-dimensional case, for a value x_c in the interval (x_0, x_1) , the corresponding value y_c along the straight line is given from the equation of slopes:

$$\frac{y_c - y_0}{x_c - x_0} = \frac{y_1 - y_0}{x_1 - x_0}.$$

Solving this equation for y_c , gives:

$$y_c = y_0 + (x_c - x_0) \frac{y_1 - y_0}{x_1 - x_0},$$

which can be rewritten as:

$$\begin{aligned} y_c &= y_0 \left(1 - \frac{x_c - x_0}{x_1 - x_0} \right) + y_1 \left(\frac{x_c - x_0}{x_1 - x_0} \right) \\ &= y_0 \left(\frac{x_1 - x_c}{x_1 - x_0} \right) + y_1 \left(\frac{x_c - x_0}{x_1 - x_0} \right), \end{aligned}$$

This formula can be interpreted as a weighted average. The weights are inversely related to the distance from the end points to the unknown point: the closer point has more influence than the farther point.

These results can be extended to the 3D case, where we talk about trilinear interpolation. In the following, we will refer to this method as LINT.

3.3.2 Cubic Interpolation

A common, widely used cubic interpolation method is the so called Catmull-Rom spline [CR74]. However, this kind of method only ensure a \mathcal{C}^1 continuity of the piecewise polynomials considered. In order to reconstruct the field preserving its divergence free properties (see section 3.1), a \mathcal{C}^2 continuous interpolation is needed. For this reason, in the tests performed at CERN, a particular form of \mathcal{C}^2 -cubic spline has been used, constructed modifying the Catmull Rom interpolation method.

The Catmull-Rom spline is an interpolation method which belongs to the class of *Cubic Hermite splines*. A generic cubic Hermite spline is an interpolation method over an interval using a third-degree polynomial, written in its Hermite forms [SB13], i.e. specified by its values of the function and its first derivative at the boundaries of its domain. For example, the Cubic Hermite spline $p(t)$ over the interval $[0, 1]$ is given by:

$$p(t) = (2t^3 - 3t^2 + 1) \cdot y_0 + (t^3 - 2t^2 + t) \cdot m_0 + (-2t^3 + 3t^2) \cdot y_1 + (t^3 - t^2) \cdot m_1.$$

where y_0 , y_1 and m_0 , m_1 are respectively the function and the derivative values at the boundaries. The Catmull-Rom spline estimates the derivative values using a centered finite difference. For example, the derivative value m_0 at $t_0 = 0$ is estimated using the values y_{-1} at $t_{-1} = -1$ and y_1 at $t_1 = 1$:

$$m_0 = \frac{y_1 - y_{-1}}{2}.$$

So, given the control points (y_{-1}, y_0, y_1, y_2) computed at $t_{-1} = -1$, $t_0 = 0$, $t_1 = 1$, $t_2 = 2$, the interpolated value $p(t)$ at the points $t \in [0, 1]$ is:

$$p(t) = \begin{bmatrix} 1 & t & t^2 & t^3 \end{bmatrix} \begin{bmatrix} 1 & 0 & 0 & 0 \\ 0 & 0 & 1 & 0 \\ -3 & 3 & -2 & -1 \\ 2 & -2 & 1 & 1 \end{bmatrix} \begin{bmatrix} y_0 \\ y_1 \\ \frac{y_1 - y_{-1}}{2} \\ \frac{y_2 - y_0}{2} \end{bmatrix},$$

which can be simplified in:

$$p(t) = \frac{1}{2} \begin{bmatrix} 1 & t & t^2 & t^3 \end{bmatrix} \begin{bmatrix} 0 & 2 & 0 & 0 \\ -1 & 0 & 1 & 0 \\ 2 & -5 & 4 & -1 \\ -1 & 3 & -3 & 1 \end{bmatrix} \begin{bmatrix} y_{-1} \\ y_0 \\ y_1 \\ y_2 \end{bmatrix} \quad (3.19)$$

The Hermite spline interpolation allows to interpolate using only sampled values near the interpolation point, in contrast to the global nature of more common cubic spline functions.

We present now the \mathcal{C}^2 -cubic spline we developed during the internship at CERN. Let us consider the one-dimensional cubic spline for a set of $n + 1$ points (y_0, \dots, y_n) . The i^{th} piece of the spline is represented by:

$$p_i(t) = a_i + b_i t + c_i t^2 + d_i t^3. \quad (3.20)$$

where a_i, b_i, c_i and d_i are four constants that characterize the polynomial function, $t \in [0, 1]$ and $i = 0, \dots, n-1$. This interpolation imposes a \mathcal{C}^0 , \mathcal{C}^1 and \mathcal{C}^2 continuity of the reconstructed function. In particular, we imposed the continuity of the first and the second derivatives in the interior points, while on the end points we fixed the exact function value on the boundaries ($p_0(0) = y_0$ and $p_{n-1}(1) = y_n$). Moreover, the second derivative was set to zero at the end points. Like for the Catmull Rom splines, the first and second derivative values are approximated by centered finite differences. For example, the derivative value m_1 at t_1 is estimated using the values y_0 at t_0 and y_2 at t_2 :

$$m_1 = \frac{y_2 - y_0}{2}.$$

The second derivative value M_1 in the same point t_1 is defined as:

$$M_1 = \frac{y_2 - 2y_1 + y_0}{2}.$$

For the end points, it was necessary to implement one-sided finite differences for the derivative values (respectively forward and backwards). For this reason, the interpolating functions $p_0(t)$ and $p_{n-1}(t)$ are different from the one for the interior points.

For example, given the control points (y_0, y_1, y_2, y_3) computed at $t_0 = 0, t_1 = 1, t_2 = 2, t_3 = 3$, the interpolated piece-wise polynomials, for $t \in [0, 1]$, are:

$$p_0(t) = \frac{1}{6} \begin{bmatrix} 1 & t & t^2 & t^3 \end{bmatrix} \begin{bmatrix} 6 & 0 & 0 & 0 \\ -6 & 6 & 0 & 0 \\ 0 & 0 & 0 & 0 \\ 1 & -2 & 1 & 0 \end{bmatrix} \begin{bmatrix} y_0 \\ y_1 \\ y_2 \\ y_3 \end{bmatrix} \quad (3.21)$$

$$p_j(t) = \frac{1}{2} \begin{bmatrix} 1 & t & t^2 & t^3 \end{bmatrix} \begin{bmatrix} 1 & 4 & 1 & 0 \\ -3 & 0 & 3 & 0 \\ 3 & -6 & 3 & 0 \\ -1 & 3 & -3 & 1 \end{bmatrix} \begin{bmatrix} y_0 \\ y_1 \\ y_2 \\ y_3 \end{bmatrix} \quad (3.22)$$

$$p_{n-1}(t) = \frac{1}{2} \begin{bmatrix} 1 & t & t^2 & t^3 \end{bmatrix} \begin{bmatrix} 0 & -1 & -4 & 1 \\ 0 & 3 & 0 & 3 \\ 0 & -3 & 6 & 3 \\ 0 & 3 & -2 & -1 \end{bmatrix} \begin{bmatrix} y_0 \\ y_1 \\ y_2 \\ y_3 \end{bmatrix} \quad (3.23)$$

where $j = 1, \dots, n-2$ is equal to the index i , without the end points.

Let us consider, for example, the function $f(t) = \sin\left(\frac{\pi t}{2}\right)$, from which we sampled the points (y_0, \dots, y_4) at $t_0 = 0, t_1 = 1, t_2 = 2, t_3 = 3$ and $t_4 = 4$. In figures 3.1, 3.2 and 3.3, the interpolating function retrieved with the cubic spline and the Catmull Rom spline are shown. As we can see from figure 3.3, the cubic spline implemented ensures the continuity of the second derivative. However, it is clear that the accuracy of the reconstruction provided by this cubic spline is inferior. Nevertheless, for our scope, the precision will be shown to be competitive with other classical methods, with the extra feature of preserving the \mathcal{C}^2 continuity and reducing the computational cost with respect to the global cubic splines described in section 3.3.3, for whose computation the solution of a linear system is necessary.

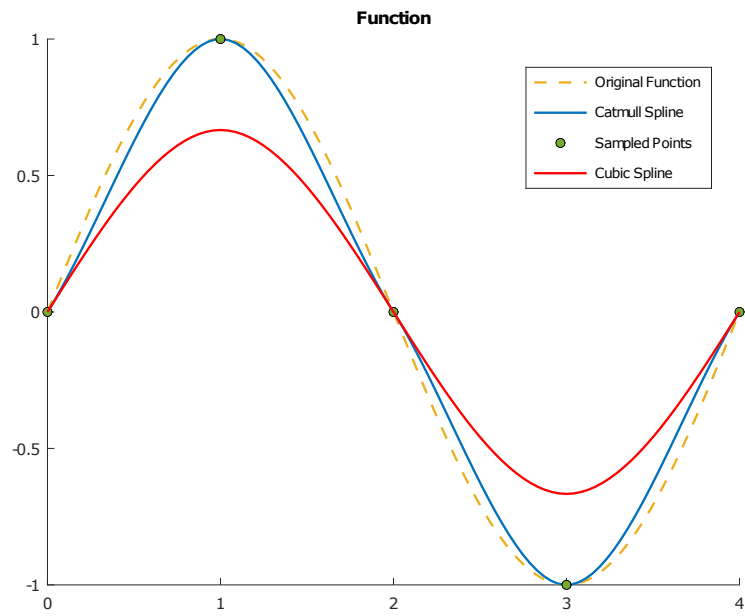


Figure 3.1: Interpolation comparison.

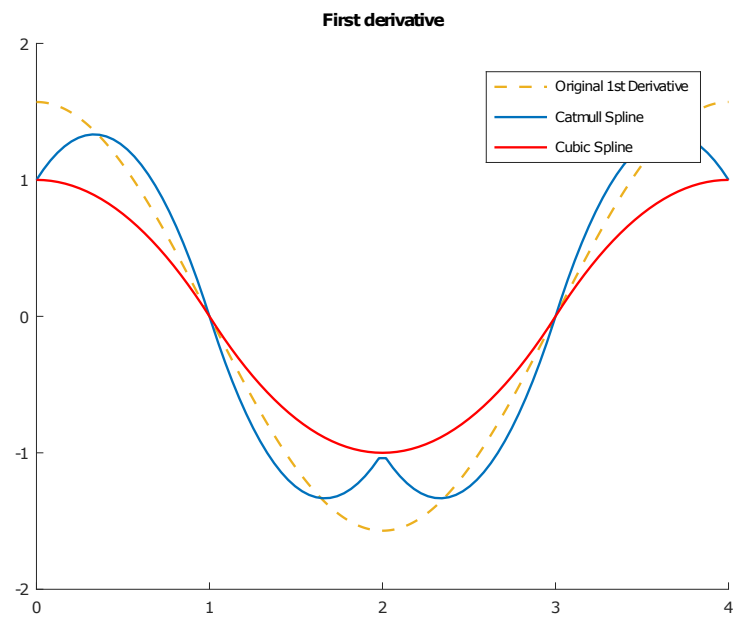


Figure 3.2: First derivative of the interpolated function.

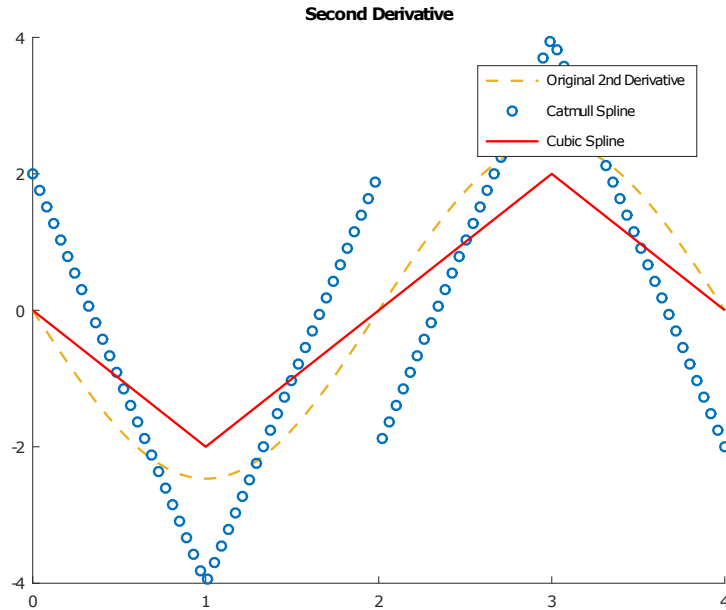


Figure 3.3: Second derivative of the interpolated function.

3.3.3 Global Cubic Splines

This kind of interpolation was used during the tests performed at Politecnico di Milano.

Global *spline* functions, that allow to obtain a piecewise polynomial interpolant that is also differentiable over the whole interval on which it is defined, were considered. These functions are very widely used in applications. For example, they are implemented in the MATLAB command `interp1`.

Definition 3.3.1. Given an interval $[a, b]$ and interpolation data (x_i, y_i) , $i = 0, \dots, n$ with $x_0 = a < x_1 < \dots < x_n = b$, a function $s(x)$ is said to be a *spline* of degree p and of order k if, for any $i = 0, \dots, n-1$, for $x \in [x_i, x_{i+1}]$ the function $s(x)$ coincides with a polynomial of degree p that satisfies the interpolation conditions $s(x_i) = y_i$ and at the same time $s \in \mathcal{C}^{(k)}[a, b]$.

The order and degree of a spline function cannot be arbitrary, but they must satisfy appropriate relationships for the existence of a function with the above characteristics to be guaranteed. Among the most widely used spline functions are those of degree 3 and order 2, also known generally as cubic splines.

Definition 3.3.2. Given an interval $[a, b]$ and interpolation data (x_i, y_i) , $i = 0, \dots, n$ with $x_0 = a < x_1 < \dots < x_n = b$, a function $s(x)$ is said to be a *natural cubic spline* if, for any $i = 0, \dots, n-1$, for $x \in [x_i, x_{i+1}]$ one has $s(x_i) = y_i$ with

$$s(x) = \alpha_i + \beta_i(x - x_i) + \gamma_i(x - x_i)^2 + \delta_i(x - x_i)^3,$$

where $\alpha_i, \beta_i, \gamma_i$ and δ_i are four constants and furthermore $s \in \mathcal{C}^2[a, b]$ and $s^{(2)}(a) = s^{(2)}(b) = 0$.

Definition 3.3.3. Given an interval $[a, b]$ and interpolation data (x_i, y_i) , $i = 0, \dots, n$ with $x_0 = a < x_1 < \dots < x_n = b$, a function $s(x)$ is said to be a *periodic cubic spline* if, for any $i = 0, \dots, n-1$, for $x \in [x_i, x_{i+1}]$ one has $s(x_i) = y_i$ with

$$s(x) = \alpha_i + \beta_i(x - x_i) + \gamma_i(x - x_i)^2 + \delta_i(x - x_i)^3,$$

and furthermore $s \in \mathcal{C}^2[a, b]$ and $s^{(1)}(a) = s^{(1)}(b)$, $s^{(2)}(a) = s^{(2)}(b)$.

Theorem 3.3.1. *Given an interval $[a, b]$ and interpolation data (x_i, y_i) , $i = 0, \dots, n$ with $x_0 = a < x_1 < \dots < x_n = b$, there is a unique function $s(x)$ that is a natural cubic spline defined by the given interpolation data.*

Denote by $h_i = x_{i+1} - x_i$ the distance between two consecutive interpolation nodes. Using the same notation as in definition 3.3.2, the conditions on the coincidence of the left and right limit with the interpolation datum in the internal nodes can be expressed as:

$$\begin{aligned} \alpha_i &= y_i, & i &= 0, \dots, n-1 \\ y_{i+1} &= \alpha_i + \beta_i h_i + \gamma_i h_i^2 + \delta_i h_i^3, & i &= 0, \dots, n-1 \end{aligned}$$

These conditions imply that all the coefficients α_i are automatically determined from the interpolation conditions. Furthermore, rewriting the second equation as:

$$\beta_i = \frac{y_{i+1} - y_i}{h_i} - \gamma_i h_i - \delta_i h_i^2, \quad i = 0, \dots, n-1$$

it is clear that the coefficients β_i can be determined if the values of γ_i, δ_i , are known. In order to impose the continuity conditions on the spline derivatives, notice that for $x \in [x_i, x_{i+1}]$ one has:

$$\begin{aligned} s(x) &= \alpha_i + \beta_i(x - x_i) + \gamma_i(x - x_i)^2 + \delta_i(x - x_i)^3, \\ s'(x) &= \beta_i + 2\gamma_i(x - x_i) + 3\delta_i(x - x_i)^2, \\ s''(x) &= 2\gamma_i + 6\delta_i(x - x_i). \end{aligned}$$

These expressions and the definition of $\gamma_n = s''(b)/2$ imply that:

$$\begin{aligned} 2\gamma_i &= 2\gamma_{i-1} + 6\delta_{i-1}h_{i-1} & i &= 1, \dots, n \\ \beta_i &= \beta_{i-1} + 2\gamma_{i-1}h_{i-1} + 3\delta_{i-1}h_{i-1}^2 & i &= 1, \dots, n-1. \end{aligned}$$

Rewriting the first equation in order to express the coefficients δ_i as a function of the coefficients γ_i and using the expression of β_i derived previously, one obtains for γ_i :

$$\begin{aligned} &\frac{y_{i+1} - y_i}{h_i} - \gamma_i h_i - \frac{\gamma_{i+1} - \gamma_i}{3h_i} h_i^2 \\ &= \frac{y_i - y_{i-1}}{h_{i-1}} - \gamma_{i-1} h_{i-1} - \frac{\gamma_i - \gamma_{i-1}}{3h_{i-1}} h_{i-1}^2 \\ &+ 2\gamma_{i-1} h_{i-1} + 3h_{i-1}^2 \frac{\gamma_i - \gamma_{i-1}}{3h_{i-1}}, \end{aligned} \tag{3.24}$$

which can then be rewritten as:

$$\begin{aligned} & \gamma_{i-1}h_{i-1} + 2\gamma_i(h_{i-1}h_i) + \gamma_{i+1}h_i \\ & = 3 \left[\frac{y_{i+1} - y_i}{h_i} - \frac{y_i - y_{i-1}}{h_{i-1}} \right] \quad i = 1, \dots, n-1. \end{aligned} \quad (3.25)$$

In this way, $n - 1$ linear equations in the $n + 1$ unknowns γ_i are obtained. In order to obtain a number of equations equal to the number of unknowns, the boundary conditions $s^{(2)}(a) = s^{(2)}(b) = 0$ must be imposed, which amount to set $\gamma_0 = \gamma_n = 0$.

Global spline interpolation allows to obtain a piecewise polynomial approximation that approximates the derivatives of the interpolated function well, along with the function itself. Standard piecewise polynomial interpolants, instead, approximate locally also the interpolated function derivatives, but yield in general non-differentiable functions at the nodes shared by two local interpolants. On the other hand, the numerical solution of a linear system, required for the determination of the global spline coefficients, requires a greater computational effort than the simpler, local formulae introduced in section 3.3.1.

Theorem 3.3.2. *Given the interval $[a, b]$ and the interpolation data (x_i, y_i) , $i = 0, \dots, n$ such that $x_0 = a < x_1 < \dots < x_n = b$, if $g \in \mathcal{C}^4[a, b]$ and if g satisfies the interpolation conditions $g(x_i) = y_i$, $i = 0, \dots, n$, then, denoting by $s(x)$ the natural cubic spline defined by the assigned interpolation data and setting $h_i = x_i - x_{i-1}$, $h = \max h_i$, one has*

$$\begin{aligned} \max_{x \in [a, b]} |s(x) - g(x)| & \leq \max_{x \in [a, b]} |g^{(4)}(x)| \frac{5}{384} h^4 \\ \max_{x \in [a, b]} |s'(x) - g'(x)| & \leq \max_{x \in [a, b]} |g^{(4)}(x)| \frac{1}{24} h^3 \\ \max_{x \in [a, b]} |s''(x) - g''(x)| & \leq \max_{x \in [a, b]} |g^{(4)}(x)| \frac{3}{8} h^2. \end{aligned}$$

Furthermore, interpolation by natural cubic splines provides an approximation whose graph has on average a smaller curvature than that of the graph of the interpolated function. This statement can be made more precise by the following theorem.

Theorem 3.3.3. *Given the interval $[a, b]$ and the interpolation data (x_i, y_i) , $i = 0, \dots, n$ where $x_0 = a < x_1 < \dots < x_n = b$, if $g \in \mathcal{C}^2[a, b]$ and if g satisfies the interpolation conditions $g(x_i) = y_i$, $i = 0, \dots, n$, then denoting by $s(x)$ the natural cubic spline defined by the interpolation data one has*

$$\int_a^b [s''(x)]^2 dx \leq \int_a^b [g''(x)]^2 dx.$$

3.4 ODE Integrators

In this section, we compare the different high order integration techniques used in this thesis, in order to assess their accuracy and efficiency for long term simulations. Since the goal of the work performed at CERN was to show clearly the advantages introduced by a divergence-free interpolation, we just applied a stable and precise interpolation method, in order to introduce the minimum amount of error. The integration method used in this case was taken from the GNU Scientific Library [Gou09]. This library provides a variety of methods and components for adaptive step-size control.

On the other hand, the accurate comparison of different methods was the heart of the work done at Politecnico di Milano. For this reason, different methods and their characteristics are presented here.

In order to integrate the equations of motion, integration methods for Ordinary Differential Equations (ODE) are needed. In particular, our goal is to solve systems of the form:

$$\begin{cases} \dot{\mathbf{y}} = \mathbf{f}(t, \mathbf{y}), & t > 0 \\ \mathbf{y}(0) = \mathbf{y}_0 & t = 0 \end{cases}, \quad (3.26)$$

where t is the independent variable and \mathbf{y} and \mathbf{f} are n -dimensional functions. For the problem (3.26), also known as Cauchy problem, there are different results about the existence and the uniqueness of the solution, depending on the regularity of f . The reader can find further information in [QSS10].

First, let us give some basic definitions. Fixed $0 < T < +\infty$, let $I = (t_0, t_0 + T)$ be the integration interval. Correspondingly, for $h > 0$, $h \in \mathbb{R}$, let:

$$t_n = t_0 + nh \quad n = 0, 1, 2, \dots, N_h$$

be the sequence of discretization nodes of I into sub-intervals $I_n = [t_n, t_{n+1}]$. The width h of such sub-intervals is called *discretization step size*. Notice that N_h is the maximum integer such that $t_{N_h} \leq t_0 + T$.

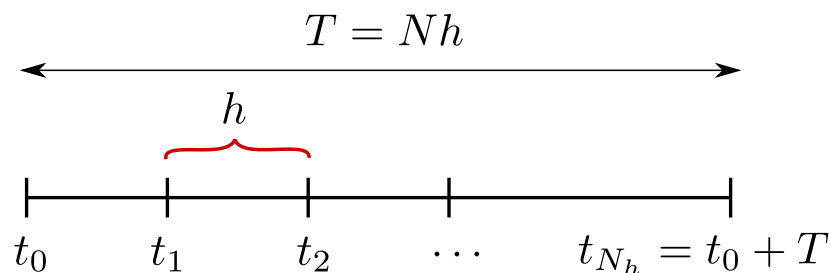


Figure 3.4: Axis of time.

Let u_j be the approximation of the exact solution $y(t_j)$ at node t_j . Similarly, f_j denotes the value $f(t_j, u_j)$. Clearly, let $u_0 = y_0$.

Definition 3.4.1. A numerical method for the approximation of problem (3.26) is called *one-step method* if $\forall n \geq 0$, u_{n+1} depends only on u_n . Otherwise, the scheme is called a *multistep method*.

Moreover:

Definition 3.4.2. A method is called *explicit* if u_{n+1} can be computed directly in terms of (some of) the previous values u_k , $k \leq n$, *implicit* if u_{n+1} depends implicitly on itself through f .

3.4.1 Runge Kutta Methods

The main methods we used are the so called Runge Kutta methods. The most general form for a Runge Kutta method is the following [QSS10]:

$$u_{n+1} = u_n + hF(t_n, u_n, h; f), \quad n \geq 0, \quad (3.27)$$

where F is the increment function defined as:

$$F(t_n, u_n, h; f) = \sum_{i=1}^s b_i K_i, \quad (3.28)$$

$$K_i = f \left(t_n + c_i h, u_n + h \sum_{j=1}^s a_{ij} K_j \right), \quad i = 1, \dots, s.$$

s denotes the number of stages of the method. The coefficients $a_{ij} \in \mathbb{R}^{s \times s}$, $b_i \in \mathbb{R}^s$ and $c_i = \sum_{j=1}^s a_{ij}$ fully characterize a RK method and they are usually collected in the so called *Butcher array*:

$$\begin{array}{c|cccc} c_1 & a_{11} & a_{12} & \dots & a_{1s} \\ c_2 & a_{21} & a_{22} & \dots & a_{2s} \\ \vdots & \vdots & & \ddots & \vdots \\ c_s & a_{s1} & a_{s2} & \dots & a_{ss} \\ \hline & b_1 & b_2 & \dots & b_s \end{array}$$

It is sometimes useful to rewrite the relations (3.27) and (3.28) in a somewhat different form. At each step we introduce intermediate times t_i and coordinates u_i following the rules:

$$t_i = t_n + c_i h, \quad (3.29)$$

$$u_i = u_n + h \sum_{j=1}^s a_{ij} K_j. \quad (3.30)$$

With this convention (3.28) can be rewritten in the form:

$$K_i = f(t_i, u_i). \quad (3.31)$$

Then, the RK definition becomes:

$$u_{n+1} = u_n + h \sum_{i=1}^s b_i f(t_i, u_i), \quad n \geq 0. \quad (3.32)$$

These sets of equations are clearly equivalent but, in this expanded form, it is clear how K_i represents the value of f at the intermediate points.

If the coefficients a_{ij} are equal to zero for $j \geq i$, with $i = 1, 2, \dots, s$, then each K_i can be explicitly computed in terms of their $i - 1$ coefficients K_1, \dots, K_{i-1} that have already been determined. In such a case the RK method is *explicit*. Otherwise, it is *implicit* and solving a non-linear system of size s is necessary for computing the coefficients K_i . Moreover, a RK method can be symplectic or not:

Theorem 3.4.1. *If the coefficients of a Runge-Kutta method satisfy:*

$$b_i a_{ij} + b_j a_{ji} = b_i b_j, \quad \forall j = 1, \dots, s$$

then it is symplectic.

It has to be noticed that all the symplectic RK methods are also implicit methods.

In the realistic case, where the magnetic vector potential is sampled at equidistant points along z , the use of high order methods become difficult. In fact, a general numerical method requires the value of the magnetic vector potential at fixed z coordinate, for example the mid-point method at $(z_n + z_{n+1})/2$. These values can be provided in simple cases, where the z -step is a multiple of the required evaluation points, for example the mid-point method or other second order methods require the value of the vector magnetic field in the middle of the z -step. Therefore, using a doubled z -step for the integration, these values become available. Anyways, in our methods, the magnetic field is re-interpolated every time, in order to get the value of the field also in all the points we may need.

3.4.2 Runge Kutta and Gauss Methods

Another widely used Runge Kutta method is the Fourth Order Runge Kutta (RK4). The RK4 method is a fourth-order method, meaning that the local truncation error is on the order of $O(h^5)$, while the total accumulated error is on the order of $O(h^4)$. The explicit equations for the increment functions are:

$$\begin{aligned} K_1 &= h f(t_n, u_n), \\ K_2 &= h f\left(t_n + \frac{h}{2}, u_n + \frac{K_1}{2}\right), \\ K_3 &= h f\left(t_n + \frac{h}{2}, u_n + \frac{K_2}{2}\right), \\ K_4 &= h f(t_n + h, u_n + K_3), \end{aligned} \quad (3.33)$$

and:

$$\begin{aligned} u_{n+1} &= u_n + \frac{1}{6} (K_1 + 2K_2 + 2K_3 + K_4), \\ t_{n+1} &= t_n + h. \end{aligned} \quad (3.34)$$

In this case the Butcher array is:

$$\begin{array}{c|cccc}
 0 & & & & \\
 \frac{1}{2} & \frac{1}{2} & & & \\
 \frac{1}{2} & 0 & \frac{1}{2} & & \\
 1 & 0 & 0 & 1 & \\
 \hline
 & \frac{1}{6} & \frac{1}{3} & \frac{1}{3} & \frac{1}{6}
 \end{array}$$

Recalling what was stated in Definition 3.4.2, this method is an explicit method, as we can also understand by the fact that the Butcher matrix is strictly lower triangular. It can be also observed that this method is not symplectic since it does not satisfy conditions of Theorem 3.4.1. Gauss methods are particular implicit Runge-Kutta methods which are symplectic. A fourth order gauss method is characterized by the following Butcher tableau:

$$\begin{array}{c|cc}
 \frac{1}{2} - \frac{\sqrt{3}}{6} & \frac{1}{4} & \frac{1}{4} - \frac{\sqrt{3}}{6} \\
 \frac{1}{2} + \frac{\sqrt{3}}{6} & \frac{1}{4} + \frac{\sqrt{3}}{6} & \frac{1}{4} \\
 \hline
 & \frac{1}{2} & \frac{1}{2}
 \end{array}$$

The sixth-order Gauss method is instead characterized by the Butcher tableau:

$$\begin{array}{c|ccc}
 \frac{1}{2} - \frac{\sqrt{15}}{10} & \frac{5}{36} & \frac{2}{9} - \frac{\sqrt{15}}{15} & \frac{5}{36} - \frac{\sqrt{15}}{30} \\
 \frac{1}{2} & \frac{5}{36} + \frac{\sqrt{15}}{24} & \frac{2}{9} & \frac{5}{36} - \frac{\sqrt{15}}{24} \\
 \frac{1}{2} + \frac{\sqrt{15}}{10} & \frac{5}{36} + \frac{\sqrt{15}}{30} & \frac{2}{9} - \frac{\sqrt{15}}{15} & \frac{5}{36} \\
 \hline
 & \frac{5}{18} & \frac{4}{9} & \frac{5}{18}
 \end{array}$$

3.4.3 Runge Kutta Embedded Method

Since RK schemes are one-step methods, they are well-suited to adapting the step size h , provided that an efficient estimator of the local error is available. One possible estimation uses simultaneously two different RK methods with s stages, of order p and $p + 1$, respectively, which share the same set of values K_i . These methods form the group of the so called *embedded methods* [HLW06].

The main method we used is of this kind, and it is called Runge-Kutta Fehlberg. It consists of a method of order $O(h^4)$ with an error estimator of order $O(h^5)$ (for

this reason, it is known as the RK45 method). During the integration, the step size is adapted such that the estimated error stays below a user-defined threshold: if the error is too high, a step is repeated with a lower step size; if the error is much smaller, the step size is increased to save time. This results in an (almost) optimal step size, which saves computation time. The lower-order step is given by:

$$u_{n+1}^* = u_n + h \sum_{i=1}^s b_i^* K_i,$$

where K_i are the same as for the higher-order method. Then, taking the difference between the approximate solutions at t_{n+1} produced by the two methods, we are provided with an estimate of the local truncation error for the scheme of lower order:

$$e_{n+1} = u_{n+1} - u_{n+1}^* = h \sum_{i=1}^s (b_i - b_i^*) K_i,$$

which is $O(h^p)$. The Butcher tableau for this kind of method is extended to give the values of b_i^* :

c_1	a_{11}	a_{11}	\dots	a_{1s}
c_2	a_{21}	a_{22}	\dots	a_{2s}
\vdots	\vdots		\ddots	\vdots
c_s	a_{s1}	a_{s2}	\dots	a_{ss}
	b_1	b_2	\dots	b_s
	b_1^*	b_2^*	\dots	b_s^*

In particular, the Butcher array for the RK45 method is:

0	0	0	0	0	0	0
$\frac{1}{4}$	$\frac{1}{4}$	0	0	0	0	0
$\frac{3}{8}$	$\frac{3}{32}$	$\frac{9}{32}$	0	0	0	0
$\frac{12}{13}$	$\frac{1932}{2197}$	$-\frac{7200}{2197}$	$-\frac{7296}{2197}$	0	0	0
1	$\frac{439}{216}$	-8	$\frac{3680}{513}$	$-\frac{845}{4104}$	0	0
$\frac{1}{2}$	$-\frac{8}{27}$	2	$-\frac{3544}{2565}$	$\frac{1859}{4104}$	$-\frac{11}{40}$	0
$\frac{25}{216}$	0	$\frac{1408}{2565}$	$\frac{2197}{4104}$	$-\frac{1}{5}$	0	
$\frac{16}{135}$	0	$\frac{6656}{12825}$	$\frac{28561}{56430}$	$-\frac{9}{50}$	$\frac{2}{55}$	

3.4.4 Step-Size Adaptive Methods

The GSL library provided us with multiple functions. In particular, the *adaptive step size control function* examines the proposed change to the solution produced by a stepping function and attempts to determine the optimal step-size for a user-specified level of error. The step-size adjustment procedure for this method begins by computing the desired error level D_i for each component. This error is obtained by adding the absolute and the relative error (properly weighted) set by the user:

$$D_i = \varepsilon_{abs} + \varepsilon_{rel} \cdot (a_y |y_i| + a_{dydt} h |y_i'|),$$

with a_y and a_{dydt} scaling factors for the system state $y(t)$ and derivatives $y'(t)$ respectively. This desired error is compared with the observed error $E_i = |y_{err_i}|$. If the observed error E exceeds the desired error level D by more than 10% for any component then the method reduces the step-size by an appropriate factor:

$$h_{new} = h_{old} \cdot S \cdot (E/D)^{-1/q},$$

where q is the consistency order of the method (e.g. $q=4$ for 4(5) embedded RK), and S is a safety factor of 0.9. The ratio E/D is taken to be the maximum of the ratios E_i/D_i . If the observed error E is less than 50% of the desired error level for the maximum ratio E_i/D_i , then the algorithm takes the opportunity to increase the step-size to bring the error in line with the desired level,

$$h_{new} = h_{old} \cdot S \cdot (E/D)^{-1/(q+1)}.$$

This encompasses all the standard error scaling methods.

3.5 Error Evaluation

Calling $f(x)$ the exact solution of a specific problem and $I(x)$ the approximated function of the exact solution. x is a set of discrete values $[x_1, \dots, x_n]$ over which the two functions are defined. The approximation error is defined as:

$$e(x) = \sum_{i=0}^n e(x_i) = \sum_{i=0}^n |f(x_i) - I(x_i)|. \quad (3.35)$$

In order to measure the quality of an algorithm, various error norms can be used. This evaluation gives a way to describe the distance of the approximation from the exact solution. The absolute L^2 error is computed as:

$$\varepsilon_{A,L^2} = \|e(x)\|_{L^2} = \left\| \sum_{i=0}^n e(x_i) \right\|_{L^2} = \sqrt{\sum_{i=0}^n e(x_i)^2}. \quad (3.36)$$

Another common method is the absolute L^∞ error, which computes the magnitude of the largest component of $e(x)$:

$$\varepsilon_{A,L^\infty} = \|e(x)\|_{L^\infty} = \left\| \sum_{i=0}^n e(x_i) \right\|_{L^\infty} = \max_{i \in [0, \dots, n]} |e(x_i)|. \quad (3.37)$$

The relative L^2 error is:

$$\varepsilon_{R,L^2} = \frac{\|e(x)\|_{L^2}}{\|f(x)\|_{L^2}} = \frac{\|\sum_{i=0}^n e(x_i)\|_{L^2}}{\|\sum_{i=0}^n f(x_i)\|_{L^2}} = \frac{\sqrt{\sum_{i=0}^n e(x_i)^2}}{\sqrt{\sum_{i=0}^n f(x_i)^2}}. \quad (3.38)$$

The relative L^∞ error:

$$\varepsilon_{R,L^\infty} = \frac{\|e(x)\|_{L^\infty}}{\|f(x)\|_{L^\infty}} = \frac{\|\sum_{i=0}^n e(x_i)\|_{L^\infty}}{\|\sum_{i=0}^n f(x_i)\|_{L^\infty}}. \quad (3.39)$$

In our analysis we mainly used the relative error, in the L^2 and L^∞ norm.

Chapter 4

Numerical Experiments

In this chapter the numerical experiments performed are presented. In the first and second sections, the precise scheme of coils and the discrete mesh used are explained. Afterwards, the results of the comparison between integration methods performed at Politecnico is introduced. In the end, the particle tracking tests run at CERN are described and commented.

4.1 Modeling the System of Coils

We are considering a system of coils with opposite currents, where each coil has a radius $r = 0.15$ m and a distance $d = 0.2$ m one from the other. We set the on-axis

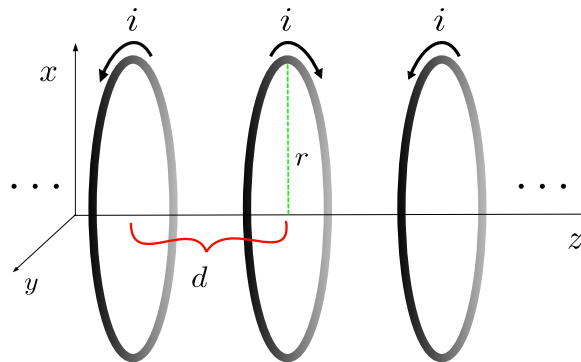


Figure 4.1: Scheme of the system of coils.

B_z field of each coil equal to $B_z = 3$ T and the canonical momentum $P_0 = 50 \frac{\text{MeV}}{c}$.

It has to be noticed that with these specific values of radius and distance, the magnetic fields of each coil influence those of the neighbouring coils, leading to a change of the overall field along the z axis. As we can observe in figure 4.2, these fringe effects are mainly localized at the edges of the system.

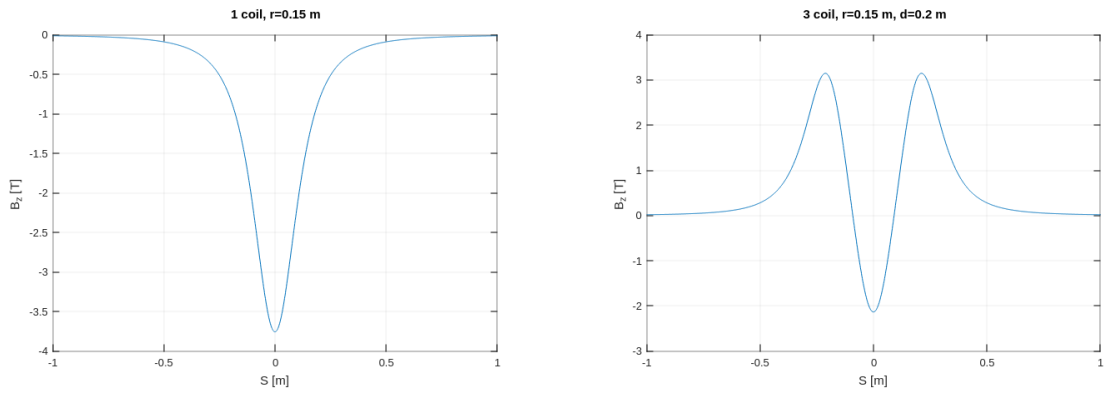


Figure 4.2: Magnetic field variation with number of coils: one coil versus three coils.

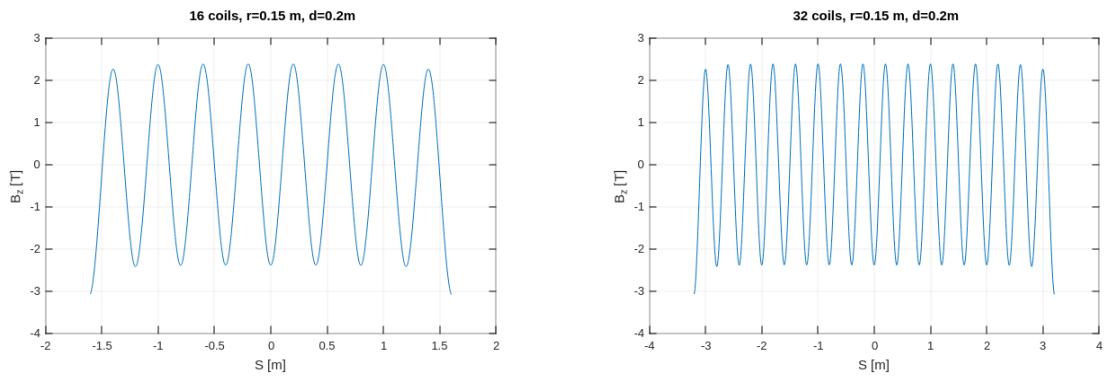


Figure 4.3: Magnetic field variation with number of coils: 16 coils versus 32 coils.

In order to concentrate these fringe effects in regions where they do not excessively affect the particle dynamics, we choose a system composed by 200 coils with opposite currents, 100 placed before the origin of the z axis, 100 placed after. In this way,

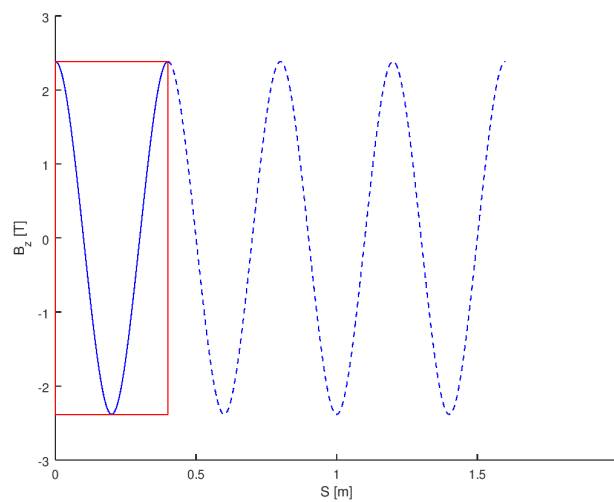


Figure 4.4: Periodic construction of the magnetic field. In red, the elementary unit formed by two coils, then repeated along the z axis four times.

the behavior of the field around the origin of the z axis was more uniformly affected by the fringes, showing a constant on-axis magnetic field. We then selected only the two central coils (the coil in zero, half coil in -0.2 and half coil in 0.2), and we repeated this unit four times, starting from the origin of the axis. The resulting system was finally composed by 8 coils, extending from 0 to 1.6 m. In this way we obtained an ideal periodic model of a system of opposite coils, where the fringe effects were assumed negligible.

4.2 Definition of the Discrete Mesh

In this section we describe the discrete mesh on which the magnetic field was considered as known. In order to set the limits of accuracy depending on the grid spacing, we performed an analysis of the interpolation error over different grids. The volume we discretized was placed inside the coils, going from 0 to 1.6 m along the z axis and from 0 to 0.1 m along the x and y axis. This decision was based on the fact that the particles are moving along the system of coils staying relatively close the axis, thanks to the focusing action of the coils. For each grid,

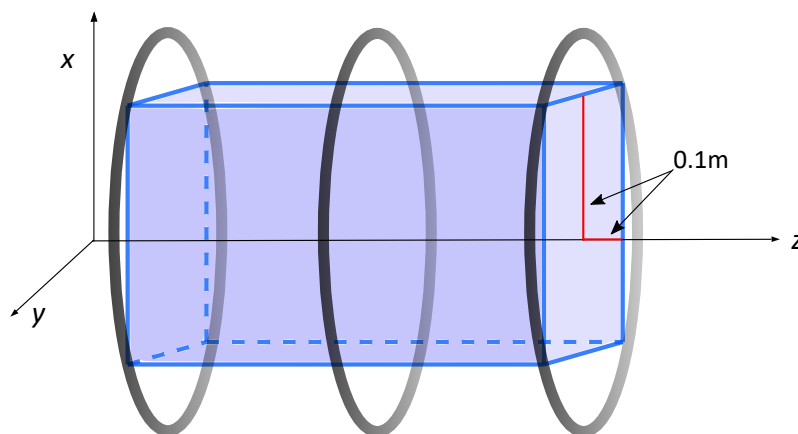


Figure 4.5: Grid for interpolation.

the analytic field was computed at the grid nodes and then reconstructed on a finer mesh by means of three different approaches: 1) the trilinear method (LINT), 2) the first post-processing method (FIRST) described in section 3.1.1 and 3) the second post-processing method (SECOND) described in section 3.1.2, both interpolated with a local cubic interpolation method (see section 3.3.2). This kind of cubic interpolation, even if it preserves the \mathcal{C}^2 continuity of the field, results in a general lower quality of the interpolated field. For this reason, we expect to see errors higher than the ones obtained with usual global cubic interpolation splines.

In Table 4.1, the different meshes and the corresponding steps are shown together with the corresponding relative infinite norm error (3.39). All the interpolated fields show a similar error. However, we can observe that the SECOND method, interpolated with the local cubic spline described in section 3.3.1, returns the least accurate results, while the trilinear and the FIRST one are comparable (see also fig.

mesh size	$\Delta x, y$ [m]	Δz [m]	LINT err	FIRST err	SEC err
$4 \times 4 \times 64$	0.0667	0.0254	1.6416e-01	1.6081e-01	7.2205e-01
$6 \times 6 \times 96$	0.0400	0.0168	5.6369e-02	8.2990e-02	3.5011e-01
$8 \times 8 \times 128$	0.0286	0.0126	2.8442e-02	2.2747e-02	2.1773e-01
$10 \times 10 \times 160$	0.0222	0.0101	1.7119e-02	2.2618e-02	1.5767e-01
$12 \times 12 \times 192$	0.0182	0.0084	1.1428e-02	9.6237e-03	1.2352e-01
$14 \times 14 \times 224$	0.0154	0.0072	8.1657e-03	1.0120e-02	1.0152e-01
$16 \times 16 \times 256$	0.0133	0.0063	6.1315e-03	5.3651e-03	8.6181e-02
$18 \times 18 \times 288$	0.0117	0.0056	4.7675e-03	5.6661e-03	7.4871e-02
$20 \times 20 \times 320$	0.0105	0.0050	3.8172e-03	3.4323e-03	6.6189e-02
$22 \times 22 \times 352$	0.0095	0.0046	3.1218e-03	3.6055e-03	5.9313e-02
$24 \times 24 \times 384$	0.0087	0.0042	2.6013e-03	2.3854e-03	5.3733e-02
$26 \times 26 \times 416$	0.0080	0.0039	2.2059e-03	2.4911e-03	4.9114e-02
$28 \times 28 \times 448$	0.0074	0.0036	1.8908e-03	1.7542e-03	4.5228e-02
$30 \times 30 \times 480$	0.0069	0.0033	1.6366e-03	1.8225e-03	4.1912e-02
$32 \times 32 \times 512$	0.0065	0.0031	1.4323e-03	1.3442e-03	3.9049e-02
$34 \times 34 \times 544$	0.0061	0.0029	1.2657e-03	1.3906e-03	3.6553e-02

Table 4.1: Grid steps and Infinite Norm errors with the different interpolation methods

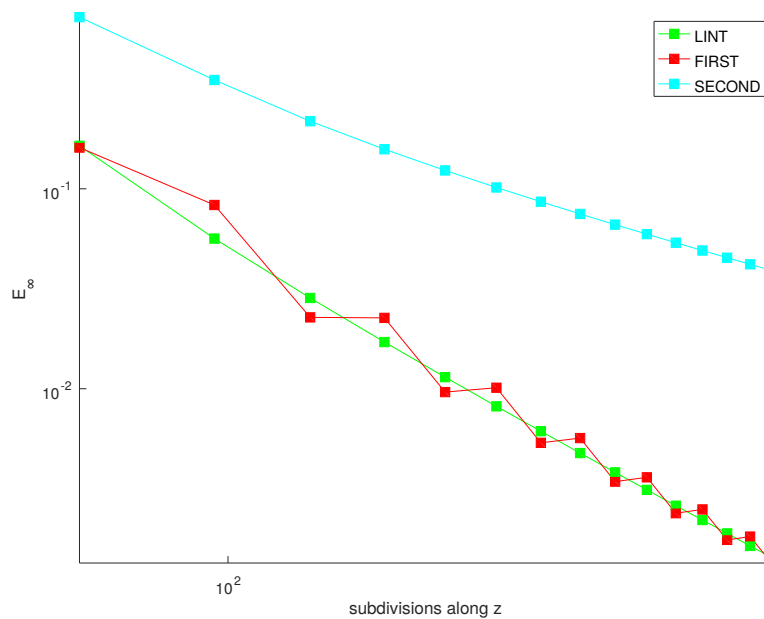


Figure 4.6: Interpolation error changing the grid size

4.6). A possible reason of this behavior lies in the quadrature methods employed in the implementation of the SECOND method. Indeed, as we explained in section 3.1.2, the computation of the surface integrals (3.17) is performed through the midpoint quadrature rule. As explained in section 3.2, this is the simplest numerical integration methods, introducing a quite high error. In future implementations, the usage of more accurate methods will be of first importance.

The resolution of the grid is chosen in order to guarantee that the error is below a given threshold, set around 10^{-2} . A good grid could be taken considering $\Delta x = \Delta y \leq 0.0065$ m (32×32) and $\Delta z \leq 0.0029$ m (512). In this specific case, we obtained the L^∞ and L^2 errors shown in Table 4.2.

	Infinite error	L^2 error
LINT	1.4323e-03	1.0917e-03
FIRST	1.3442e-03	1.2590e-03
SECOND	3.9049e-02	2.5608e-02

Table 4.2: Errors in the $32 \times 32 \times 512$ case.

In fig. 4.7 we can see that the general behavior of the field is preserved, even if the lack of accuracy of SECOND approach is clear. In particular, figures 4.8 and 4.9 show the reconstructed field errors with respect to the analytic field.

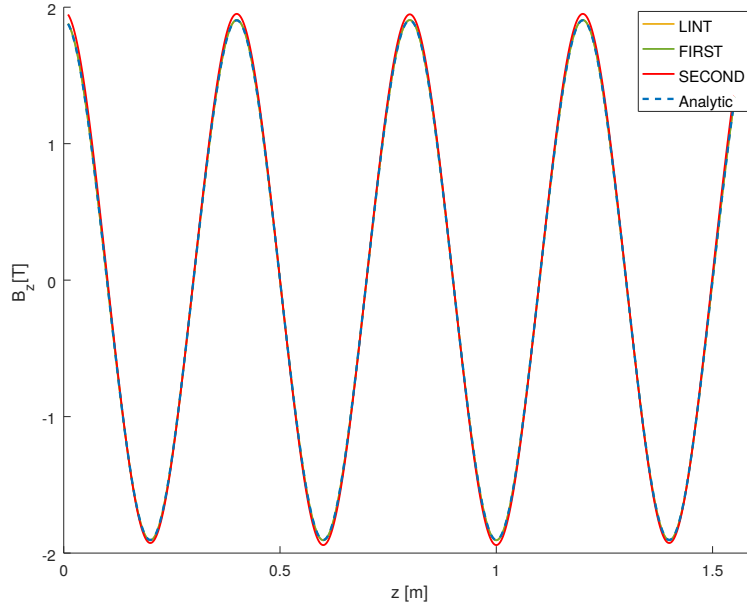


Figure 4.7: Overall interpolated field.

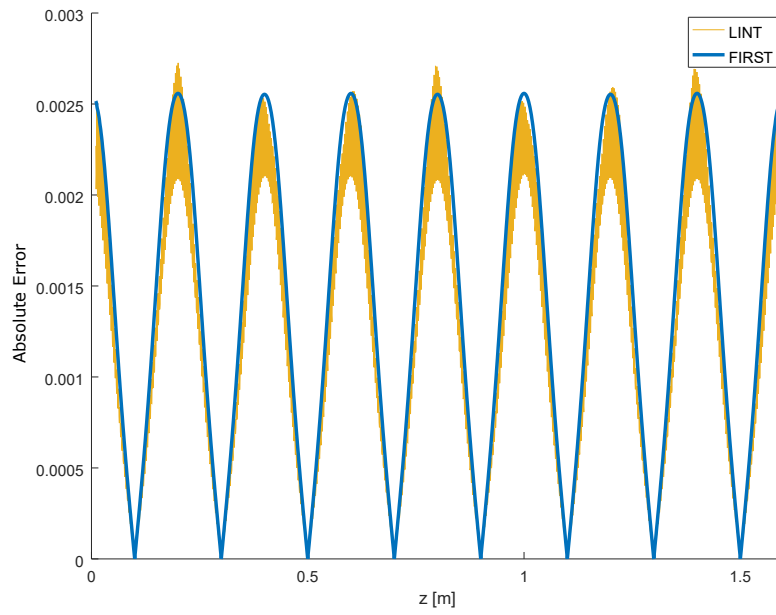


Figure 4.8: Absolute error for the FIRST post-processing method.

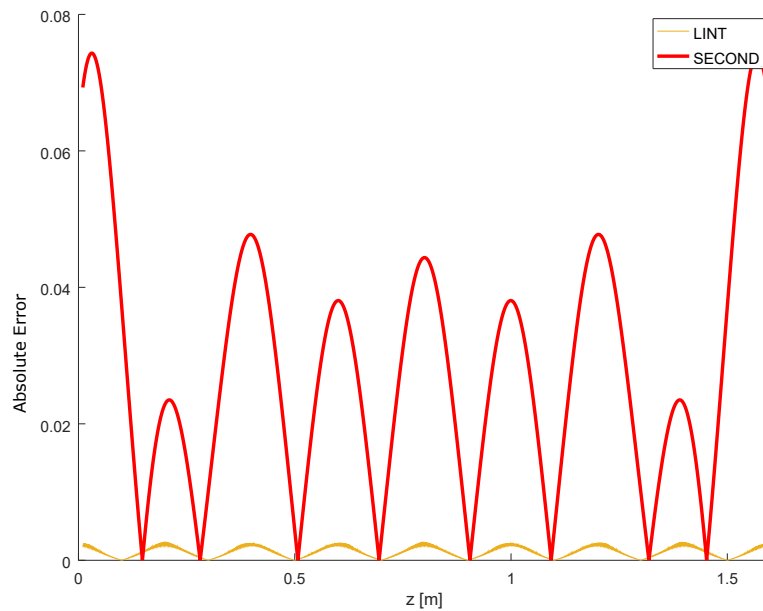


Figure 4.9: Absolute error for the SECOND post-processing method.

4.3 Comparison of Different Integration Methods

In this section, several high order integration techniques will be compared, in order to assess their accuracy and efficiency for long-term simulations. The tests were performed following the procedure presented in [Sim+19]. As we discussed in section 1.4, for the system of coils considered here, the exact analytic expression of the vector potential is available. In this way, the Maxwell equation are theoretically satisfied everywhere and unwanted spurious contributions are avoided. The magnetic vector potential is the one described at (1.28), with z as independent variable. The ODE system that has to be solved is given in (2.41).

The particle tracking was performed simulating the passage of an electron, with rest mass $m = 0.5109989461 \text{ MeV}/c^2 = 9.109383 \cdot 10^{-31} \text{ kg}$ and charge $q = -1.602176 \cdot 10^{-19} \text{ C}$, through a sequence of 4 coils leading opposite currents, placed one next to the other around the $z = 0$. We choose a reference momentum $P_0 = 50 \text{ MeV}/c$, resulting in a total energy equal to $E = 50 \text{ MeV}$. The initial conditions for the transverse positions and momenta of the particle are set to $\mathbf{w}_0 = (0.02, 0.04, -2, 0)$ m and $\delta_0 = 0$.

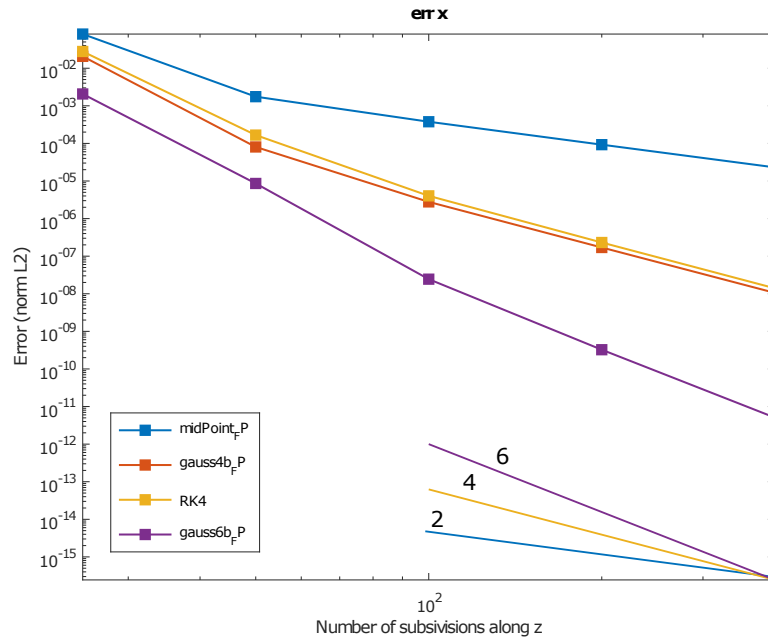


Figure 4.10: Analytic field: Relative L^2 -norm error for x .

In figures 4.10 and 4.11 the errors obtained with the different ODE methods are presented. A reference solution was computed using the exact vector potential and the MATLAB ODE solver `ode45`, with a maximum $\Delta z^{ref} = \Delta z^{data}/10$ and a relative error tolerance of 10^{-13} . Methods are tested integrating the particles motion doubling each time the subdivisions number for 5 times (25, 50, 100, 200, 400). Since we are dealing with a field that is not interpolated, the magnetic vector potential is computed exactly at each required location. The error computed was the L^2 relative norm error (see equation (3.38)). It can be proved that the errors in the x

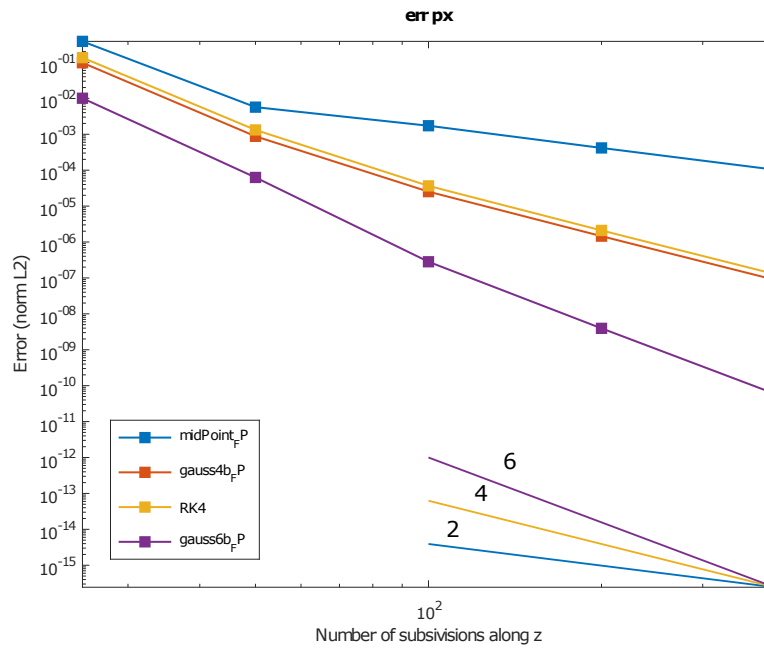


Figure 4.11: Analytic field: Relative L^2 -norm error for p_y .

and y coordinates behave very similarly and the same is true for the corresponding momenta. The behavior of the solvers is in agreement with their theoretical convergence order (on the right bottom of the plots, the ideal slopes corresponding to the theoretical convergence order is indicated). In this analytic case, high order symplectic integrators (Gauss6) are those ensuring the highest accuracy.

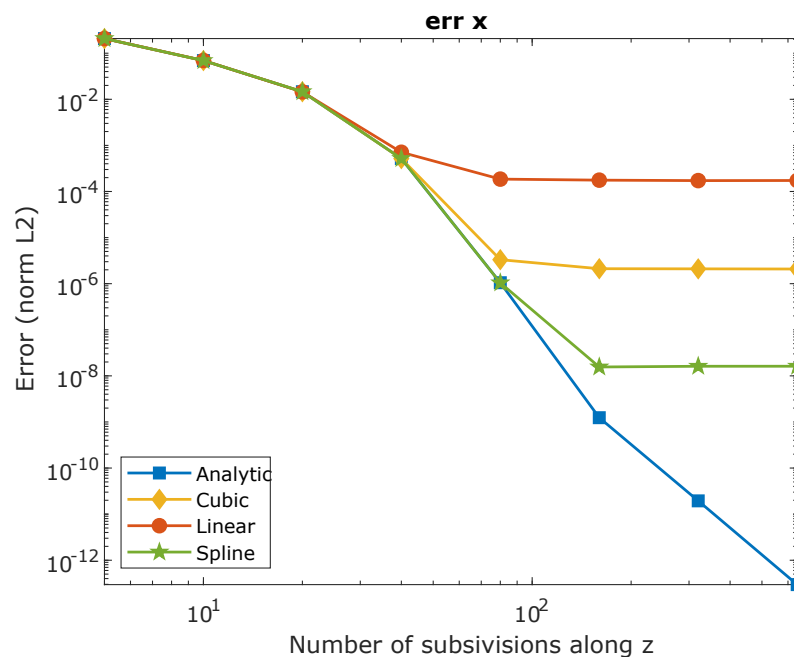


Figure 4.12: Gauss6, different interpolations: relative L^2 -norm error for x .

As we already said, in realistic cases the vector potential (1.28) is only available as sampled data on a discrete grid. For this reason, we tested the impact of different interpolation techniques on the integration methods. A three dimensional mesh was constructed imposing steps equal to $\Delta x = 0.007$ m, $\Delta y = 0.007$ m and $\Delta z = 0.003$ m over the intervals $x = [-0.15, 0.15]$ m, $y = [-0.15, 0.15]$ m and $z = [-2, 2]$ m. In this case, methods were tested integrating the particles motion doubling each time the subdivisions number for 8 times (5, 10, 20, 40, 80, 160, 320, 640). The vector potential value in each point not corresponding to the sampling points was computed applying different interpolation techniques. The results of the comparison is reported in figures 4.12, 4.13, 4.14 and 4.15. The 'linear' interpolated values at the query points are based on linear interpolation of the values at neighboring grid points in each dimension. With the 'cubic' method, the interpolated values are based on a piece-wise cubic, globally non differentiable interpolation of the values at neighboring grid points. The interpolated values at query points with the 'spline' method are based on the global cubic spline interpolation defined in section 3.3.3. Also the behavior in the analytic case, in which the error is depending

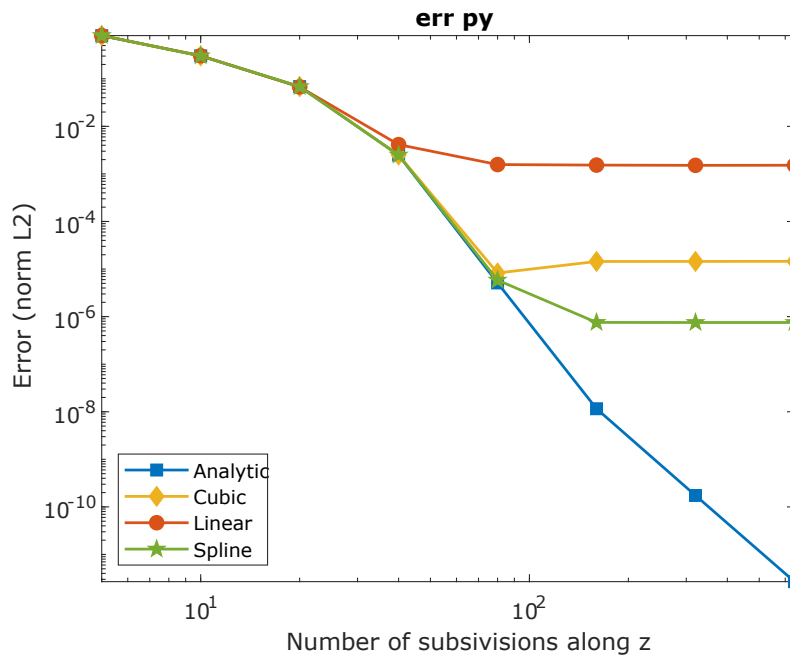


Figure 4.13: Gauss6, different interpolations: relative L^2 -norm error for p_y .

only on the integrator, is shown. In figures 4.12 and 4.13, results obtained with the sixth-order Gauss method are shown, since the highest order methods are more strongly affected by errors introduced by the interpolation process. The overall accuracy seems to be affected by all the interpolation methods. However, the 'spline' interpolation follows better the error achieved with the analytic vector potential. The overall error achieved by the interpolation methods is higher than the one observed in [Sim+19], even if the interpolating step along z is similar. This is most likely due to the fact that in our case, the interpolation was performed over the three directions, while in [Sim+19] a 1-dimensional interpolation was used.

As a comparison, in figures 4.14 and 4.15 the results obtained with the midpoint

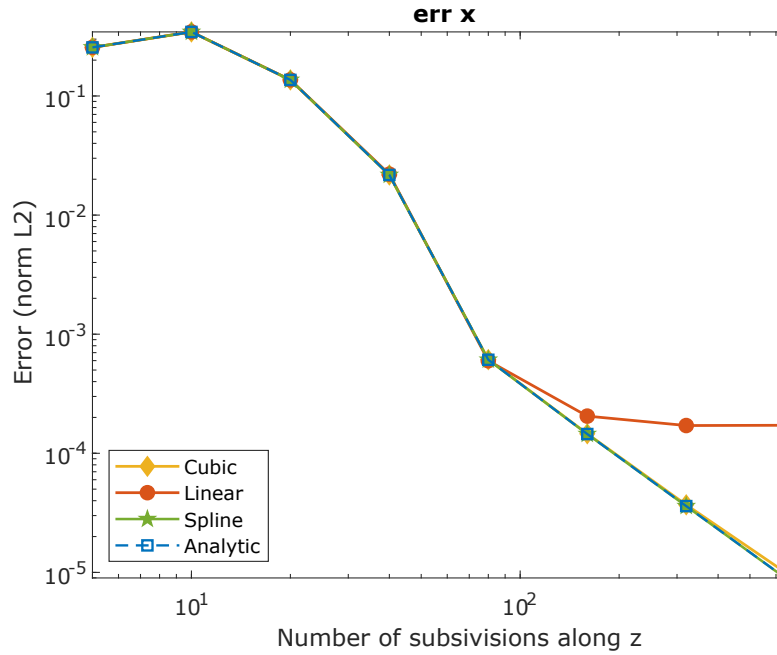


Figure 4.14: Mid-point, different interpolations: relative L^2 -norm error for x .

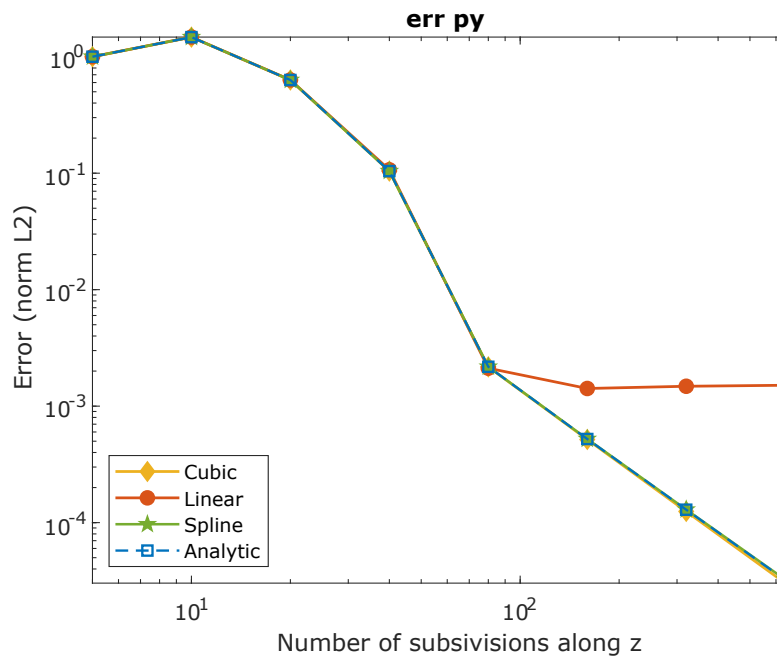


Figure 4.15: Mid-point, different interpolations: relative L^2 -norm error for p_y .

integration are presented. In this case, since we are dealing with a second order method, the interpolation does not influence the integration accuracy. Obviously, the overall accuracy is much lower than the one obtained with higher order methods. Further results concerning the effects of interpolation techniques on different integrators (see section 4.3) are reported. In the following figures, the results for the Runge Kutta 4 and the Gauss 4 method are reported.

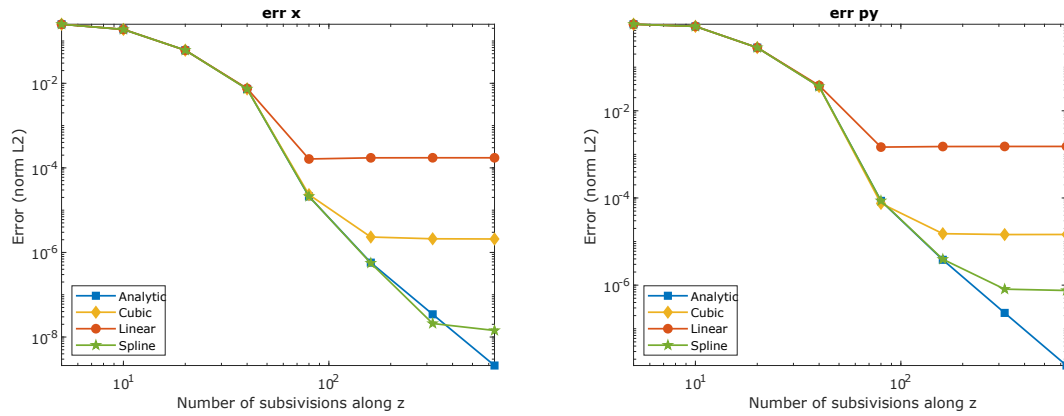


Figure 4.16: Runge Kutta 4, different interpolations: relative L^2 -norm error for x and p_y .

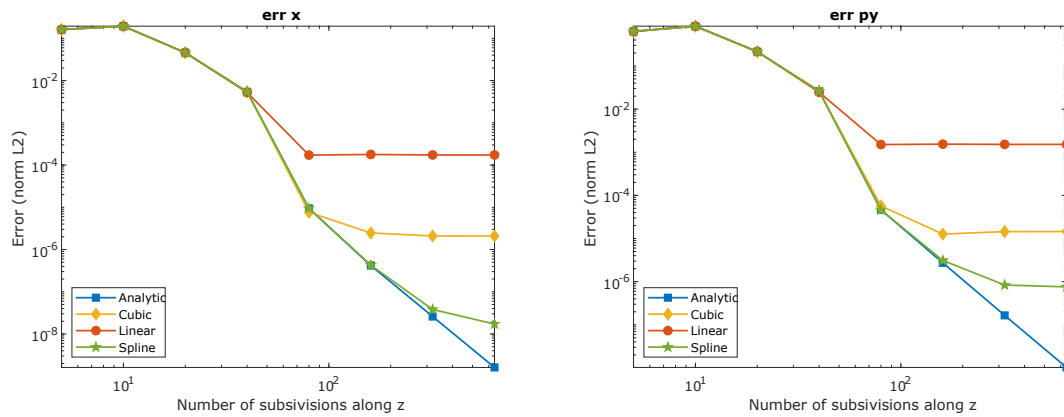


Figure 4.17: Gauss 4, different interpolations: relative L^2 -norm error for x and p_y .

From these results, it can be understood that, after a certain point, the error is limited by the accuracy of the reconstructed field. If a greater accuracy is needed, the use of very precise high order integrator will be ineffective. A better reconstruction of the field will be instead required.

In order to compare the efficiency of the methods employed, we performed the analysis of the required computational time for each method (fig 4.18 and 4.19). Also in this case, methods are tested integrating particles motion doubling each time the subdivisions number for 5 times (25, 50, 100, 200, 400). Among the ODE methods, the fourth order explicit Runge Kutta method gives the best results. Among the other methods, the sixth order Gauss method is the best one in order to achieve a high precision.

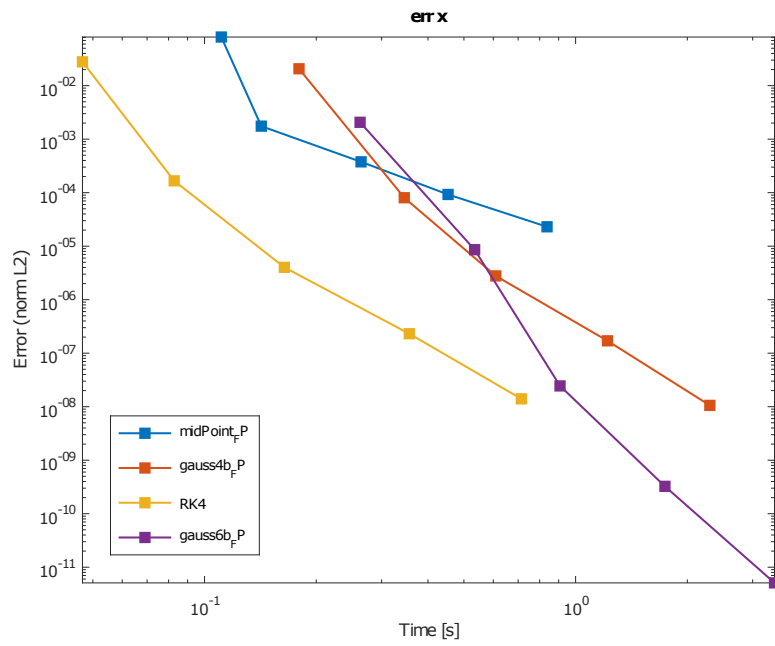


Figure 4.18: CPU time for the analytic field: relative L^2 -norm error for x .

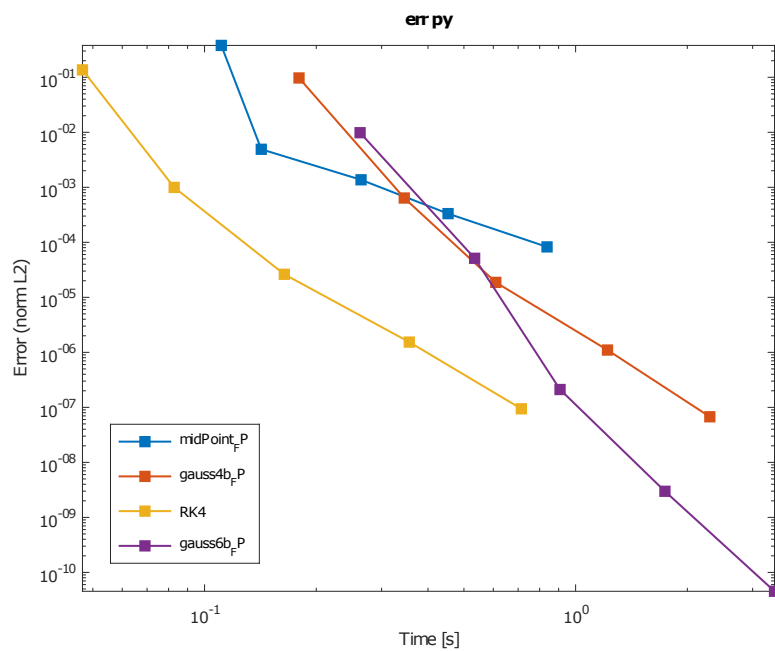


Figure 4.19: CPU time for the analytic field: relative L^2 -norm error for p_y .

4.4 Particle Tracking Results

Recalling the discussion in section 2.5, symplectic transformations must preserve the phase space volume (Liouville theorem). We already mentioned that, if after the interpolation the reconstructed field does not respect the divergence free condition $\nabla \cdot \mathbf{B} = 0$, Liouville theorem does not hold. In chapter 3.1, we showed how this problem can be addressed by introducing vector potential reconstruction and post-processing methods that preserve the divergence-free nature of the magnetic field. We also studied the differences between interpolation methods, concluding that some of them are actually less accurate than the standard methods in faithfully reconstructing the field behavior (see results in 4.1). In this section, we will report numerical results that show how preserving the divergence free properties of a field allows to improve the preservation of phase space volume during the tracking. In order to do that, we performed three different tests. The first one consists of a general observation of the trajectory behavior, in order to get an idea of what is happening during the turns if we use the field reconstructed in different ways. In the second test, we studied the volume in phase space through another parameter called emittance. In the last one, we simulated a measurement error on the magnetic field with the ultimate goal of proving the difference between the divergence-free-preserving methods.

The integration method used in all the tests is RK45, setting an absolute error of 10^{-13} . This method appeared to be very stable during the tracking, also after 10^6 revolutions, and allowed us to focus only on the effects of interpolation and post-processing errors.

4.5 First Test: Trajectory Study

As we discussed in section 2.5, volume preservation can be seen as a consequence of the symplectic properties. As a first test, we decided to focus our attention on a small distribution of particles with precise initial conditions, studying the variation of their dynamical variables and their trajectory over a big number of revolutions across the coils system. It has to be underlined that this kind of test is not representative of a real situation. However, it will give us a useful hint on what is happening in our system when a high number of revolutions is considered.

We assumed a grid space with $32 \times 32 \times 512$ points in each of the coordinates. The Hamilton equations were integrated using the adaptive RK45 method described in section 3.4. We divided the z axis, extended from 0 to 1.6 m, in 1000 integration steps and we imposed an absolute error of 10^{-13} . Consider that, in order to achieve this tolerance, the adaptive method may employ a number of integration steps larger than the initially prescribed one. We performed the particle tracking for a group of twelve electrons, distributed symmetrically around a reference electron in the 6D space (see fig. 4.20). For example, assuming the reference particle to be at the origin of the system ($\mathbf{w}(0, 0, 0, 0, 0, 0)$), we placed two particles along the x axis at a distance Δ from the reference particle, in $(\Delta, 0, 0, 0, 0, 0)$ and

$(-\Delta, 0, 0, 0, 0, 0)$. Δ was taken equal to 10^{-6} m. The same thing was done for all the dynamical variables. Afterwards, this distribution was sent through the system of coils previously described and tracked for 10^6 revolutions. In order to

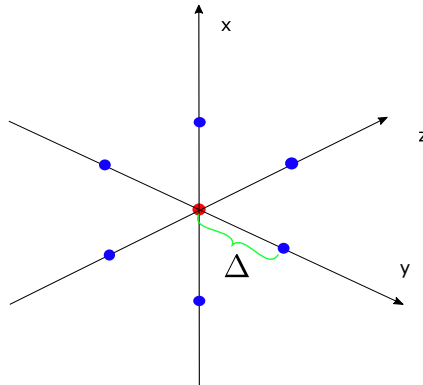


Figure 4.20: First test: arrangement of the particles (example in the 3D space).

get an idea of what happens to our distribution of particles, we can observe their trajectories on the xy plane for 10^6 revolutions. In a perfectly conservative system,

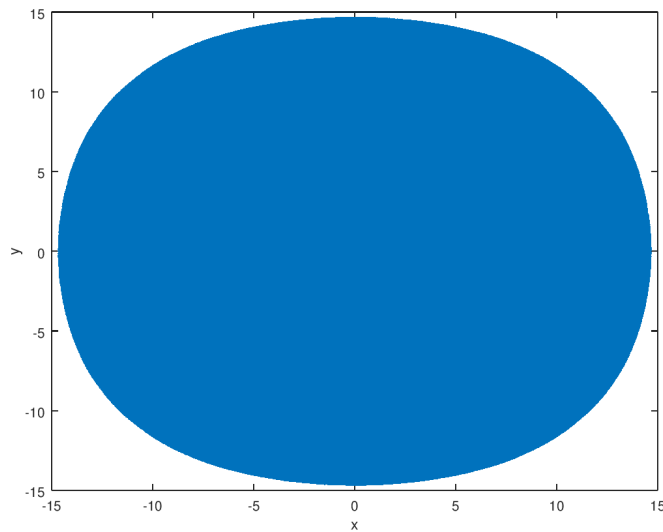


Figure 4.21: Trajectory on the xy plane for the analytic field directly interpolated with the LINT method.

we would expect to see a precise circle showing the particles to travel always along the same trajectory. In fig. 4.21, we show the final trajectory for the case of the trilinear interpolation of the analytic field (LINT). At the end of the simulation the trajectory of the particles over the xy plane is no more conserved, but collapses towards the axis. On the other hand, the trajectory of the particles in the case of the other field reconstruction approaches seems to be better preserved during the turns. This fact indicates that the energy is not conserved by the first interpolation approach. As we already mentioned, this can be an effect of the fact that the

divergence free properties are not conserved [BB80]. Indeed, it appears that the other two methods, even if not perfectly, are able to better preserve the particles trajectory even over 10^6 revolutions. In the next tests, we will give a quantitative assessment of this fact.

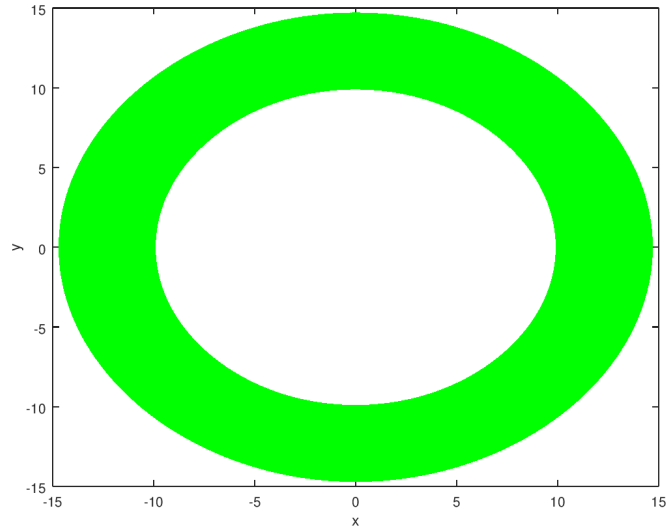


Figure 4.22: Trajectory on the xy plane for the analytic field reconstructed with the FIRST method.

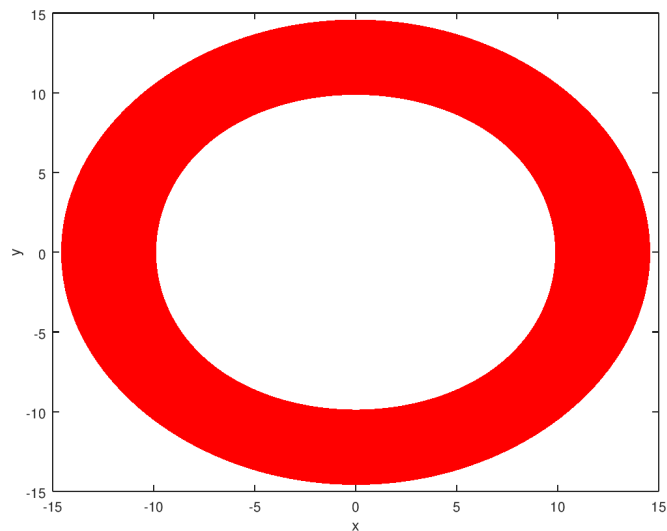


Figure 4.23: Trajectory on the xy plane for the analytic field reconstructed with the SECOND method.

4.6 Second Test: Emittance

Linear symplectic transformations in n degrees of freedom have associated with them n conserved quantities, the product of which corresponds to the phase space volume, that is conserved in all symplectic systems (see section 2.5, [Wol14]). In beam dynamics, these quantities can be expressed in terms of the so called *emittances*, which are one of the main tools used to describe beam dynamics.

Neglecting mutual interactions and coupling between the three coordinates of a particle, one defines the emittance of each degree of freedom: horizontal, vertical and longitudinal. The emittance is the property of a particle beam that characterizes its size. Roughly, it is proportional to the area or volume in the transverse phase space of particles. In an actual accelerator, the region in phase space in which particles stay in motion in the accelerator can be quite complicated, but it is frequently approximated by an *ellipse* [MMK06]. The original choice of an elliptical shape comes from the fact that when *linear* focusing forces are applied to a beam, the trajectory of each particle in phase space lies on an ellipse, which may be called the trajectory ellipse. In our special case, the non-linearity of the field does not allow the representation of the phase space with the elliptical approximation, so we directly studied the value of the emittance over the whole trajectory. Indeed, *non-linear* field components can stretch and distort the particle distribution in phase space. A realistic phase space distribution is quite different from a regular ellipse (see figure 4.24). We introduce, therefore, a definition of emittance that

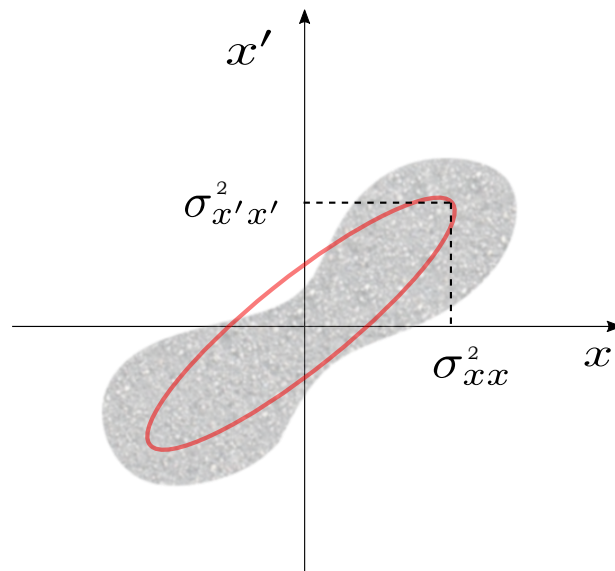


Figure 4.24: Particle distribution in a realistic case (in trace space (x, x')).

measures the beam quality rather than the phase space area: the *RMS (root mean square) emittance*. First, we need to introduce the so called *beam matrix*, which describes the statistical properties of the beam. The beam matrix for the transverse

dimension is defined as:

$$\Sigma_{xy} = \begin{pmatrix} \langle x^2 \rangle & \langle xx' \rangle & \langle xy \rangle & \langle xy' \rangle \\ \langle x'x \rangle & \langle x'^2 \rangle & \langle x'y \rangle & \langle x'y' \rangle \\ \langle xy \rangle & \langle x'y \rangle & \langle y^2 \rangle & \langle y'y' \rangle \\ \langle xy' \rangle & \langle x'y' \rangle & \langle yy' \rangle & \langle y'^2 \rangle \end{pmatrix} = \begin{pmatrix} \sigma_{xx}^2 & \sigma_{xy}^2 \\ \sigma_{xy}^2 & \sigma_{yy}^2 \end{pmatrix}, \quad (4.1)$$

where x and y are the horizontal and vertical coordinates, x' and y' are their derivatives with respect to the longitudinal coordinate and variances σ^2 are the so called *second moments* of the beam distribution. The formulation used refers to the so called *trace space* (x, x', y, y') , but it is completely equivalent to its formulation in the phase space. If the beam is transversely decoupled ($\sigma_{xy} = 0$), we can consider the two matrices separately in order to fully characterize the beam:

$$\Sigma_{uu} = \begin{pmatrix} \sigma_{uu}^2 & \sigma_{uu'}^2 \\ \sigma_{u'u}^2 & \sigma_{u'u'}^2 \end{pmatrix} = \begin{pmatrix} \langle u^2 \rangle & \langle uu' \rangle \\ \langle u'u \rangle & \langle u'^2 \rangle \end{pmatrix} \quad (4.2)$$

where u refers to either x or y . In this case, we define:

$$\begin{aligned} \sigma_{uu}^2 = \langle u^2 \rangle &= \frac{1}{N} \sum_j u_j^2 && \text{rms size;} \\ \sigma_{u'u'}^2 = \langle u'^2 \rangle &= \frac{1}{N} \sum_j u_j'^2 && \text{rms divergence;} \\ \sigma_{u'u}^2 = \langle uu' \rangle &= \frac{1}{N} \sum_j u_j u_j' && \text{correlation,} \end{aligned} \quad (4.3)$$

where N denotes the total number of particles. Finally, given a particle distribution, we define the *emittance* as:

$$\varepsilon_{rms} = \sqrt{\langle u^2 \rangle \langle u'^2 \rangle - \langle uu' \rangle^2} = \sqrt{\det \Sigma_{uu}}. \quad (4.4)$$

For linear systems, like drifts and quadrupoles, this quantity is an invariant (in absence of dissipative or cooling forces) [Buo92]. Let us consider now the spatial evolution of the beam emittance ε also in a non-linear case. The particle motion is assumed to be Hamiltonian, not significantly coupled and in general non-linear. It can be modeled with the general non-linear Hamiltonian:

$$H(x, x') = \frac{x'^2}{2} + f(x),$$

where $f(x)$ is a general \mathcal{C}^∞ function. The Hamilton equations of motion, with respect to the independent variable s are:

$$\frac{dx}{ds} = x'; \quad (4.5)$$

$$\frac{dx'}{ds} = -\frac{\partial H}{\partial x}. \quad (4.6)$$

The equations of motion of the barycentre (\bar{x}, \bar{x}') are:

$$\frac{d\bar{x}}{ds} = \bar{x}'; \quad (4.7)$$

$$\frac{d\bar{x}'}{ds} = -\frac{\overline{\partial H}}{\partial x}. \quad (4.8)$$

If the motion is linear, $\frac{\overline{\partial H}}{\partial x}$ is proportional to \bar{x} . Then, if the barycentre coincides with the origin ($\bar{x} = \bar{x}' = 0$) at some time, it stays at rest ($\frac{d\bar{x}}{ds} = \frac{d\bar{x}'}{ds} = 0$).

However, if the motion is non-linear, the derivative of \bar{x}' involves higher order moments of the coordinate x , and generally does not vanish. As a consequence, the barycentre moves in the phase space. Moreover, in general, $\frac{\overline{\partial H}}{\partial x}$ is not equal to $\frac{\partial H}{\partial x}(\bar{x})$. This means that in the non-linear case, the barycentre does not move according to the same law as the representative points. As a consequence, the straight lines joining a couple of points M_i, M_j and the barycentre O are not mapped into straight lines, and the triangle OM_iM_j is not mapped into another triangle, except in the linear case. Therefore, in a non-linear case, the Liouville theorem does not imply that the area A_{ij} of the triangles OM_iM_j is conserved. The emittance, here defined as a sum of areas A_{ij} , is not conserved except when the motion is linear. From this observation one can understand that, in the case of non-linear systems for which the Liouville theorem holds, the rms emittance is generally not conserved.

To obtain this result analytically, it is useful to compute the derivative $\frac{d\varepsilon}{ds}$ of the emittance. Here, we cannot in general assume $\bar{x} = \bar{x}' = 0$ and we must replace $\overline{x^2} = \overline{x'^2}$ and $\overline{xx'}$ by the central second-order moments $\sigma_{xx}^2, \sigma_{x'x'}^2$ and $\sigma_{xx'}^2$ respectively, in the expression of the emittance (4.4). Defining:

$$\mu_{xx} = \sigma_{xx}^2, \quad \mu_{x'x'} = \sigma_{x'x'}^2, \quad \mu_{xx'} = \sigma_{xx'}^2,$$

a straightforward calculation gives the derivatives of the moments:

$$\frac{d\mu_{xx}}{ds} = 2\mu_{xx'}; \quad (4.9)$$

$$\frac{d\mu_{x'x'}}{ds} = -2\mu_{01H}; \quad (4.10)$$

$$\frac{d\mu_{xx'}}{ds} = \mu_{x'x'} - \mu_{10H}, \quad (4.11)$$

where:

$$\mu_{10H} = x \frac{\overline{\partial H}}{\partial x} - \bar{x} \cdot \frac{\overline{\partial H}}{\partial x}, \quad (4.12)$$

$$\mu_{01H} = x' \frac{\overline{\partial H}}{\partial x} - \bar{x}' \cdot \frac{\overline{\partial H}}{\partial x}. \quad (4.13)$$

$$(4.14)$$

With these relations, the derivative $\frac{d\varepsilon}{ds}$ of the emittance is:

$$\frac{d\varepsilon}{ds} = \frac{1}{\varepsilon} (\mu_{x'x'} \mu_{10H} - \mu_{xx} \mu_{01H}). \quad (4.15)$$

As we discussed before, in the case of linear motion:

$$\frac{\partial H}{\partial x} = ax; \quad \overline{\frac{\partial H}{\partial x}} = a\bar{x},$$

and so:

$$\mu_{10H} = a\mu_{xx} \quad \text{and} \quad \mu_{01H} = a\mu_{xx'}.$$

The derivative $d\varepsilon/ds$ vanishes and the emittance is conserved.

When the motion is non-linear, $\frac{d\varepsilon}{ds}$ does generally not vanish for all s , and the emittance is not conserved. However, non-linearities are obviously harmful to the stability of motion and they are maintained at the smallest possible level in particle accelerators. Generally, all the causes of emittance dilution (coupling, scattering, radiation,...) are also minimized. An invariant emittance is a characteristic that should be preserved in any kind of system, linear or not. It can be concluded that in accelerators the beam emittance should be always conserved.

Going back to the simulation, we computed the emittance value (4.4) for 10^4 revolutions, considering the same system composed by 12 particles described in section 4.5. As shown in fig. 4.25, the different interpolation and reconstruction procedures have an impact on the emittance behaviour. If the trilinear method is applied, a substantial increase of the emittance (350 times higher than the starting value) can be observed. This behavior can be prove to diverge for further revolutions. On the other hand, the two post-processing methods show their ability to better

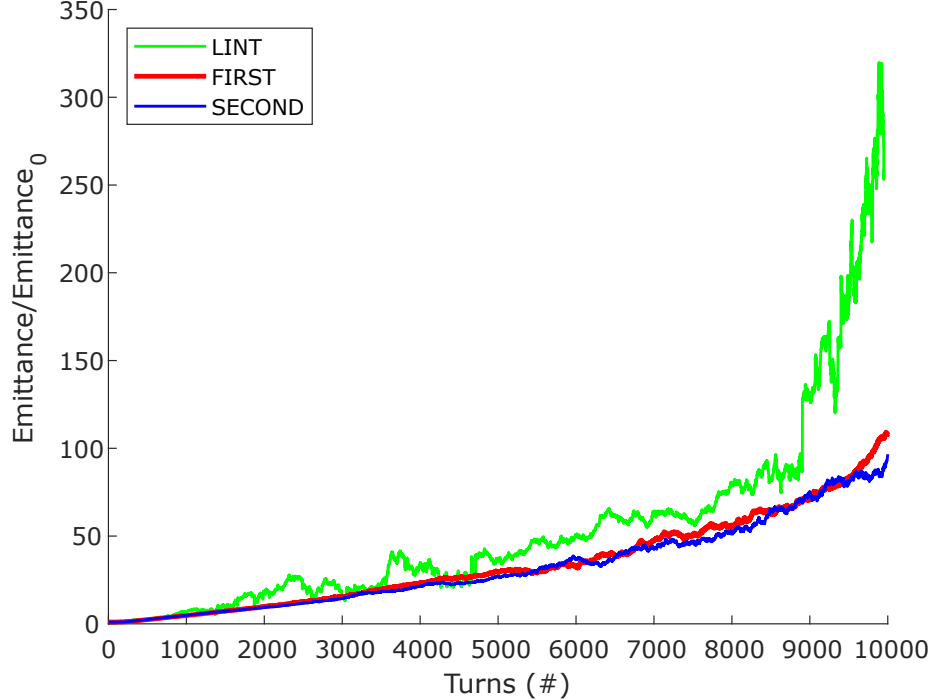


Figure 4.25: Emittance behavior for the three different methods vs. the number of turns.

preserve the emittance value. Looking at the zoomed figure 4.26, we can observe

that also in these cases the emittance experiences a growth. As we discussed before, this is the effect of the non-linearity of the field itself. This amount is obviously not negligible (100 times bigger than the starting value), but over 10^4 revolutions and compared with LINT behavior, it can be considered a good improvement. The starting emittance value is around $5 \cdot 10^{-13}$ m · mrad, while the final values are around $5 \cdot 10^{-11}$ for FIRST and SECOND methods and around $1.5 \cdot 10^{-10}$ m · mrad in LINT case. From these results we can derive the conclusion that the preservation of the divergence free properties of the field has an immediate positive impact on the preservation of the volume in phase space, in spite of the approximations and shortcomings of the methods described in sections 3.1.1 and 3.1.2.

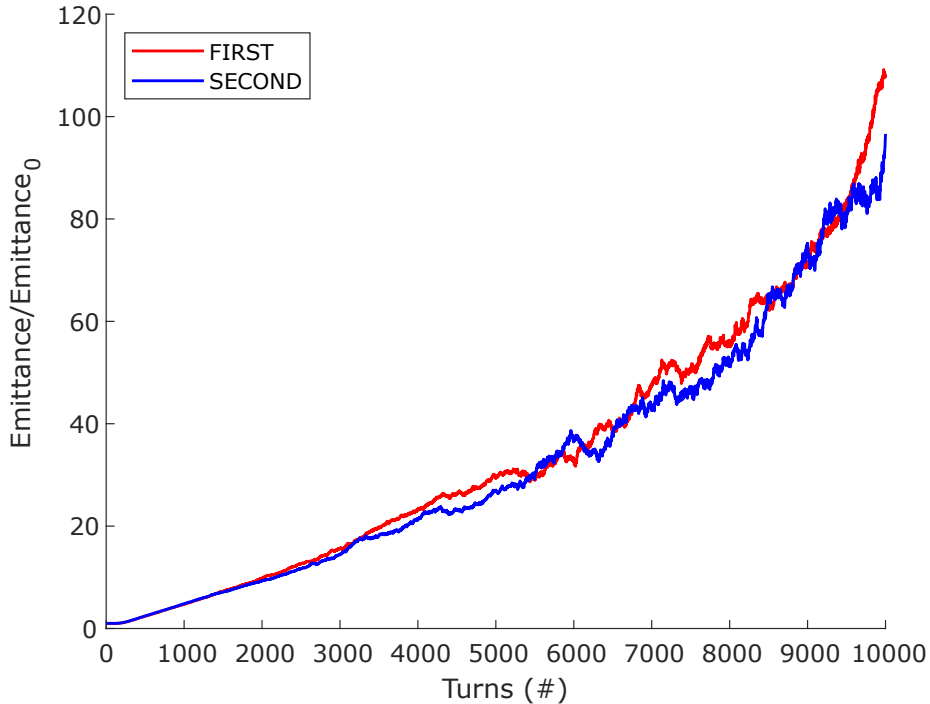


Figure 4.26: Emittance behavior for the divergence free preserving methods.

4.7 Third Test: Measurement Errors Correction

In the following test, we tried to underline the differences between the two post-processing methods in a more realistic case, for example with a measured field map. As discussed in chapter 3.1.2, the reconstruction of the field performed with the SECOND method, implies the complete elimination of the magnetic scalar potential φ and allows to prevent from contributions depending on the magnetic field evaluation. Indeed, according to [Dra19], the functions $\mathbf{G}_n(\mathbf{r}, \mathbf{r}')$ and $\mathbf{G}_t(\mathbf{r}, \mathbf{r}')$, for every $\mathbf{r}' \in S$, are analytic in \mathbf{r} for all $\mathbf{r} \in V$. It follows from (3.12) and (3.14), under mild conditions on $\mathbf{B}_n(\mathbf{r}')$ and $\varphi_n(\mathbf{r}')$, that $\mathbf{A}_n(\mathbf{r})$ and $\mathbf{A}_t(\mathbf{r})$ are analytic in V . Thanks to this procedure, only \mathbf{G}_n and \mathbf{G}_t need to be evaluated very accurately

and it does not matter how poorly \mathbf{B}_n and φ_t (see equations (3.12) and (3.15)) are evaluated. To sum up, the resulting \mathbf{A}_n and \mathbf{A}_t will be analytic in V and will satisfy the relations:

$$\begin{aligned}\nabla \cdot \mathbf{A}(\mathbf{r}) &= 0, \\ \nabla \times [\nabla \times \mathbf{A}(\mathbf{r})] &= 0.\end{aligned}\tag{4.16}$$

In order to show that the method does indeed benefit from these properties, we performed a specific test, adding a random error of $\sim 10^{-2}$ T in every point of the analytic field map's grid. In this case, we considered an interpolation grid more dense in the z direction, using $32 \times 32 \times 3200$ grid points. Then, we proceeded to the evaluation of the field with our three methods: on one hand, we directly interpolated the new data with the trilinear interpolation (LINT); on the other hand, we post-processed the data with the FIRST and the SECOND reconstruction methods, and we interpolated the results with the cubic spline. The numerical

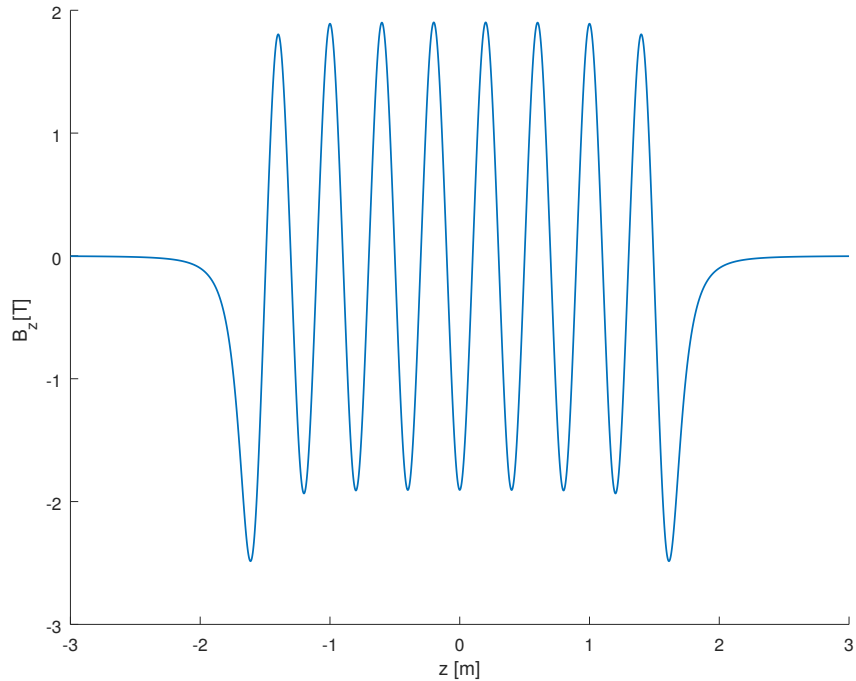


Figure 4.27: \mathbf{B}_z field considered in the third test.

integration of the equations of motion was performed with a Runge Kutta 45 integrator, with a maximum step of 10^{-4} and an absolute error of 10^{-13} . It has to be noticed that in this case, we integrated the equations coming from the time dependent Hamiltonian. Afterwards, we proceeded with the tracking.

In this case, the simulation considered a different situation with respect to the first two tests: the tracking was performed on a straight path, passing through a segment of 16 coils just once. Over such a short distance, it was possible to simulate the tracking of a significant number of particles: we randomly distributed 10^4 particles around a reference one in the 6D space. The new volume considered included also the contribution of the fringe fields (see fig. 4.27).

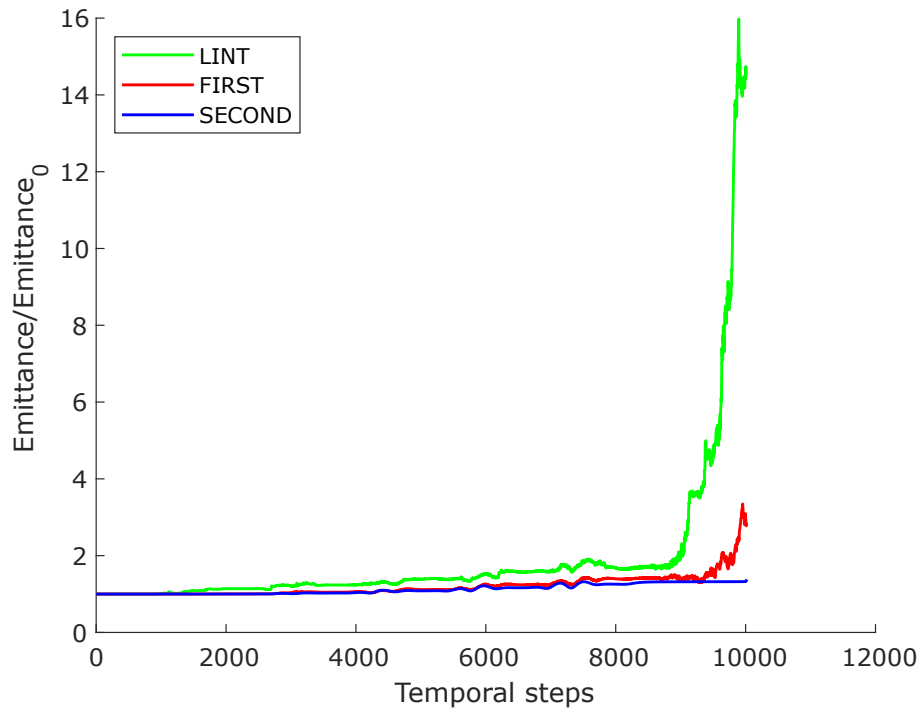


Figure 4.28: Transverse emittance over the number of integration steps.

The decision to perform just a single passage through our system was a necessity imposed by the long time needed by the simulation to track such an large number of particles.

As we discussed in chapter 4.6, the emittance is an important quantity to assess the conservation of the volume in phase space. Thus, we computed this quantity over our 10^4 time steps, to see what could be the effect of the addition of the measurement error.

Since just a single passage through our system was simulated, we do not expect to see a net variation of the emittance, as the one shown in fig. 4.25. However, since we added an extra error to the field data and we simulated a beam composed by an high number of particles, we expect to observe a growth of the emittance also along this short path. The results are shown in figure 4.28, and they seem to confirm our hypothesis. As in the other tests, the LINT field shows the worst emittance behavior, which starts growing from the first steps. The post-processing methods present a general lower spread in phase space. If we focus on the FIRST method results (see fig. 4.29), we can observe that, also in this case, the emittance values are growing progressively, reaching a peak in the lasts steps. On the other side, the best emittance behavior is given by the SECOND method. As it can be seen from the plots, the emittance seems generally more stable and constant in time, not showing particular peaks as with the other methods.

As a further support to this argument, another check was performed. Considering the same distribution of particles and the same system of coils with measurement

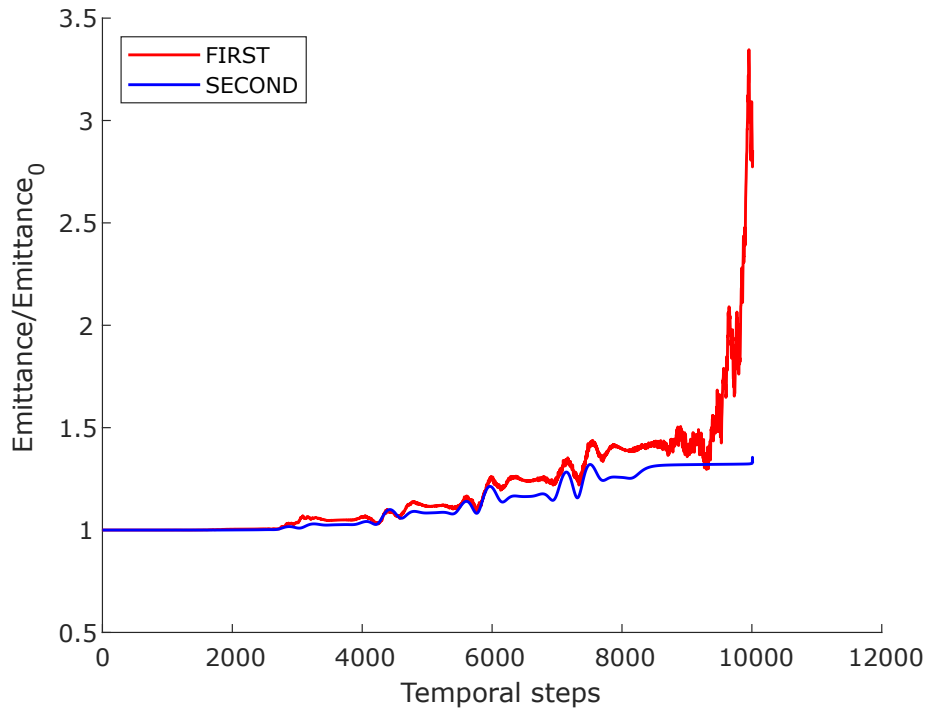


Figure 4.29: FIRST and SECOND methods: transverse emittance over the number of integration steps.

errors, the final positions of the particles were computed and a linear transfer map was fitted to the initial and corresponding final position in a least square sense. Afterwards, the absolute value of the determinant of this matrix was computed. Since it can be shown that the following theorem holds [LBH80]:

Theorem 4.7.1. *Let v_1, v_2, \dots, v_n be vectors in \mathbb{R}^n , let P be the n -dimensional parallelepiped determined by those vectors, and let M be the matrix with rows v_1, v_2, \dots, v_n . Then, the absolute value of the determinant of M is the volume of P :*

$$|\det(M)| = \text{vol}(P),$$

studying the temporal behavior of $|\det(M)|$, we can have an idea of how the volume is varying. As we can see in fig. 4.30 and 4.31, LINT method is showing high peaks, while the FIRST post-processing method tends to increase only at the end of the simulation. On the other hand, the SECOND post-processing method shows a constant behavior for all the integration steps. These results are coherent with the results reported in fig. 4.28.

These results support our previous arguments that the reconstruction performed using the SECOND method, ensuring always the preservation of $\nabla \cdot \mathbf{B} = 0$, results in a better conservation of the volume of the particles in the phase space, even in presence of measurement errors.

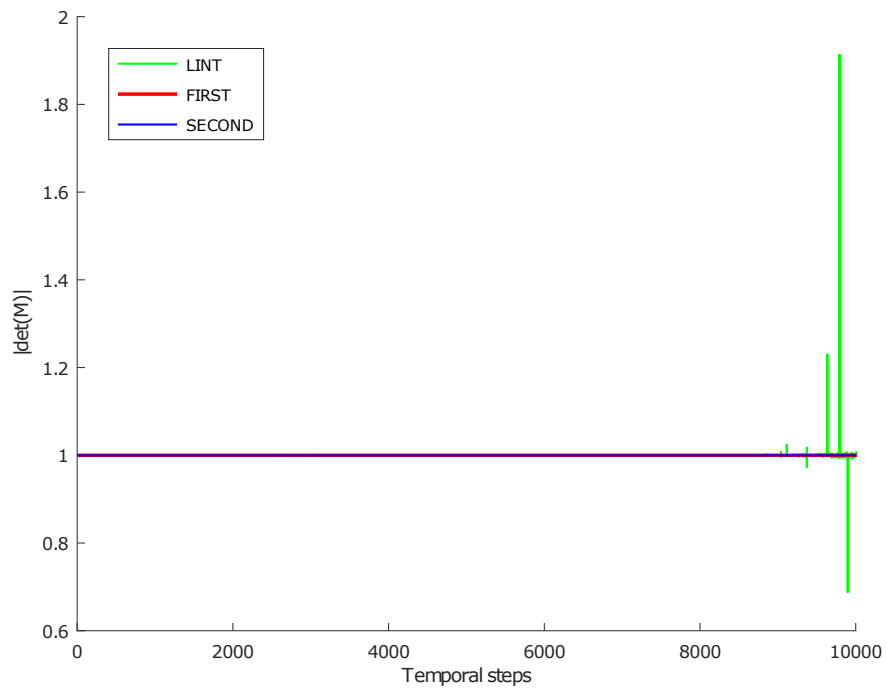


Figure 4.30: $|\det(M)|$ over the number of integration steps for all the methods.

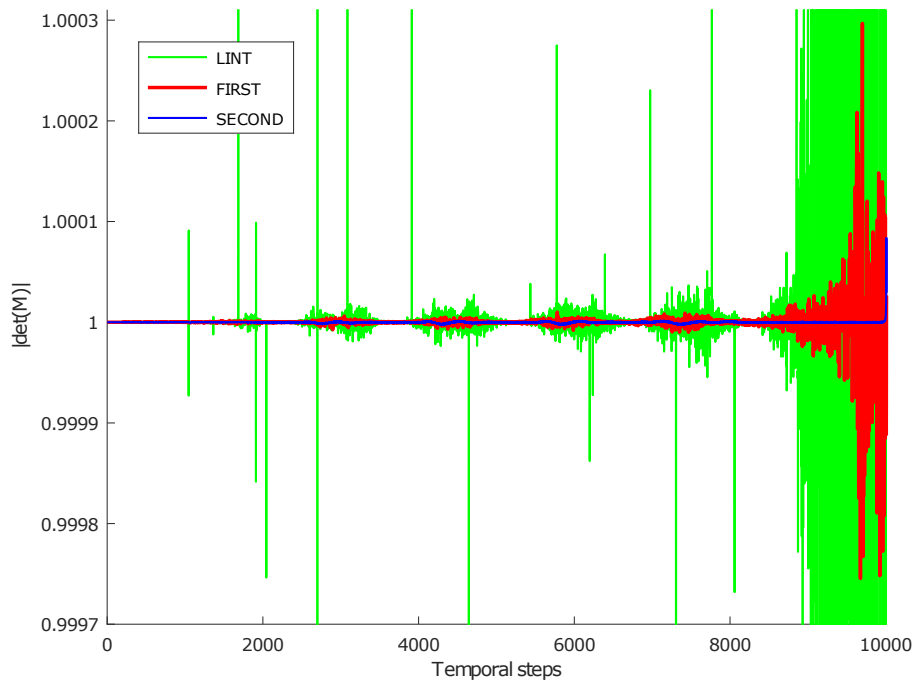


Figure 4.31: Zoom on FIRST and SECOND methods: $|\det(M)|$ over the number of integration steps.

Chapter 5

Conclusions and Perspectives

In this thesis, we have studied methods for the accurate reconstruction of magnetic fields from sampled values and numerical integration methods for the equations of motion of a charged particle in the reconstructed field. A system of coils leading opposite currents was taken as case study, in order to model non-linear elements in the presence of fringe fields.

Two techniques for the calculation of the vector potential were considered and implemented. These techniques can process realistic field maps, even in presence of measurement errors. In both cases, the particle tracking simulation using these post-processed fields showed an improvement of the conservation of the volume occupied in the phase space. Also the emittance growth proved to be limited, even over a large number of revolutions. In particular, the method implemented following the procedure outlined in [Dra19], guaranteed the full reconstruction of the vector potential, providing divergence-free properties even in case of non-negligible measurement errors. These results confirm the importance of working with divergence-free magnetic fields for stable particle tracking simulations.

Concerning the comparison of numerical methods for the approximation of the particle trajectories, high order symplectic Runge-Kutta integrators show good accuracy results, while standard explicit Runge-Kutta methods are among the most efficient for the considered problem. Moreover, following the steps described in [Sim+19], it was observed how the interpolated reconstruction of the vector potential plays a central role in the final accuracy of the tracking, limiting the results achievable with high order integration methods characterized by small integration steps. Also in this case, the use of cubic splines, ensuring a \mathcal{C}^2 continuity of the vector potential, provided the best results.

In this work many aspects of numerical methods and electromagnetic field modeling were involved, leading to many possible directions of improvement. In the future, it would be useful to improve the numerical methods present in “RF-Track” [Lat16], in order to increase the efficiency and the accuracy of the code. For example, the standard midpoint quadrature formula used for solving the integrals in the implementation of one of the post-processing method could be replaced by a higher order one.

Testing both with big numbers of particles and over a high number of turns appeared to be computationally intensive and was not feasible within this thesis work. We performed instead simulations focusing on each aspect separately. In future implementations it will be interesting to combine and tests these aspects.

Appendix A

Measure Units

A.1 Units

Description	Unit	Practical Unit
Length	m	m
Mass	kg	MeV · c ⁻²
Time	s	mm · c ⁻¹
Electric current	A	A
Electric charge	C	e
Force	N	MeV · m ⁻¹
Energy	J	MeV
Potential difference	V	V
Electric field strength	V · m ⁻¹	V · m ⁻¹
Magnetic flux density	T	T
Emittance	m · mrad	mm · mrad
Momentum	kg · m · s ⁻¹	MeV · c ²

A.2 Physical Constants

Description	Symbol	Unit
Speed of light in vacuum	c	$299792458 \text{ m} \cdot \text{s}^{-1}$
Elementary charge	e	$1,602176634 \cdot 10^{-19} \text{ C}$
Vacuum permeability	μ_0	$1,256637061 \cdot 10^{-6} \text{ N} \cdot \text{A}^{-2}$
Electron mass	m_e	$9,10938291 \cdot 10^{-31} \text{ kg}$

Appendix B

Liouville's Theorem Demonstration

The proof of the phase space volume conservation (and so the Liouville theorem) relies on the symplectic condition. We are going to rewrite the demonstration presented in section (2.5) in a more complete way [Tuc10]. Consider a phase space volume element $d\mathbf{w}$ at $t = 0$, containing a small collection of initial conditions on a set of trajectories. The trajectories evolve in time according to Hamilton's equations of motion, and at a time t later will be located in a new volume element $d\mathbf{W}$.

In order to keep clear the difference between Jacobian matrix and Jacobian determinant, now on we will respect the following definitions:

Definition B.0.1. If $f : \mathbb{R}^n \rightarrow \mathbb{R}^n$ is a \mathcal{C}^∞ -differentiable map, its *Jacobian matrix* is the $(m \times n)$ matrix of partial derivatives:

$$J_{ij} := \frac{\partial W_i}{\partial w_j} =, \quad i = 1, \dots, n; j = 1, \dots, n.$$

where $\mathbf{w} = (w_1, \dots, w_n)$ and $\mathbf{W} = (W_1, \dots, W_n)$.

Definition B.0.2. If $n = m$ the Jacobian matrix is a square matrix, hence its determinant $\det(J)$ is defined and called *the Jacobian* of f (possibly only at a point), defined as:

$$\mathcal{J} = \det J = \frac{\partial(W_1, \dots, W_n)}{\partial(w_1, \dots, w_n)}$$

Moreover, in order to make our calculation easier, we will also use the matrix exponential form. Given a differentiable matrix A , the following trace identity holds:

$$\det(e^A) = e^{\text{Tr}(A)}. \quad (\text{B.1})$$

An equivalent expression for the Jacobian is then:

$$\det(J) = e^{\text{Tr}(\ln J)}. \quad (\text{B.2})$$

The Liouville theorem condition we want to prove is:

$$dV = \prod_{i=1}^{2n} dW_i = |\det(J)| \prod_{i=1}^{2n} dw_i = \mathcal{J} \prod_{i=1}^{2n} dw_i = dv. \quad (\text{B.3})$$

We want to compute the time derivative of the Jacobian. In order to do so, we apply the so called Jacobi's Formula.

Theorem B.0.1. *If A is a differentiable map from the real numbers to $n \times n$ matrices,*

$$\frac{d}{dt} \det A(t) = \text{Tr} \left(\text{adj}(A(t)) \frac{dA(t)}{dt} \right)$$

where $\text{tr}(X)$ is the trace of the matrix X . Moreover, when A is invertible:

$$\text{adj}(A(t)) = \det(A)A^{-1}.$$

Then we get:

$$\frac{d\mathcal{J}}{dt} = \frac{d}{dt} \det J = \text{Tr} \left(\text{adj}(J) \frac{dJ(t)}{dt} \right) = \text{Tr} \left(\det(J)J^{-1} \frac{dJ(t)}{dt} \right). \quad (\text{B.4})$$

Substituting (B.2) in (B.4):

$$\begin{aligned} \frac{d\mathcal{J}}{dt} &= \text{Tr} \left(e^{\text{Tr}(\ln J)} J^{-1} \frac{dJ(t)}{dt} \right) = e^{\text{Tr}(\ln J)} \text{Tr} \left(J^{-1} \frac{dJ(t)}{dt} \right) = \\ &= \mathcal{J} \sum_{i=1}^m \sum_{j=1}^m \left(J_{ij}^{-1} \frac{dJ_{ij}(t)}{dt} \right) \end{aligned} \quad (\text{B.5})$$

The explicit expressions for the matrices J^{-1} and dJ/dt are:

$$\begin{aligned} J_{ij}^{-1} &= \frac{\partial w_i}{\partial W_j}, \\ \frac{dJ_{ij}(t)}{dt} &= \frac{d}{dt} \left[\frac{\partial W_i}{\partial w_j} \right] = \frac{\partial \dot{W}_j}{\partial w_i}. \end{aligned} \quad (\text{B.6})$$

Substituting (B.6) in (B.5):

$$\begin{aligned} \frac{d\mathcal{J}}{dt} &= \mathcal{J} \sum_{i,j=1}^n \left(\frac{\partial w_i}{\partial W_j} \frac{\partial \dot{W}_j}{\partial w_i} \right) \\ &= \mathcal{J} \sum_{i,j,k=1}^n \left(\frac{\partial w_i}{\partial W_j} \frac{\partial \dot{W}_j}{\partial W_k} \frac{\partial W_k}{\partial w_i} \right) \end{aligned} \quad (\text{B.7})$$

where the chain rule has been introduced for the derivative $\frac{\partial \dot{W}_j}{\partial w_i}$. The sum over i can now be performed:

$$\sum_{i=1}^n \frac{\partial w_i}{\partial W_j} \frac{\partial W_k}{\partial w_i} = \sum_{i=1}^n J_{ij}^{-1} J_{ki} = \sum_{i=0}^n J_{ki} J_{ij}^{-1} = \delta_{kj}.$$

Thus, we are left with:

$$\begin{aligned} \frac{d\mathcal{J}}{dt} &= \mathcal{J} \sum_{j,k=1}^n \left(\delta_{kj} \frac{\partial \dot{W}_j}{\partial W_k} \right) = \\ &= \mathcal{J} \sum_{j=1}^n \frac{\partial \dot{W}_j}{\partial W_j} = \mathcal{J} \nabla_W \cdot \dot{\mathbf{W}} \end{aligned} \quad (\text{B.8})$$

The initial condition on this differential equation is $\mathcal{J}(0) = \mathcal{J}(w, w) = 1$. Moreover, for a Hamiltonian systems:

$$\begin{aligned} \nabla_W \cdot \dot{\mathbf{W}} &= \nabla_W \cdot (\dot{\mathbf{Q}}, \dot{\mathbf{P}}) = \frac{\partial \dot{\mathbf{Q}}}{\partial \mathbf{Q}} + \frac{\partial \dot{\mathbf{P}}}{\partial \mathbf{P}} = \\ &= \frac{\partial}{\partial \mathbf{Q}} \left(\frac{\partial \mathbf{H}}{\partial \mathbf{P}} \right) + \frac{\partial}{\partial \mathbf{P}} \left(-\frac{\partial \mathbf{H}}{\partial \mathbf{Q}} \right) = \\ &= \frac{\partial^2 \mathbf{H}}{\partial \mathbf{Q} \partial \mathbf{P}} - \frac{\partial^2 \mathbf{H}}{\partial \mathbf{P} \partial \mathbf{Q}} = 0. \end{aligned} \tag{B.9}$$

This says that $d\mathcal{J}/dt = 0$, and $\mathcal{J}(0) = 1$. Thus:

$$|\mathcal{J}(\mathbf{w}, \mathbf{W})| = |\det J| = 1. \tag{B.10}$$

If this is true, then the phase space volume element transforms according to:

$$dV = \prod_{i=1}^{2n} dW_i = \prod_{i=1}^{2n} dw_i = dv.$$

This conservation law states that the phase space volume occupied by a collection of systems evolving according to Hamilton equations of motion will be preserved in time. This is one statement of Liouville theorem.

Bibliography

- [AS65] M. Abramowitz and I.A. Stegun. *Handbook of Mathematical Functions: With Formulas, Graphs, and Mathematical Tables*. Applied mathematics series. Dover Publications, 1965.
- [AWH13] G.B. Arfken, H.J. Weber, and F.E. Harris. *Mathematical Methods for Physicists: A Comprehensive Guide*. Elsevier Science, 2013.
- [BB80] J. U. Brackbill and D. C. Barnes. “The Effect of Nonzero $\nabla \cdot \mathbf{B}$ on the numerical solution of the magnetohydrodynamic equations”. *Journal of Computational Physics* 35.3 (1980), pp. 426–430.
- [BN82] Joseph Bak and Donald J. Newman. *Complex analysis*. Springer, 1982.
- [Buo92] Jean Buon. *Beam phase space and emittance*. Tech. rep. Paris-11 Univ., 1992.
- [CM08] Mario Conte and William W. MacKay. *An introduction to the physics of particle accelerators*. World Scientific Publishing Company, 2008.
- [CR74] Edwin Catmull and Raphael Rom. “A class of local interpolating splines”. In: *Computer aided geometric design*. Elsevier, 1974, pp. 317–326.
- [Dra19] Alex J. Dragt. *Lie methods for nonlinear dynamics with applications to accelerator physics*. 2019. URL: <https://www.physics.umd.edu/dsat/docs/Book12Nov2019.pdf>.
- [FM06] Antonio Fasano and Stefano Marmi. *Analytical mechanics: an introduction*. OUP Oxford, 2006.
- [Gou09] Brian Gough. *GNU scientific library reference manual*. Network Theory Ltd., 2009. URL: <http://www.gnu.org/software/gsl/>.
- [GPS02] Herbert Goldstein, Charles Poole, and John Safko. *Classical mechanics*. 2002.
- [HLS98] Marlis Hochbruck, Christian Lubich, and Hubert Selhofer. “Exponential integrators for large systems of differential equations”. *SIAM Journal on Scientific Computing* 19.5 (1998), pp. 1552–1574.
- [HLW06] Ernst Hairer, Christian Lubich, and Gerhard Wanner. *Geometric numerical integration: structure-preserving algorithms for ordinary differential equations*. Vol. 31. Springer Science & Business Media, 2006.
- [Jac99] J. D. Jackson. *Classical Electrodynamics, 3rd ed.* 1999.
- [Kun07] Kevin Kuns. “Calculation of magnetic field inside plasma chamber”. *UCLA report* 2.3 (2007), pp. 1–11.

- [Lan+82] L.D. Landau, E.M. Lifshitz, J.B. Sykes, and J.S. Bell. *Mechanics*. Butterworth-Heinemann. Elsevier Science, 1982.
- [Lat16] *RF-Track: beam tracking in field maps including space-charge effects. Features and benchmarks*. Proceedings of LINAC16, East Lansing, MI, USA, September 25-30 2016. 2016.
- [LBH80] Steven J Leon, Ion Bica, and Tiina Hohn. *Linear algebra with applications*. Macmillan New York, 1980.
- [McN11] C. P. McNally. “Divergence-free interpolation of vector fields from point values — exact $\nabla \cdot \mathbf{B} = 0$ in numerical simulations”. *Monthly Notices of the Royal Astronomical Society: Letters* 413.1 (May 2011), pp. L76–L80.
- [MJW15] B.D. Muratori, J.K. Jones, and A. Wolski. “Analytical expressions for fringe fields in multipole magnets”. *Physical Review Special Topics-Accelerators and Beams* 18.6 (2015), p. 064001.
- [MMK06] F. Mackay, R. Marchand, and K. Kabin. “Divergence-free magnetic field interpolation and charged particle trajectory integration”. *Journal of Geophysical Research: Space Physics* 111.A6 (2006).
- [QSS10] Alfio Quarteroni, Riccardo Sacco, and Fausto Saleri. *Numerical mathematics*. Vol. 37. Springer Science & Business Media, 2010.
- [Ree03] John R. Rees. *Symplecticity in beam dynamics: An introduction*. Tech. rep. Stanford Linear Accelerator Center, Menlo Park, CA (US), 2003.
- [SB13] Josef Stoer and Roland Bulirsch. *Introduction to numerical analysis*. Vol. 12. Springer Science & Business Media, 2013.
- [Sha12] A. Shadowitz. *The Electromagnetic Field*. Dover Books on Physics. Dover Publications, 2012.
- [Sim+19] Abele Simona, Luca Bonaventura, Thomas Pugnati, and Barbara Dalena. “High order time integrators for the simulation of charged particle motion in magnetic quadrupoles”. *Computer Physics Communications* 239 (2019), pp. 33–52.
- [Tuc10] Mark Tuckerman. *Statistical Mechanics: Theory and Molecular Simulation*. Oxford university press, 2010.
- [Wie07] Helmut Wiedemann. *Particle Accelerator Physics: Third Edition*. Springer, 2007.
- [Wol14] Andrzej Wolski. *Beam Dynamics in High Energy Particle Accelerators*. World Scientific, 2014.